

Universität  
Rostock



Traditio et Innovatio



# Study of design principles of titanium dioxide photocatalysts for solar hydrogen production

Dissertation  
zur Erlangung des akademischen Grades  
Doctor rerum naturalium (Dr. rer. nat.)

der Mathematisch-Naturwissenschaftlichen Fakultät  
der Universität Rostock

vorgelegt von  
Igor Medic, geboren am 08.06.1992 in Novi Sad, Serbien  
Rostock, 20.03.2023



Dieses Werk ist lizenziert unter einer  
Creative Commons Namensnennung - Nicht kommerziell - Keine Bearbeitungen 4.0  
International Lizenz.

This work was carried out between August 2019 and March 2023 at the Leibniz Institute for Catalysis e. V. (LIKAT) in Rostock.



# Declaration

I declare that the research work presented in this thesis is my own and carried out entirely at the Leibniz Institute for Catalysis (LIKAT), Rostock, Germany under the supervision of Prof. Dr. Jennifer Strunk (Head of the Department Heterogeneous Photocatalysis).

Rostock, 20.03.2023

Igor Medic

## Referees

1. Prof. Dr. Jennifer Strunk, Leibniz Institute for Catalysis, University of Rostock
2. Prof. Dr. Radim Beranek, Institute for Electrochemistry, Ulm University

**Date of thesis submission:** 20.03.2023

**Date of defense:** 13.06.2023



# Acknowledgement

I would like to thank Prof. Jennifer Strunk for the opportunity to conduct research in Heterogeneous Catalysis Department at LIKAT. I am grateful for offered advice and persistent encouragement that always came with perfect blend of insight and humor, blazing the trail through complex and dynamic research challenges.

Immense gratitude to Dr. Alexander Zapf for his patience and support. Our discussions helped me to adopt comprehensive problem-solving way of thinking which is something I hope to carry forward throughout my career.

Former and current Department members, particularly Dr. Marcus Klahn, Dr. Moritz Lang, Junhao Huang and Merlin Gutgesell from structure-function correlation group made my research both productive and enjoyable.

I am thankful to Dr. Henrik Junge for motivation and generous donation of initial experimental set-up for testing photocatalytic H<sub>2</sub> production as well as Petra Bartels and Anja Kammer for training and assistance during the photocatalytic tests.

I would like to thank Dr. Henrik Lund and Kathleen Schubert for XRD measurements; Dr. Stephan Bartling and Fabian Strunk for XPS measurements; Dr. Carsten Robert Kreyenschulte for STEM-EELS measurements; Astrid Lehmann for AAS and carbon analysis. Special thanks to Dr. Armin Springer from Electron microscopy center at University of Rostock for TEM measurements.

Gratitude to Andreas Hutter, Matthias Auer and Thomas Rall for a technical assistance as well as the rest of LIKAT staff for the pleasant work atmosphere.

I am thankful to the Leibniz Association for financial support of my reseach within the Leibniz ComBioCat Science Campus.

As always, I am immensely grateful to my family and friends without whose love dreams would not become reality.





# Abstract

Among particulate photocatalysts, particulate  $\text{TiO}_2$  has been used for long time as hydrogen evolution catalyst.  $\text{TiO}_2$  is abundant, robust and shows high UV photocatalytic activity. For practical application, however, using solar light instead of UV is highly desirable. The transition from UV to solar sensitization of  $\text{TiO}_2$  is challenging and often results in sluggish  $\text{H}_2$  production. Therefore, design and construction of efficient solar  $\text{TiO}_2$  catalysts is still a primary goal of work in the field. Intrinsically, low solar photocatalytic activity of  $\text{TiO}_2$  can be tackled either with doping or nanostructuring, thus improving the solar light harvesting or charge carrier dynamics. Here, doping and nanostructuring principles in design of efficient solar  $\text{TiO}_2$  catalysts are studied on self-doped  $\text{TiO}_2$  and rutile needle catalysts. The self-doped  $\text{TiO}_2$  were synthesized in the reaction between  $\text{TiO}_2$  and sodium-potassium alloy while rutile needles were prepared from titanium-tetraisoopropoxide (TTIP) under acidic conditions. Both syntheses were run at room temperature. Structural characterization reveals that self-doped  $\text{TiO}_2$  adopts hybrid  $\text{TiO}_2@Ti^{3+}/TiO_2@TiO_2$  structure with disordered layer embedded between  $\text{TiO}_2$  crystalline core and  $\text{TiO}_2$  overlayer, where formed  $Ti^{3+}$  ions are in the disordered layer. In contrast, rutile needles are pure phase rutile crystalline  $\text{TiO}_2$ . However, in needles the anisotropic crystal growth at temperature of 200 °C is observed that preferentially occurs along crystal c-axis and triggers morphology change from needle to plate. Study of optical properties confirms that band gaps in rutile needles are around 3 eV, typical for rutile polymorph, while light harvesting of self-doped  $\text{TiO}_2$  is greatly enhanced by introduction of  $Ti^{3+}$  in-band electronic states 1.3 eV below conduction band. Thus, these states enhance working solar spectrum of self-doped  $\text{TiO}_2$ . Common for both  $\text{TiO}_2$  materials, though, is that they do not expose  $Ti^{3+}$  ions or oxygen vacancies at their surfaces. When solar  $\text{H}_2$  production performance is compared, the rutile needles synthesized under optimized conditions were 30 times as active as an optimized self-doped  $\text{TiO}_2$  catalyst. Also, rutile needle catalyst performs 3 and 4.5 times better comparing with nanoparticulate  $\text{TiO}_2$  P25 and rutile  $\text{TiO}_2$  benchmarks, respectively. Finally, correlation of structure and activity in self-doped  $\text{TiO}_2$  reveals that nature and spatial distribution of  $Ti^{3+}$  ions are primary determinants of solar  $\text{H}_2$  production. Even though  $Ti^{3+}$  ions improve working solar spectrum, they also hamper charge carrier dynamics by introducing new recombination centers, which apparently influences photocatalysis more. On the other hand, effective shortening of bulk charge carrier diffusion path by nanostructuring is proven to be the key for improved transport of photogenerated electrons leading to efficient solar  $\text{H}_2$  production with rutile structures. Thus, well-structured defect-free  $\text{TiO}_2$  catalysts that separate photogenerated electrons and holes efficiently are good candidates for  $\text{H}_2$  production under solar light. Alternatively, doped- $\text{TiO}_2$  structures with enhanced solar light harvesting can be considered for solar  $\text{H}_2$  production if subsurface transformation that typically occurs during doping is circumvented.



# Zusammenfassung

Unter den partikelförmigen Photokatalysatoren wird seit langem partikelförmiges  $\text{TiO}_2$  als Katalysator für die Wasserstoffentwicklung verwendet.  $\text{TiO}_2$  ist reichlich vorhanden, robust und zeigt eine hohe UV-photokatalytische Aktivität. Für die praktische Anwendung ist jedoch die Verwendung von Sonnenlicht anstelle von UV-Licht höchst wünschenswert. Der Übergang von der UV- zur Sonnensensibilisierung von  $\text{TiO}_2$  ist eine Herausforderung und führt oft zu einer langsamen  $\text{H}_2$ -Produktion. Daher sind das Design und die Konstruktion von effizienten Solar- $\text{TiO}_2$ -Katalysatoren nach wie vor das Hauptziel der Forschung auf diesem Gebiet. Die geringe solare photokatalytische Aktivität von  $\text{TiO}_2$  kann an entweder durch Dotierung oder Nanostrukturierung angegangen werden, wodurch die Sonnenlichtaufnahme oder die Ladungsträgerdynamik verbessert werden. Hier werden Dotierungs- und Nanostrukturierungsprinzipien beim Design effizienter Solar- $\text{TiO}_2$ -Katalysatoren an selbstdotierten  $\text{TiO}_2$ - und Rutil-Nadelkatalysatoren untersucht. Das selbstdotierte  $\text{TiO}_2$  wurde in der Reaktion zwischen  $\text{TiO}_2$  und einer Natrium-Kalium-Legierung synthetisiert, während Rutil-Nadeln aus TTIP unter sauren Bedingungen hergestellt wurden. Beide Synthesen wurden bei Raumtemperatur durchgeführt. Die strukturelle Charakterisierung zeigt, dass selbstdotiertes  $\text{TiO}_2$  eine  $\text{TiO}_2@ \text{Ti}^{3+}/ \text{TiO}_2@ \text{TiO}_2$ -Hybridstruktur mit einer ungeordneten Schicht annimmt, die zwischen dem kristallinen  $\text{TiO}_2$ -Kern und der  $\text{TiO}_2$ -Deckschicht eingebettet ist, wobei sich die gebildeten  $\text{Ti}^{3+}$ -Ionen in der ungeordneten Schicht befinden. Im Gegensatz dazu sind Rutil-Nadeln kristallines Rutil- $\text{TiO}_2$  in reiner Phase. In Nadeln wird jedoch anisotropes Kristallwachstum bei einer Temperatur von 200 °C beobachtet, das vorzugsweise entlang der Kristall-c-Achse auftritt und eine Morphologieänderung von der Nadel zur Platte auslöst. Die Untersuchung der optischen Eigenschaften bestätigt, dass die Bandlücken in Rutil-Nadeln etwa 3 eV betragen, was typisch für Rutilpolymorphe ist, während die Lichtsammlung von selbstdotiertem  $\text{TiO}_2$  durch die Einführung von  $\text{Ti}^{3+}$ -elektronischen Zuständen im Band 1,3 eV unterhalb des Leitungsbands stark verbessert wird. Somit verbessern diese Zustände den nutzbaren Anteil des Sonnenspektrums von selbstdotiertem  $\text{TiO}_2$ . Beiden  $\text{TiO}_2$ -Materialien ist jedoch gemeinsam, dass sie keine  $\text{Ti}^{3+}$ -Ionen oder Sauerstoffleerstellen an ihren Oberflächen freilegen. Beim Vergleich der solaren  $\text{H}_2$ -Produktionsleistung waren die unter optimierten Bedingungen synthetisierten Rutilnadeln 30-mal so aktiv wie ein optimierter selbstdotierter  $\text{TiO}_2$ -Katalysator. Außerdem schneidet der Rutil-Nadelkatalysator 3- bzw. 4,5-mal besser ab im Vergleich zu nanopartikulären  $\text{TiO}_2$  P25- bzw. Rutil- $\text{TiO}_2$ -Benchmarks. Schließlich zeigt die Korrelation von Struktur und Aktivität in selbstdotiertem  $\text{TiO}_2$ , dass  $\text{Ti}^{3+}$ -Ionen unter der Oberfläche im Volumen die primäre Determinante der solaren  $\text{H}_2$ -Produktion sind. Obwohl  $\text{Ti}^{3+}$ -Ionen den nutzbaren Anteil des Sonnenspektrums vergrößern, behindern sie auch die Dynamik der Ladungsträger, indem sie neue Rekombinationszentren einführen, was die Photokatalyse offensichtlich stärker beeinflusst. Andererseits hat sich die effektive Verkürzung des Diffusionsweges der Volumenladungsträger durch Nanostrukturierung als Schlüssel zur effizienten solaren  $\text{H}_2$ -Produktion mit Rutilstrukturen erwiesen. Daher sind gut

strukturierte, defektfreie TiO<sub>2</sub>-Katalysatoren, die photogeneratede Elektronen und Löcher effizient trennen, gute Kandidaten für die H<sub>2</sub>-Produktion unter Sonnenlicht. Alternativ können dotierte TiO<sub>2</sub>-Strukturen mit verbesserter Sonnenlichternte für die solare H<sub>2</sub>-Produktion in Betracht gezogen werden, wenn die Umstrukturierung unter der Oberfläche, die typischerweise während des Dotierens auftritt, umgangen wird.

# Table of contents

Table of contents.....	i
List of abbreviations and symbols.....	iii
1. Introduction.....	1
1.1 Hydrogen – power of the future .....	1
1.2 Heterogeneous photocatalysis.....	2
1.2.1 Light absorption, solar spectrum and air mass .....	2
1.2.2 Band structure and Fermi level .....	4
1.2.3 Thermodynamic aspects of heterogeneous photocatalysis.....	5
1.2.4 Mass transport .....	7
1.3 TiO <sub>2</sub> as a photocatalyst.....	9
1.3.1 Crystal phases of TiO <sub>2</sub> .....	9
1.3.1.1 Rutile TiO <sub>2</sub> .....	10
1.3.1.2 Anatase TiO <sub>2</sub> and anatase-rutile mixed-phase TiO <sub>2</sub> .....	13
1.3.2 Solar light harvesting by TiO <sub>2</sub> .....	14
1.3.3 Charge carrier dynamics, trapping and recombination.....	16
1.3.4 Band bending in TiO <sub>2</sub> .....	18
1.4 Hydrogen production by heterogeneous photocatalysis on TiO <sub>2</sub> .....	20
1.4.1 The photocatalytic H <sub>2</sub> production from water .....	21
1.4.2 Photocatalytic H <sub>2</sub> production from water/alcohol mixture .....	22
1.5 Aims and outline of the thesis.....	25
2. Experimental .....	27
2.1 Catalyst synthesis .....	27
2.1.1 Synthesis of blue titania in reaction with Na/K alloy (B-TiO <sub>2</sub> ).....	27
2.1.2 Synthesis of grey titania by thermal annealing of B-TiO <sub>2</sub> (G-TiO <sub>2</sub> ) .....	28
2.1.3 Synthesis of rutile needles under ambient conditions.....	28
2.2 Photocatalytic H <sub>2</sub> production testing .....	28
2.3 Catalyst characterization .....	31
2.3.1 X-ray diffraction (XRD).....	31
2.3.2 Transmission electron microscopy (TEM) .....	33
2.3.3 Diffuse reflectance UV-Vis-NIR spectroscopy (DRS).....	34
2.3.4 X-ray photoelectron (XP) spectroscopy.....	37
2.3.5 Electron paramagnetic resonance (EPR) .....	38
2.3.6 Atomic absorption spectroscopy (AAS).....	40

2.3.7 Analysis of carbon impurities .....	41
3. Impact of Ti <sup>3+</sup> ions on light harvesting and photocatalytic activity of self-doped TiO <sub>2</sub> as seen from solar H <sub>2</sub> production.....	42
3.1 Synthesis of self-doped TiO <sub>2</sub> and composition analysis .....	42
3.2 Crystal structure and morphology of self-doped TiO <sub>2</sub> .....	48
3.3 Optical properties of self-doped TiO <sub>2</sub> .....	53
3.4 Study of Ti <sup>3+</sup> ions in self-doped TiO <sub>2</sub> .....	56
3.5 Structural model of self-doped TiO <sub>2</sub> .....	64
3.6 Photocatalytic activity of self-doped TiO <sub>2</sub> .....	65
3.6.1 H <sub>2</sub> production under 1.5 AM solar simulated light.....	65
3.6.2 Effect of Ti <sup>3+</sup> ions on solar H <sub>2</sub> production of self-doped TiO <sub>2</sub> .....	66
3.7 Conclusions.....	67
4. Size effect in rutile structures on photocatalytic H <sub>2</sub> production under solar light .....	69
4.1 Synthesis of rutile needles .....	69
4.2 Morphology and crystal structure of rutile needles .....	71
4.3 Optical properties of rutile needles .....	76
4.4 Analysis of surface states in rutile needles .....	77
4.5 Photocatalytic activity of rutile needle catalysts in H <sub>2</sub> production .....	80
4.5.1 H <sub>2</sub> production under 1.5 AM solar simulated light.....	80
4.5.2 H <sub>2</sub> production under sun light .....	81
4.5.3 Influence of test conditions on photocatalytic performance of rutile catalysts.....	83
4.6 Structure-activity relationship in rutile needle catalysts .....	85
4.7 Conclusions.....	87
5. Final conclusions and prospects.....	89
References.....	91

# List of abbreviations and symbols

Abbreviation/symbol	Denotation
A	electron acceptor molecule
a.u.	arbitrary unit
AAS	atomic absorption spectroscopy
ADF	annular dark field
AM	air mass
AO	atomic orbital
BE	binding energy
BF	bright field
CB	conduction band
CBM	conduction band minimum
CdS	cadmium sulfide
CO <sub>2</sub>	carbon dioxide
CW	continuous wave
D	electron donor molecule
d	mean crystallite size
$\Delta E_g$	band gap
$\Delta G_0$	change of Gibbs free energy
$\Delta H_f$	enthalpy of formation
DME	dimethoxyethane
DRS	diffuse reflectance UV-Vis-NIR spectroscopy
e <sup>-</sup>	electron
EELS	electron energy-loss spectroscopy
$E_F$	Fermi level
$E_{F,n}$	quasi-Fermi-level of electrons
$E_{F,p}$	quasi-Fermi-level of holes
ELNES	energy-loss near-edge structure
EPR	electron paramagnetic resonance
FWHM	full width at half maximum
g	proportionality factor in EPR
$\gamma$	gamma ray photon
GHS	greenhouse gas
h <sup>+</sup>	hole
<sup>1</sup> H <sup>+</sup>	proton
H <sub>2</sub>	hydrogen
H <sub>2</sub> O	water
HAADF	high angle annular darkfield detector
<sup>4</sup> He	helium
HEP	hydrogen evolution photocatalyst
HER	hydrogen evolution reaction
ICDD	International Center of Diffraction Data
IR	infrared
k	Boltzmann constant

kWm <sup>-2</sup>	kilowatt per square meter
MLLS	multilinear least-square
MO	molecular orbital
MS	mass spectrometer
n <sub>filled</sub>	filled energy levels
NIR	near infrared
n <sub>total</sub>	total energy levels
ν <sub>e</sub>	electron neutrino
OEP	oxygen evolution photocatalyst
OER	oxygen evolution reaction
OWS	overall water splitting
PEC	photoelectrochemical cell
ppm	parts per million
PTFE	polytetrafluoroethylene
PV-E	photovoltaic-assisted electrolysis
Q	gas flow
SR	surface recombination
STEM	scanning transmission electron microscopy
TEM	transmission electron microscopy
θ	Bragg angle
TTIP	titanium tetraisopropoxide
UA	astronomical unit
UV/Vis	ultraviolet-visible
VB	valence band
VBM	valence band maximum
VR	volume recombination
wt%	weight percent
XP	x-ray photoelectron
XRD	x-ray diffraction
ζ	solar zenith angle



# 1. Introduction

## 1.1 Hydrogen – power of the future

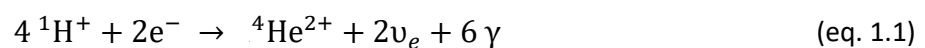
The ever-increasing demand for energy results in massive use of fossil fuels and rapid depletion of the natural reservoirs. The energy in fossil fuels such as coal, oil and natural gas is stored in chemical bonds and it can be released by their combustion, generating carbon dioxide (CO<sub>2</sub>) as a side-product. In 2021 CO<sub>2</sub> emission worldwide was determined to be 36.3 Gt, the amount of anthropogenic CO<sub>2</sub> that cannot be captured by the natural carbon cycle, but instead it accumulates as gaseous CO<sub>2</sub> in the atmosphere.<sup>1, 2</sup> As a result, the atmospheric CO<sub>2</sub> concentration increased from 278 ppm at the beginning of the industrial revolution (around 1750) to 416 ppm in September 2022.<sup>3, 4</sup> Elevated concentrations of atmospheric greenhouse gases (GHGs), particularly CO<sub>2</sub>, have affected the global environment, causing climate deviations and threatening the biodiversity.<sup>5</sup> If world population keeps growing at the present rate, it is estimated that by the year 2050 the global need for energy will almost double.<sup>6</sup> Hence, the need to develop renewable energy resources that do not rely on fossil fuels becomes inevitable. Solar energy has attracted interest as one such sustainable and clean energy source. The annual solar irradiation that reaches the earth is estimated to 1.5X10<sup>18</sup> kWh, exceeding global energy consumption by a factor of more than 1X10<sup>4</sup>.<sup>7</sup> Hence, it is obvious that solar light bears an enormous potential to be employed for energy generation and chemical energy storage.<sup>8</sup> Among strategies for solar energy conversion, solar hydrogen (H<sub>2</sub>) production is an attractive way to convert solar energy and store it in H<sub>2</sub>, an energy dense chemical. H<sub>2</sub> is an ideal fuel to enable a successful global net zero economy. It has a gravimetric energy density more than twice than that of conventional fuels like diesel, gasoline, and natural gas and H<sub>2</sub> is a lightweight energy carrier that can be converted to electricity and water by fuel cells.<sup>9</sup> However, as of now most of the hydrogen is produced from non-renewable sources such as natural gas by steam reforming of methane, technologies having significant CO<sub>2</sub> footprints.<sup>10</sup> Alternatively, H<sub>2</sub> can be produced by photovoltaic-assisted electrolysis (PV-E), photocatalysis and photoelectrochemical (PEC) cells, though, not cost-effectively. Based on techno-economic analyses, the cost of H<sub>2</sub> produced from renewable resources is predicted to be the lowest in a photocatalytic system with particulate catalyst.<sup>11</sup> Such approach even shows potential to meet the hydrogen price set by the United States Department of Energy.<sup>11, 12</sup> At first place the photocatalysis owes its market potential in H<sub>2</sub> production due to the low operational cost comparing with either PV-E or PEC.<sup>13</sup> Furthermore, photocatalysis allows the use of a broad range of raw materials for H<sub>2</sub> production from water to biomass, thus opening-up new opportunities for switching from fossil fuels to hydrogen economy.<sup>14</sup>

## 1.2 Heterogeneous photocatalysis

In a classical catalysis, reaction kinetics is improved by lowering the activation barrier of the reaction via an energetically more favorable reaction pathway. Thus, by definition, catalysts can catalyze only a thermodynamically spontaneous reactions, referred often as downhill. Downhill reactions are those reactions where the change of Gibbs free energy is negative ( $\Delta G_0 < 0$ ). In photocatalysis, light of a specific wavelength is utilized for chemical reactions. The photons bear excess energy which is then transferred to the photocatalyst. Therefore, beside downhill reaction photocatalysts can often facilitate reactions with positive change of Gibbs energy (uphill reaction). A typical example for uphill reactions is water splitting into hydrogen and oxygen, which will be further discussed.<sup>15</sup> Since uphill reactions are inherently non-spontaneous without energy input of light, similarly to the natural photosynthesis, they are sometimes called "artificial photosynthesis" in the literature.<sup>16</sup> The ability of photocatalysts to activate reactions with positive change in Gibbs energy is based on spatial separation of the oxidation and reduction half reactions, generation and inclusion of electronically excited state in the reaction pathway.<sup>17</sup> Therefore, the complex nature of the reactions in a practical sense is setting numerous requirements on the semiconducting photocatalyst: not only does it have to absorb maximum amount of the solar spectrum to generate photoexcited charge carriers, efficiently separate and transfer them to the surface but it has also to expose active catalytic sites on the surface where redox reactions occur and to allow for optimal adsorption and desorption of reactants and reaction products, respectively. In the following these aspects of heterogeneous photocatalyst will be explained in more detail.

### 1.2.1 Light absorption, solar spectrum and air mass

Photocatalysis starts with the activation of photocatalyst through the illumination with light of specific wavelengths. Semiconductors are very often used as heterogeneous photocatalysts. In semiconductors, absorption of photon of energy higher than the band gap between conduction band (CB) and valence band (VB) excites the electron from VB to the CB while leaving the positive hole in VB. Ideally, the light that is required for heterogeneous photocatalytic processes should be provided by solar irradiation. As already mentioned, the sun irradiation bears an enormous energy potential. By every fusion reaction of protons into helium that occurs in the sun a net energy of 26.7 MeV is generated according to equation 1.1:



where  ${}^1\text{H}^+$  is a proton,  $e^-$  is an electron,  ${}^4\text{He}^{2+}$  is a helium,  $\nu_e$  is an electron neutrino, and  $\gamma$  is a gamma ray photon.

The nuclear reactions proceed with a loss of sun mass at a rate of  $4 \times 10^3 \text{ kg s}^{-1}$ , where the sun mass is estimated to be around  $2 \times 10^{30} \text{ kg}$ .<sup>14</sup> The solar radiation is relatively uniform in the space. However, the terrestrial sunlight radiation intensity fluctuates periodically due to earth motion. Furthermore, it depends on the characteristics of the atmosphere, where factors like latitude, declination, weather conditions should be taken into consideration (fig 1, left).<sup>18</sup> In general, the longer the path lengths the light traverses through terrestrial atmosphere, the larger the loss of the sunlight due to scattering and absorption. Therefore, the solar radiation that reaches the earth's surface without being absorbed or scattered is called direct radiation. Otherwise, it is called diffuse radiation. Solar radiation in the vacuum considering the absence of the atmosphere is conventionally measured at the distance of 1 UA (astronomical unit, representing the average sun-earth distance of  $1.5 \times 10^6 \text{ km}$ ). The radiation outside the atmosphere at 1 UA is  $1.367 \text{ kWm}^{-2}$ . This is called a solar constant. On earth surface, the average radiation is attenuated to about  $1 \text{ kWm}^{-2}$ .<sup>19</sup>

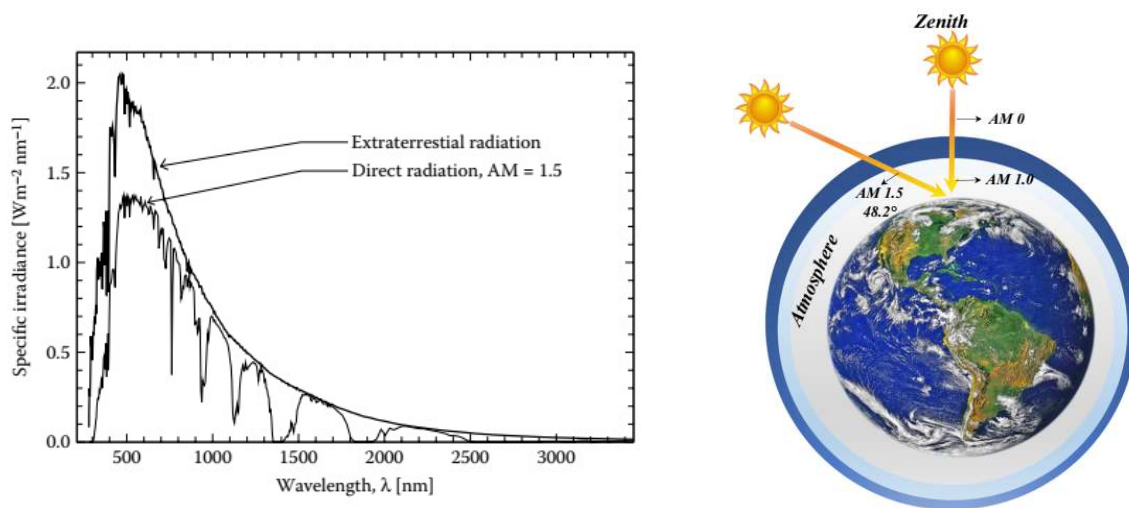


Figure 1. Comparison of extraterrestrial and direct AM 1.5 solar irradiation spectrum (left). Reproduced from<sup>7</sup> ©2011 CRC Press; the visual representation of AM 0, AM 1, and AM 1.5 (right). Reproduced from<sup>19</sup> ©2021 Elsevier

A measure of attenuation of light by the atmosphere is air mass (AM) and relates to the optical path length through the atmosphere determined by the zenith angle (fig. 1, right). The AM can be calculated according to equation 1.2:

$$AM = \frac{1}{\cos \zeta} \quad (\text{eq. 1.2})$$

where  $\zeta$  is the angle between the overhead and actual position of the sun (solar zenith angle).

Accordingly, due to the lack of the atmosphere, the AM value in vacuum is zero. In the case the sun is at a zenith light traverses the shortest path through atmosphere and AM = 1, while for the solar zenith angle of 48.2 degrees the AM equals 1.5. AM 1.5 was introduced in the 1970s based on a solar irradiation analysis, describing well the overall annual average, considering the variation of the earth-sun distance with season. Ever since the AM 1.5 spectrum is indispensable in standard photovoltaic and solar energy conversion tests.

### 1.2.2 Band structure and Fermi level

An important criterion to characterize solid materials is their electrical conductivity, which is related to the distribution of electrons in the material. Solids can be considered as a network of atoms, in which their number determines behavior and properties of the material. According to molecular orbital theory, molecular orbitals (MOs) are formed by a linear combination of atomic orbitals (AOs) in a way that the number of formed MOs equals to the number of contributing AOs. Furthermore, according to the Pauli principle of exclusion two electrons cannot be identical, which means that at least one quantum number out of four has to be different. Therefore, the larger the number of atoms that material is consisted of, the larger the overlapping of electronic states and smaller the energy difference between VB and CB. In a semiconductor at 0 K all filled states form the VB while the unoccupied states form CB. The ratio between the number of filled energy levels ( $n_{\text{filled}}$ ) to the number of total energy levels ( $n_{\text{total}}$ ) as a function of temperature in a semiconductor is described by Fermi-Dirac statistics (eq. 1.3):<sup>7</sup>

$$\frac{n_{\text{filled}}}{n_{\text{total}}} = \frac{1}{1 + e^{\frac{(E-E_F)}{kT}}} \quad (\text{eq. 1.3})$$

where  $E_F$  is Fermi level and  $k$  is the Boltzmann constant.

In materials at  $T > 0\text{K}$  these energy bands may either overlap or be separated, resulting in electronic structures of metals, semiconductors, or insulators (fig. 2, top). For semiconductors and insulators, VB and CB are separated by the band gap ( $\Delta E_g$ ), which defines the energy that is required to excite an electron from VB into CB. In photocatalysis, for instance, if a VB electron can be excited with a UV/Vis photon, then material is considered to be a semiconductor. Otherwise, it is regarded as insulator.

Apart from the band structure, a relevant parameter of semiconductors is the position of the Fermi level within the band gap. From a perspective of thermodynamics, the Fermi level will describe the electrochemical potential of electrons in the solid.<sup>7</sup> In the case that the semiconductor material has the same effective densities of states in the CB and VB, the Fermi level is located on the half way from VB and CB and the material is referred to as an intrinsic

semiconductor. However, when the semiconductor is, for example doped, the position of the Fermi level may differ in terms of the properties of the doping element (fig. 2, bottom). Thus, if the dopant accepts electrons from the semiconductor this results in the shift of the Fermi level closer to the VB, yielding an excess of positive charge and making the material a p-type semiconductor. Conversely, when the dopant donates electrons to the semiconductor the Fermi level is then pushed closer to the CB due to the excess negative charge resulting in an n-type semiconductor.

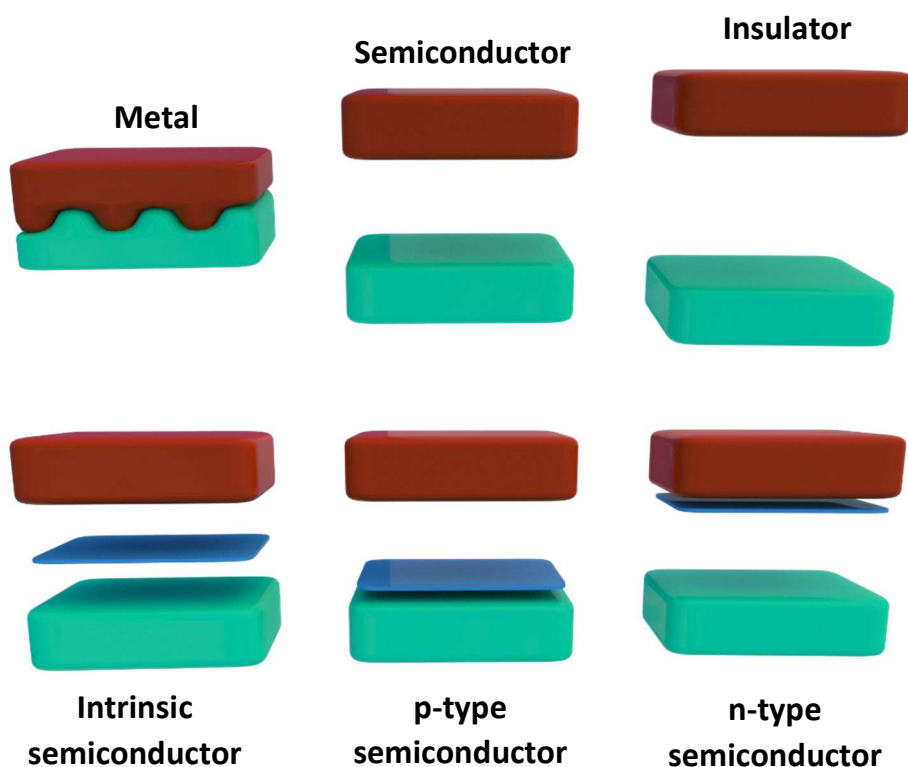


Figure 2. Band models for metal, semiconductor, and insulator (top) and positions of Fermi level in intrinsic, p-type, and n-type semiconductors (bottom). Teal, orange and blue rectangles represent valence band, conduction band and Fermi level, respectively.

### 1.2.3 Thermodynamic aspects of heterogeneous photocatalysis

Electrons from VB can be photoexcited into CB if a spectral energy greater than the band gap of the semiconductor is applied, leaving positively charged holes in the VB (fig. 3, top left). Regardless of the energy state within the conduction band which the electron is excited to, it will instantaneously relax to the bottom of the conduction band.<sup>20</sup> Thus, the most important states from the photocatalysis point of view are conduction band minimum (CBM), in the case of TiO<sub>2</sub> made up by the Ti 3d states, and valence band maximum (VBM), made up by O 2p states.<sup>21</sup> The optical transitions in semiconductors are often classified in two groups, direct and indirect transitions. In the case that transition does not require a change in

momentum, it is referred as being direct. Conversely, the indirect transition beside photon also requires an additional phonon.<sup>22</sup>

After the charge carriers are photogenerated it is most desirable that the excited carriers become spatially separated and migrate to the surface of the semiconductor, where they can take part in a charge transfer reaction with adsorbed species (fig. 3, right). However, charge transfer competes with charge recombination, phenomena where oppositely charged carriers react with each other whereupon they lose their potential for chemical reaction. Charge recombination can already occur in the bulk of the semiconductor, known as volume recombination (VR), or it can happen on the surface of the semiconductor, known as surface recombination (SR). A variety of factors such as charge carrier concentration, their mobility, defect density, trapping properties and electrical fields can influence the rate of recombination in a semiconductor.<sup>23</sup> Therefore, a material dependent quantity of the recombination probability, “diffusion length”, is introduced to describe the average distance that charge carriers can migrate before a recombination event occurs.<sup>24</sup> In this respect, it may be beneficial to use nanomaterials for photocatalysis: if the particle size is smaller, then the distance that the charge carriers need to migrate before they reach the surface is shorter and the ratio with respect to the diffusion length is more favorable.<sup>25</sup> Alternatively, it may be possible to improve charge transport by doping the semiconductor.<sup>26</sup> Then the charge carriers can migrate over larger distances having a higher chance to reach the semiconductor surface.

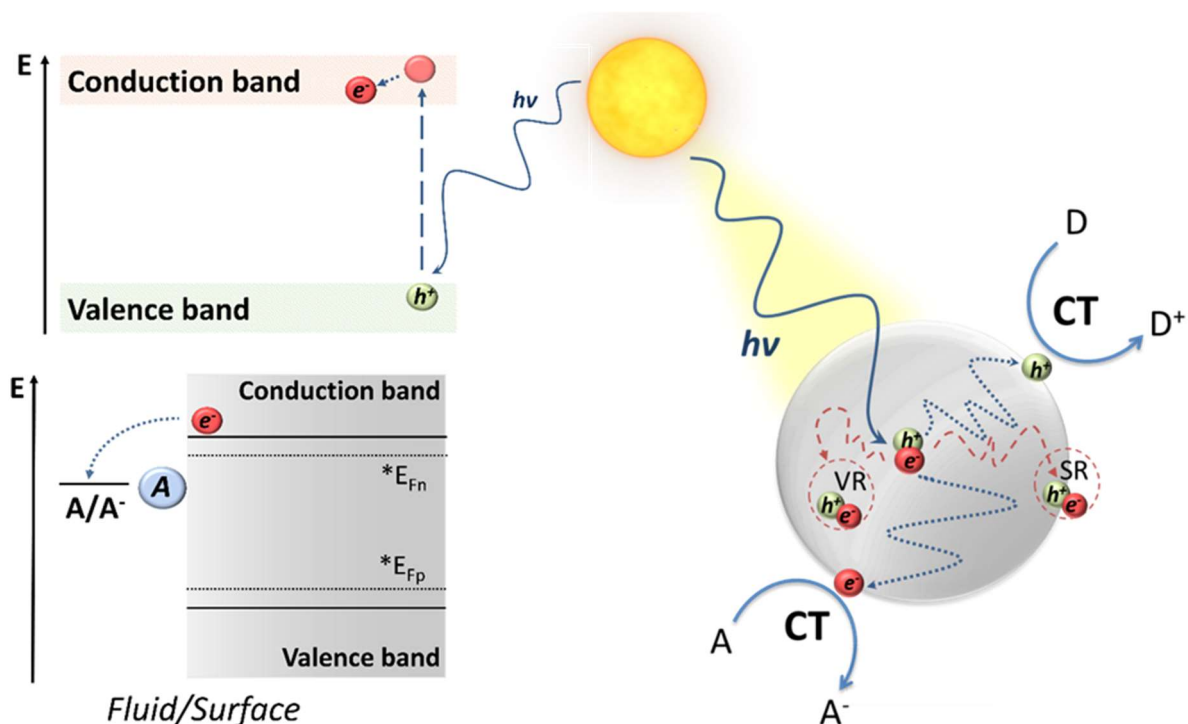


Figure 3. Schematic representation of the processes occurring in heterogeneous photocatalysis. Adapted from<sup>20</sup>

To carry out redox reactions, the involved energy levels should be positioned in the proper way to make reduction and oxidation reactions thermodynamically feasible (fig. 3, bottom left). The thermodynamic requirement for spontaneous electron flow is that the electron always has to fall down to a lower energy level.<sup>22</sup> Applied to photocatalysis, the principle implies that a reduction reaction on the surface of the semiconductor is feasible if the excited electron is at a more negative potential than the acceptor level of the molecule to be reduced, while for the oxidation reaction the electron in the donor level of the molecule to be oxidized has to be at a more negative potential to fill up the hole in the semiconductor valence band. This is usually described in the way that it is necessary that the band edges straddle the redox potentials of the desired reaction.<sup>22</sup> Apart for thermodynamics, due to the kinetic barriers it is often needed that an overpotential for the oxidation or reduction reaction is applied. An active photocatalyst reduces the required overpotential, however, running the reactions without any overpotential is not possible even in the case of the best catalysts.<sup>24</sup>

When excited, the overall concentration of charge carriers in the semiconductor can increase, leading to a non-equilibrated thermodynamic potential. In that case positions of the CBM and VBM should not be taken as a definite factor that describes the feasibility of the reaction, but instead quasi-Fermi-levels related to the electrons  $E_{F,n}$  and holes  $E_{F,p}$  should be considered instead (fig. 2, bottom).<sup>7</sup> The quasi-Fermi-levels align to  $E_F$  with increasing distance from the surface of the semiconductor due to the low penetration depth of photons into a semiconductor, so that the excitation is limited to the volume close to the surface of the material.<sup>21</sup> In some cases, however, the concentration of majority carriers consisting of electrons in the case of n-type semiconductors or holes in case of p-type semiconductors, is not significantly increased due to the excitation. For this reason taking the position of the band edges for thermodynamic feasibility of the reaction is a good approximation, especially in the case of  $\text{TiO}_2$ .<sup>21</sup>

#### *1.2.4 Mass transport*

Apart from the requirement that charge carriers have to exist sufficiently long and reach the semiconductor's surface, they need to be used for a specific chemical reaction at a catalytically active site on the surface that adsorbs the reactants, stabilizes the reaction intermediates, and desorbs the reaction products. Thus, the overall heterogeneous catalytic process includes not only the photophysical aspect but also mass transport.<sup>27</sup> The mass transport on the heterogeneous catalyst in liquid phase can be presented with 5 principal steps: (1) transport of the reactant through the fluid bulk to the boundary layer, (2) diffusion of the reactant through the boundary layer to the surface of the catalyst and adsorption on the active catalytic site, (3) catalytic surface reaction, (4) desorption of the product from the surface of the catalyst and diffusion through the boundary layer and (5) transport of the product back into the fluid bulk (fig. 4).

Heterogeneous catalysts often possess structural diversity with a plethora of different structural and electronic arrangements of surface atoms that are potentially favorable to direct the reaction to the desired pathway. The active sites are not necessarily located at ideal crystal surfaces, but instead they can be found at a defective site or even at a motif such as vacancies, kinks, and steps. In general, common for all the defective sites is that atoms at such sites are undercoordinated.<sup>28</sup> The more atoms the site is missing, the higher the affinity of the atoms to fill up their coordination spheres by adsorption. However, adsorption strength for reactants and reaction products should be tailored with special care, otherwise the overall reaction can be adversely affected. For example, in the case that a reactant is bonded weakly to the catalyst surface, it may result in a lack of the reactant for the reaction leading to an inefficient catalytic process. On the other hand, if a reactant is bonded too strongly to the surface of the catalyst, the catalyst can become poisoned by the reactant, preventing the reaction to occur. Finally, in the case where products are adsorbed too strongly to the surface of the catalyst, active sites at the catalyst surface cannot be re-formed for the next catalytic cycle, resulting in the inactivation of the catalyst.

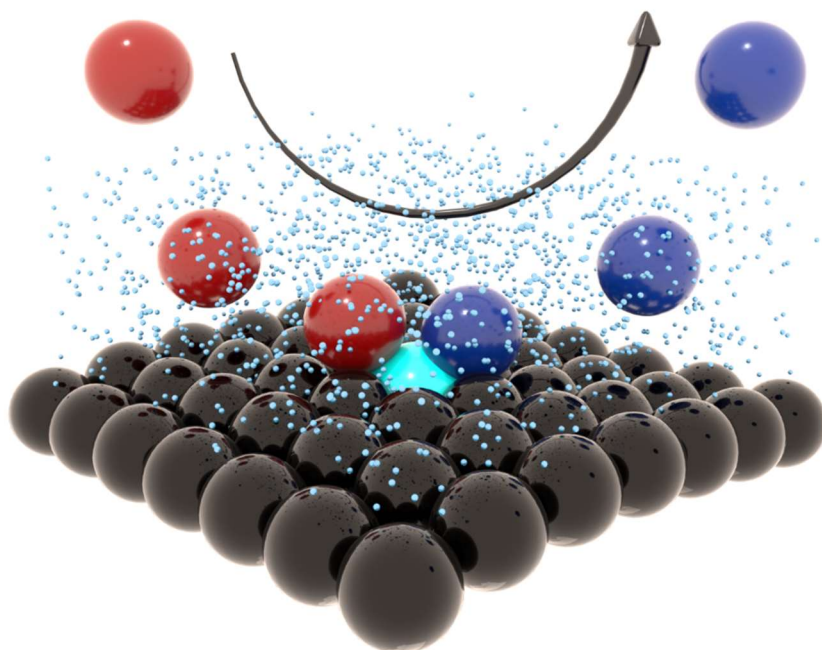


Figure 4. Schematic representation of an overall heterogeneous catalytic process at a catalyst surface. Black and teal spheres represent the catalyst surface and catalytically active site. Red and blue spheres are reactant and reaction product, respectively. Small blue spheres build a boundary layer. The arrow indicates the direction of the catalytic process.

Adapted from<sup>27</sup>



## 1.3 TiO<sub>2</sub> as a photocatalyst

TiO<sub>2</sub> is one of the most researched metal oxide semiconductor materials. It is naturally abundant, accessible and does not pose environmental risk. Due to its high refractive index, more than half of the produced TiO<sub>2</sub> is used for pigments and coatings. TiO<sub>2</sub> shows extraordinary optical and electrical properties, as well as high tolerance towards a wide range of application conditions, which pave its way to advanced technology applications such as water and air purification, gas sensing, photovoltaics and photocatalysis.

After five decades from the first specific utilization of TiO<sub>2</sub> properties in photocatalysis that was introduced in Honda's and Fujishima's pioneering work in the field of water splitting, this first generation of TiO<sub>2</sub>-based materials was then further explored for its performance in e.g., CO<sub>2</sub> reduction.<sup>29 30</sup> Since then, TiO<sub>2</sub> has been utilized in heterogeneous photocatalysis also as promotor, additive and supporting material.<sup>28</sup>

Among the three photocatalytically most relevant polymorphs of titanium dioxide, rutile, anatase, and brookite, anatase is believed to be the photocatalytically most active one.<sup>21</sup> It possesses a tetragonal crystal structure and can be regarded as a heavy n-type semiconductor, mainly due to its numerous defect sites. Anatase has long-lived photogenerated charge carriers and can be easily synthesized in sub-10 nm range which are considered as the main driving forces for efficient photocatalysis. However, long-lived holes in rutile TiO<sub>2</sub> are beneficial, for example, in a multi-hole process such as water oxidation.<sup>31</sup> Beside structure and charge dynamics, TiO<sub>2</sub> properties such as band gap and band positions are important parameters in determining if this photochemical system is suitable for the given reaction.<sup>21, 32</sup> Therefore, this chapter will introduce the crystal phases of TiO<sub>2</sub>, solar light harvesting by TiO<sub>2</sub>, charge carrier dynamics, trapping, recombination as well as a concept of TiO<sub>2</sub> band bending .

### 1.3.1 Crystal phases of TiO<sub>2</sub>

TiO<sub>2</sub> crystals are based on different spatial stacking arrangement of Ti polyhedra, with six- to nine-fold coordinated titanium cations with oxygen atoms forming in total 11 polymorphs of TiO<sub>2</sub>.<sup>33</sup> Beside the three photocatalytically relevant polymorphs, rutile, anatase and brookite, TiO<sub>2</sub> has 3 more crystalline forms that are stable at atmospheric pressure: TiO<sub>2</sub> (B), hollandite-like TiO<sub>2</sub> (H), ramsdellite-like TiO<sub>2</sub> (R) as well as five high-pressure TiO<sub>2</sub> phases: columbite-like TiO<sub>2</sub> (II), baddeleyite-like TiO<sub>2</sub> (OI), cotunnite-like TiO<sub>2</sub> (OII), and fluorite-like cubic phases. Among the TiO<sub>2</sub> polymorphs, the rutile phase is the most common phase that appears in nature.<sup>7</sup> The natural rutile crystals are usually impure, which greatly limits their application. Pure synthetic rutile TiO<sub>2</sub> can be produced on industrial scale from ilmenite (FeTiO<sub>3</sub>) by the

chloride or sulfate process.<sup>7</sup> In the chloride process  $\text{FeTiO}_3$  is chlorinated to  $\text{TiCl}_4$ , further purified and burned to  $\text{TiO}_2$ . In the sulfate process, instead,  $\text{FeTiO}_3$  is dissolved in sulfuric acid, whereby titanyl sulfate is formed and precipitated. Afterwards a calcination step to  $\text{TiO}_2$  is conducted. Alternatively, rutile  $\text{TiO}_2$  can be produced from anatase by thermal treatment.<sup>34</sup> The enthalpy of formation increases in the order  $\Delta H_f(\text{rutile}) < \Delta H_f(\text{brookite}) < \Delta H_f(\text{anatase})$ , while the surface energy reveals the reverse trend.<sup>35</sup> The latter induces an effect on the crystal formation especially for very small particles. On this account, it is proposed that  $\text{TiO}_2$  particles less than 11 nm in size are thermodynamically the most stable as anatase, between 11 and 35 nm as brookite, and at sizes greater than 35 nm as rutile.<sup>36</sup> Furthermore, the synthesis of pure phases can be limited by impurities consisting of the other phases which is typically the case with brookite. Therefore, only bulk and surface crystal structure of rutile and anatase polymorphs will be further discussed.

### 1.3.1.1 Rutile $\text{TiO}_2$

Rutile crystals are formed by chains of distorted  $\text{TiO}_6$  octahedra where each Ti atom is surrounded by 6 oxygen atoms. Rutile has a tetragonal structure with space  $D_{4h}^{19} - P4_2/mnm$  space group (fig. 5, top left). A unit cell of rutile  $\text{TiO}_2$  contains two  $\text{TiO}_2$  units. Each O atom is coordinated to three Ti atoms through one long (apical) and two short (equatorial) bonds. The stacking of the octahedra in rutile is shown in fig. 5, bottom left. Here, each  $\text{TiO}_6$  octahedron is in contact with 10 neighbors, with two of them sharing oxygen edge pairs while with eight sharing corner oxygen atoms. In this way rutile forms channels along the c-crystal axis.<sup>37</sup> The density of the rutile phase is  $4.25 \text{ gcm}^{-3}$ . The channels allow intercalation of small atoms into the  $\text{TiO}_2$  framework such as alkaline metals. Intercalation compounds are formed with lithium (ionic radius of 76 pm) and sodium (102 pm) due to the size match with the channel diameter.<sup>38,39</sup> In the case of potassium (138 pm), which is significantly bigger than either Li or Na, intercalation in rutile and, generally in  $\text{TiO}_2$ , does not occur.<sup>38</sup>

The shape of rutile crystals plays a role in determining the surface termination (fig. 5, right). Generally, atoms in crystal bulk are coordinatively saturated, while atoms at the crystal surface may be undercoordinated. The degree of undercoordination of atoms as well as the share of undercoordinated atoms in the surface structure depends on its geometry (fig. 6). The most stable surface of a rutile crystal is a (110) surface.<sup>40</sup> It exposes two different kinds of Ti atoms, coordinatively saturated  $\text{Ti}_{6c}$  atoms, and  $\text{Ti}_{5c}$  atoms that have one dangling bond perpendicular to the surface. Furthermore, it exposes fully coordinated  $\text{O}_{3c}$  and undercoordinated  $\text{O}_{2c}$ . The  $\text{O}_{3c}$  atoms lie within the main surface plane, while the  $\text{O}_{2c}$  atoms are projected out of the plane. The  $\text{O}_{2c}$  atoms are considered to be removed easily, for instance, by thermal annealing which results in the formation of  $\text{Ti}_{5c}$  point defects and causes an increase in surface energy.<sup>40</sup> The surface, however, tends to release the excess energy by e.g. water adsorption, by which reduced  $\text{Ti}^{3+}(\text{Ti}_{5c})$  atoms are reoxidized.<sup>41</sup>

The undefective (110) surface in rutile does not dissociate water. Water dissociation is only observed on surface defect sites and it has been shown that dissociation on such sites is exothermic.<sup>42-45</sup> The reactivity of the (110) surface can be explained as follows: water molecules adsorb on  $Ti_{5C}$  surface atoms regardless if the surface is perfect or not, in the way that O-H bonds point away from the surface. In the case of an undefective surface, the distance between the hydrogen atoms in a water molecule and a bridging  $O_{2C}$  atom projected out of the surface plane exceeds 3 angstroms. Thus, this does not allow the development of hydrogen-bonding interactions between the water hydrogen atoms and bridging oxygen atoms.<sup>46</sup> These interactions facilitate the proton transfer, thus promoting the dissociation of water. Comparing with the undefective case, defective (110) surface adsorbs water molecule on  $Ti_{5C}$  atoms located at oxygen vacant site, allows hydrogen-bonding and promotes water dissociation.

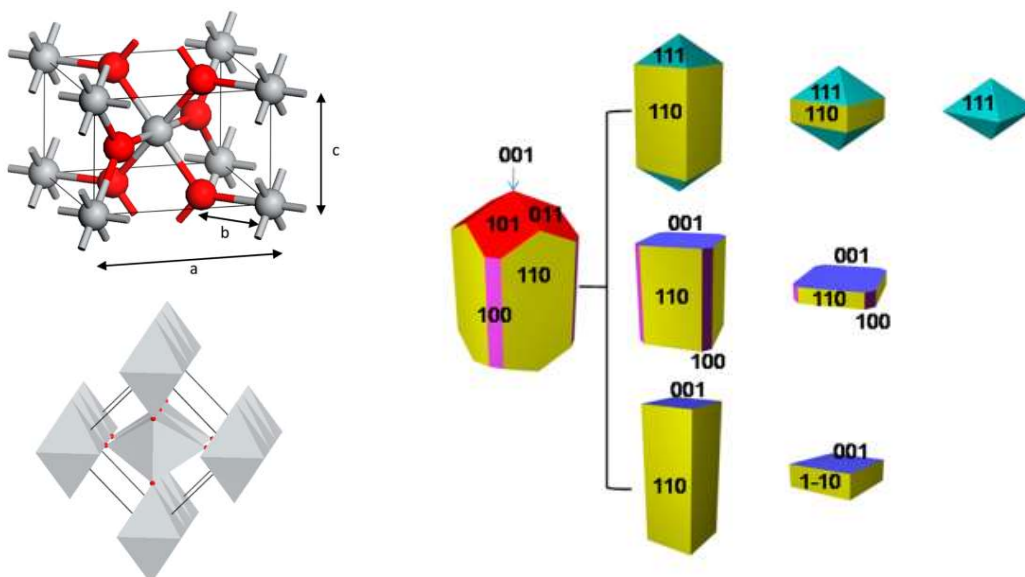


Figure 5. Unit cell (top left) and spatial arrangement of  $TiO_6$  octahedra (bottom left) in rutile  $TiO_2$ . Reproduced from<sup>40</sup> © 2014 American Chemical Society. Equilibrium crystal shape of rutile  $TiO_2$  through the Wulff construction and the evolved other shapes of rutile  $TiO_2$  (right). Reproduced from<sup>47</sup> © 2014 American Chemical Society

Beside (110) surface, (100) surface constructs the body of the rutile crystal. It is more corrugated than the (110) orientation. It consists of  $Ti_{5C}$  atoms in the center of the oxygen truncated octahedra, ridges of  $O_{2C}$  atoms in the uppermost layer, and  $O_{3C}$  atoms at a level lower than that of the  $Ti_{5C}$  atoms.<sup>40</sup> It resembles a periodic array of ridges and troughs parallel to the (001) direction. Water adsorbs on the stoichiometric (100) surface associatively, while adsorption tends to be dissociative on a surface rich in  $Ti^{3+}$  ions.<sup>40</sup>

The cap of the rutile crystal can be terminated with various surfaces. Among them following surfaces are common: (101), (011), (111), (001).<sup>48</sup> The content of undercoordinated atoms in these surfaces is higher compared with the surfaces making the body of the crystals. They usually expose  $Ti_{4C}$ ,  $Ti_{5C}$ ,  $O_{2C}$  and  $O_{3C}$  atoms, where dissociative water adsorption is more probable to occur than the associative.<sup>40</sup>

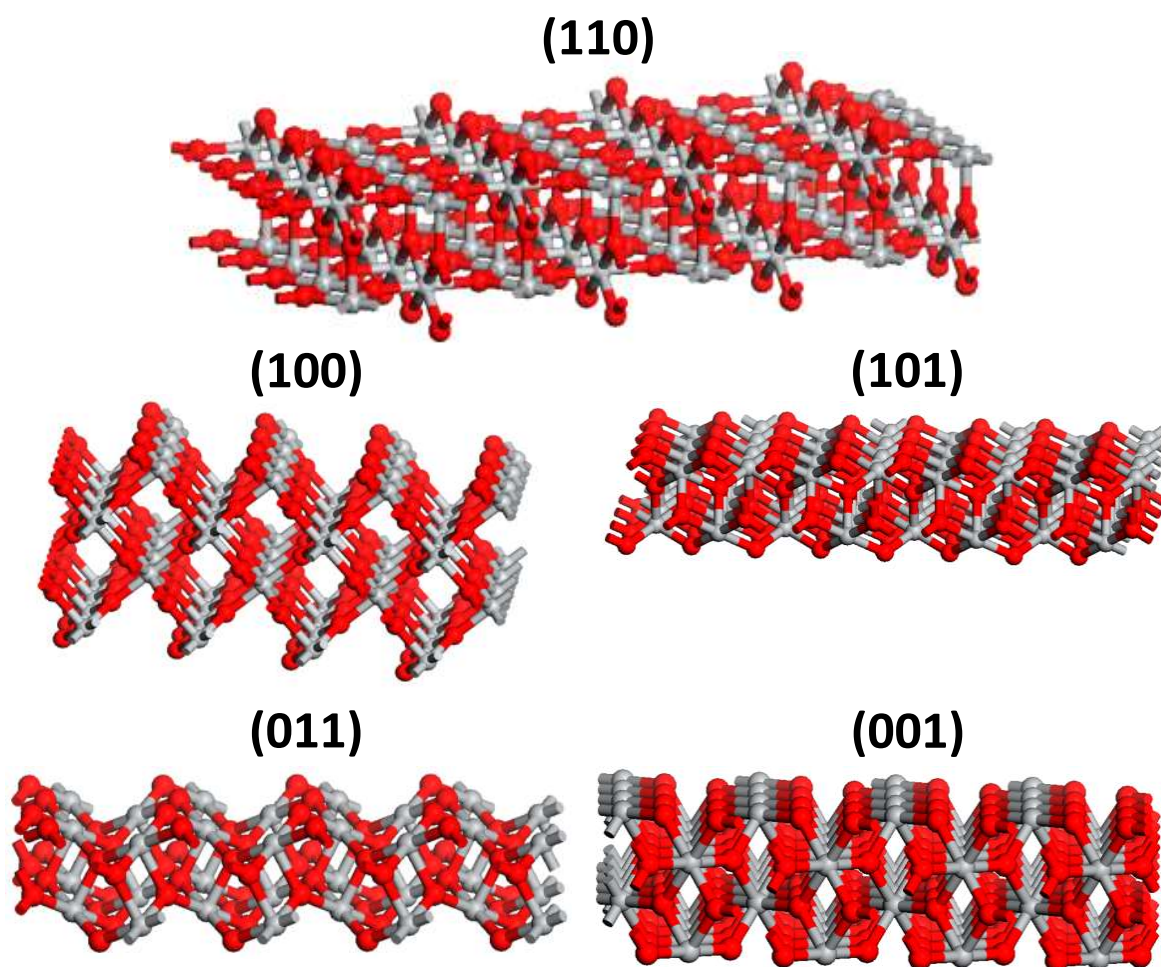


Figure 6. Schematic representation of rutile (110), (100), (101), (011) and (001) ideal surfaces. Reproduced from<sup>40</sup> © 2014 American Chemical Society

The stability of the crystal surface can be explained in terms of unsaturation density and surface energy. The unsaturation density is defined as the number of the broken bonds per  $nm^2$  of the surface titanium and oxygen atoms relative to their bulk coordination ( $Ti_{6C}$  and  $O_{3C}$ ). The unsaturation density calculated for the (110), (100), (101), and (001) surface are 10.23, 14.4, 15.59, and 18.5, respectively.<sup>49</sup> These unsaturation density values correspond well to the calculated surface energies that predicts an increase in energy in the following order:

(110) < (100) < (011) < (001).<sup>48, 50</sup> On this account, it can be concluded that surfaces at the crystal body are more stable comparing with the surfaces exposed at the crystal cap.

### 1.3.1.2 Anatase TiO<sub>2</sub> and anatase-rutile mixed-phase TiO<sub>2</sub>

Like in rutile, the anatase phase is formed by chains of distorted TiO<sub>6</sub> octahedra where each Ti atom is surrounded by 6 oxygen atoms. It has a tetragonal structure with D<sub>4h</sub><sup>19</sup> – I4<sub>1</sub>/amd space group (fig. 7, left). In the anatase phase, the conventional unit cell is composed of four TiO<sub>2</sub> units. Each O atom is coordinated to three Ti atoms lying in the same plane through one long (apical) and two short (equatorial) bonds. In anatase, the TiO<sub>6</sub> octahedron is in contact with eight neighbors, with four sharing an edge and with another four sharing a corner. By this, 3D framework structure is formed with the distorted cubic close-packed oxygen lattice.<sup>37</sup> The density of anatase is 3.89 gcm<sup>-3</sup>, which makes it less dense than the rutile phase. Moreover, the anatase structure offers 2D diffusion paths along both a- and b-axes for Na diffusion, making the Na intercalation into anatase more feasible comparing with rutile polymorph that allows intercalation only along c-axis.<sup>51</sup> Beside the bulk structure of the crystal, the energy state of exposed crystal surfaces may be relevant in promoting intercalation.<sup>52</sup> For example, it was found that the (101) surface, which exhibits low energy density, hinders sodium uptake, while the surfaces of intermediate energy, such as (100), seemed favorable for the intercalation.<sup>52 53</sup>

The anatase nanocrystals usually expose (101), (100), (001), (110), and (103) surfaces. Most of the shapes, however, exhibit the (101) and the (001) surfaces, which are of high concern in terms of application of anatase TiO<sub>2</sub>, for instance, in catalysis. Nevertheless, all anatase surfaces exhibit undercoordination.<sup>40</sup> For example, (101) surface exposes both Ti<sub>5C</sub> and Ti<sub>6C</sub>, as well as O<sub>2C</sub> and O<sub>3C</sub>. On the (001) face, Ti<sub>5C</sub>, O<sub>2C</sub> and O<sub>3C</sub> are exposed, while Ti<sub>4C</sub> and O<sub>2C</sub> are exposed on the first layer of the (110) surface. Following the principle of unsaturation density, the calculated surface energies in an anatase crystal are proposed to increase in the order: (101), (100), (103)<sub>faceted</sub>, (001), (103)<sub>smooth</sub>, and (110) surface, indicating that the (101) surface is the most stable one.<sup>54-56</sup>

A very prominent type of polycrystalline titania is a titania composed of anatase and rutile phases. The most important mixed-phase titania formulation is AEROXIDE® TiO<sub>2</sub> P25 (abbreviated: P25). Originally, it is produced by Degussa, now part of Evonik Industries. P25 shows high photocatalytic activity for a range of reactions and possesses remarkable stability against corrosion.<sup>32, 57, 58</sup> Given its high potential in photocatalysis, effort has been made to determine the phase composition as well as interface connections between anatase and rutile. On one hand, a general consensus considers P25 as a powder with variable phase composition.<sup>59</sup> Typically, it consists of anatase and rutile in the ratio 80:20 to 70:30. Moreover, some small amounts of amorphous phases have also been found in P25.<sup>59</sup> On the other hand, the exact character of interface and charge flow are not fully understood yet. It was proposed

that P25 consists of a unique microcrystalline structure, where the anatase crystallites are in an intimate contact to an overlayer of rutile or an anatase-rutile interparticle contact is established.<sup>60, 61</sup> Conversely, it was also shown that P25 contains separated particles, where either the anatase or the rutile structure exists.<sup>62</sup> However, as in most of the cases, the truth might be somewhere in between. Most likely, individual anatase and rutile particles comprise the majority of P25, but also minor amounts of anatase-rutile heterojunction structures could be formed.<sup>63</sup> Nevertheless, the anatase-rutile interface and band alignment can direct the charge flow in the mixed-phase  $\text{TiO}_2$ , thus influencing the charge separation and photocatalytic activity. Initially, a type-II (rutile) band alignment was suggested, which considers transfer of photogenerated electrons from anatase to rutile, and the transfer of photogenerated holes from rutile to anatase.<sup>64</sup> More recently, a type-II (anatase) band alignment has been reported as well. Here, the electrons flow from rutile to anatase, with holes moving in the opposite direction.<sup>65, 66</sup> Despite the fact that fundamentals of P25 remain controversial up to now, P25 is still one of the most widely applied  $\text{TiO}_2$  catalysts, often serving as a benchmark. However, clarification of the structure-function relationship of P25 will be an impetus for understanding of  $\text{TiO}_2$  behavior in photocatalytic reactions and will allow knowledge-guided design of  $\text{TiO}_2$  catalysts in the future.

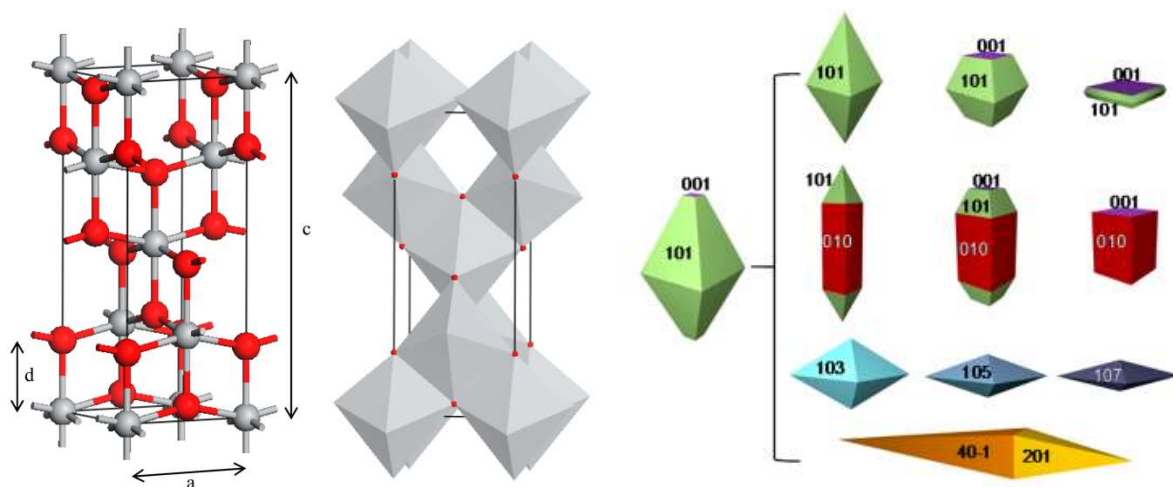


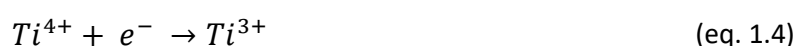
Figure 7. Unit cell (left) and spatial arrangement of  $\text{TiO}_6$  octahedra (middle) in anatase  $\text{TiO}_2$ . Reproduced from<sup>40</sup> © 2014 American Chemical Society. Equilibrium crystal shape of anatase  $\text{TiO}_2$  through the Wulff construction and the evolved other shapes of anatase  $\text{TiO}_2$  (right). Reproduced from<sup>47</sup> © 2014 American Chemical Society

### 1.3.2 Solar light harvesting by $\text{TiO}_2$

With a bandgap of 3.2 eV, anatase  $\text{TiO}_2$  has a light absorption onset at 384 nm. Such light falls in the ultraviolet spectral region and limits efficient solar light utilization by  $\text{TiO}_2$ . Poor light

utilization decreases its solar photocatalytic activity as well.<sup>32</sup> Therefore, the light harvesting ability of TiO<sub>2</sub> has been often modulated via bandgap engineering by e.g. TiO<sub>2</sub> doping. The doping of TiO<sub>2</sub> with both, non-metals and metals, has been extensively investigated in the past.<sup>67-69</sup> The VB of TiO<sub>2</sub> is composed of O 2p orbitals and the CB is formed from Ti 3d orbitals. Thus, doping with non-metals and metals will affect the band structure differently. TiO<sub>2</sub> doping with anions usually affect the VB and introduces impurity states within the bandgap at different energy levels depending on the dopant.<sup>70</sup> For example, TiO<sub>2</sub> doping with nitrogen introduces N 2p electronic states that are almost fully localized on N atoms and lie few tenths of an eV above the VB of TiO<sub>2</sub>.<sup>71</sup> Moreover, doping with two nonmetal elements or a combination of nonmetals and metals have been demonstrated to enhance the visible light absorption of TiO<sub>2</sub> material.<sup>72-74</sup> In the case of metal doping, Ti<sup>4+</sup> cations in TiO<sub>2</sub> are replaced, typically with other transition-metal cations, and electronic states of dopants are introduced within the TiO<sub>2</sub> band gap. The in-band state can then act as an electron donor or electron acceptor, thus enhancing light harvesting ability of doped TiO<sub>2</sub>. In Cr<sup>3+</sup>-doped TiO<sub>2</sub>, for instance, the visible light absorption is attributed to the photoinduced transition of Cr<sup>3+</sup> 3d electrons into CB of TiO<sub>2</sub>.<sup>75</sup> Similar to the nonmetals, TiO<sub>2</sub> doping with two metals has been found beneficial for TiO<sub>2</sub> light harvesting.<sup>76</sup> However, despite being beneficial in terms of light harvesting, the doping with foreign elements often reduces the efficiency of TiO<sub>2</sub> photocatalytic activity. The acknowledged challenges regarding the doped-TiO<sub>2</sub> includes material's instability and introduction of deep localized levels that act as charge carrier recombination centers.<sup>77</sup> Furthermore, the thermodynamic and kinetic inability of such states to participate in the redox reactions have been recognized as factors as well.<sup>77, 78</sup>

A new paradigm in TiO<sub>2</sub> doping has been introduced by self-doping.<sup>79</sup> The self-doping, in general, implies doping of the materials with the same atom that composes the material, but in a different oxidation state. In the case of TiO<sub>2</sub>, self-doping introduces Ti<sup>3+</sup> cations on the expense of Ti<sup>4+</sup> sites, also introducing disorder into the TiO<sub>2</sub> framework. Moreover, the Ti<sup>3+</sup> states form new energy states 0.8 to 1.2 eV below CB of TiO<sub>2</sub>, responsible for the blue color of the self-doped TiO<sub>2</sub>. The reduction of Ti<sup>4+</sup> to Ti<sup>3+</sup> cation is given by following equation:



Electrons necessary for Ti<sup>4+</sup> reduction to Ti<sup>3+</sup> state can be typically provided either by treatment of TiO<sub>2</sub> in reducing atmosphere at high temperatures and pressures, or by a reaction with reducing agents, although methods such as vacuum annealing, high energy particle bombardment or combustion have been also applied.<sup>79-83</sup> For practical application, strategies relying on reducing atmosphere or particle bombardment have limitations in the way that complicated and expensive facilities are often required. Therefore, a more convenient approach employing a reducing agent can in prospective fill the gap. Moreover, the selection of reducing reagents that can facilitate Ti<sup>4+</sup> reduction to Ti<sup>3+</sup> is rather broad. For

example, hydride-based inorganic reductants such as  $\text{NaBH}_4$  or hydrogen-free active metals like Li, Na, Mg, Al have been employed.<sup>81, 84-89</sup> Experimental conditions for  $\text{TiO}_2$  self-doping depend on the potential of the reducing agent. Thus, Mg or Al need higher temperatures to facilitate  $\text{Ti}^{4+}$  to  $\text{Ti}^{3+}$  transition due to their lower reducing ability, while alkaline metals possess enough reducing power to run the reaction already at room temperature. Although it can be expected that self-doped  $\text{TiO}_2$  are not stable materials under storage or operational conditions, in fact, they show high stability against  $\text{Ti}^{3+}$  reoxidation as well as color bleaching.<sup>81, 86, 87</sup> As mentioned previously, the self-doping of  $\text{TiO}_2$  unlocks visible and near-IR light absorption of the material due to the favorable position of the  $\text{Ti}^{3+}$  states within the bandgap, making self-doped  $\text{TiO}_2$  one of the best known solar light absorbers amongst  $\text{TiO}_2$  materials, with a light absorption that covers over 60% of the whole solar spectrum.<sup>86</sup> Also, self-doped  $\text{TiO}_2$  exhibits high photocatalytic activity e.g. for solar  $\text{H}_2$  production.<sup>79, 81, 84-86, 90</sup> In general, in self-doped  $\text{TiO}_2$  the influence of doping except with  $\text{Ti}^{3+}$  is often neglected, due to the convenience of capturing excess electrons by  $\text{Ti}^{4+}$  centers. However, doping with, for instance, used reducing agent could be a reason for the high stability and good photocatalytic performance of self-doped  $\text{TiO}_2$ .

Choosing  $\text{TiO}_2$  polymorphs with more favorable optical properties such as rutile can be an alternative approach to  $\text{TiO}_2$  doping. The bandgap in rutile is 3.0 eV, 0.2 eV narrower than that of anatase  $\text{TiO}_2$ . The energy of 3.0 eV corresponds to the light absorption onset at 410 nm. Therefore, in comparison with anatase, the absorption onset in rutile is 25 nm red-shifted. The main drawback of rutile  $\text{TiO}_2$  despite being the most thermodynamically stable polymorph with promising light harvesting capabilities, is fast recombination of the photogenerated charge carriers, which hinders its application in photocatalysis.<sup>91-93</sup> The charge carrier recombination in  $\text{TiO}_2$  and strategies for its improvement will be discussed next.

### *1.3.3 Charge carrier dynamics, trapping and recombination*

Band-gap illumination of  $\text{TiO}_2$  results in the photogeneration of charge carriers (eq. 1.5). The charge carrier generation is a very fast process taking place at femtosecond scale.<sup>69</sup> Afterward, carriers can follow one of the following scenarios: freely move through the crystal; couple with the crystal lattice (eq. 1.6-1.7); or annihilate by recombination (eq. 1.8).<sup>91-94</sup> For instance, free electrons can interact with Ti 3d orbitals of lattice  $\text{Ti}^{4+}$  ions forming  $\text{Ti}^{3+}$  ions. Charge-phonon interactions are usually referred to as polarons, and depending on the degree of charge localization small or large polarons form.<sup>94</sup> The configuration of a small polaron implies that the coupled electron resides in close proximity of the trapping lattice site. Moreover, the small polaron can be activated e.g., thermally or optically, when it starts to exhibit hopping mobility. In the case that electron hopping occurs over a large number of lattice sites, such polaronic configuration is then considered to be a large polaron. The energy required to activate a small polaron describes the strength of charge-phonon interactions. In the case that thermal energy

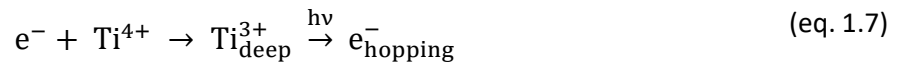
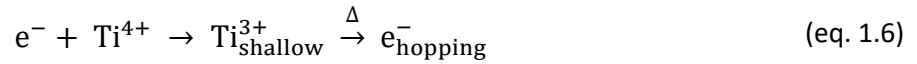


is sufficient for activation, the small polaron is considered as a shallow trap. Conversely, the small polaron is a deep trap if optical energy is necessary for its activation.

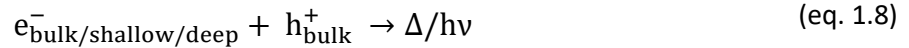
Photogeneration of charge carriers:



Trapping of electrons:



Bulk charge recombination:



In  $\text{TiO}_2$ , a considerable amount of photogenerated charge carriers spontaneously recombine directly or at the trapping sites releasing the excess energy in the form of heat or light. Although the recombination can occur in the bulk or at the surface, the bulk recombination is rather dominant pathway in  $\text{TiO}_2$ .<sup>91, 93</sup> The charge carrier lifetimes and decay kinetics strongly depend on the  $\text{TiO}_2$  crystal phase. In anatase electrons show slow nonexponential decay kinetics with a fraction of long-lived electrons that can survive more than 1 ms.<sup>91, 93</sup> On one hand, the slower decay kinetics is assigned to a bimolecular mechanism, where two fully dissociated charge carriers directly recombine.<sup>91, 95</sup> On the other hand, a multiple-trapping-dominated charge transport mechanism that involves shallow trapping states has been suggested to allow electrons to avoid quick recombination.<sup>92, 93</sup> Based on this mechanism, it is expected that the use of nanoparticles may be beneficial to prolong charge carrier lifetimes, since nanoparticles have a higher defect density comparing with e.g. defect-free single crystals.<sup>93</sup> In the case of rutile, electrons and holes exhibit fast exponential decay kinetics.<sup>92</sup> Thus, photogenerated charge carriers in rutile live shorter than in anatase, and free electrons live shorter comparing with holes.<sup>92, 96</sup> In fact, free electrons become deeply trapped within few picoseconds presumably due to the high density of bulk defects.<sup>23, 91, 97, 98</sup> Then, trapped electrons in form of small or large polarons recombine with free holes.<sup>96</sup> Hence, unlike for anatase, reducing the number of crystal defects is considered an effective way to suppress recombination in rutile.<sup>99</sup> Alternatively, charge carrier dynamics can be improved by decreasing the size of the rutile particles.<sup>91</sup>

If charge carriers evade unfavorable trapping and recombination the valence band holes and conduction band electrons migrate to the catalyst's surface. There, they can initiate interfacial charge transfer to a surface adsorbed acceptor or donor molecule by redox reactions or undergo surface charge recombination (eq. 1.9-1.11). From a catalytic point of view, the

longer lifetime of free electrons in anatase is beneficial for the reactions where electron transfer is involved, while deep electron trapping in rutile in most of the cases fails to increase the overall activity even if lifetime of the holes is prolonged.

Redox reaction at the surface of the catalyst:



Surface charge recombination:



#### 1.3.4 Band bending in $\text{TiO}_2$

The band bending model strives to explain a behavior of electronic bands near interfaces. According to the model, bands would be flat in a stoichiometric and clean semiconductor. However, in practice that often is not the case. The band bending can be induced by e.g., deviation from stoichiometry, adsorption and desorption processes, light illumination, and metal-semiconductor interfaces. Afterwards, a redistribution of the charges within the semiconducting material occurs causing a non-equilibrated state.<sup>100</sup> To reestablish the equilibrium, electrons start to migrate from the surface to the bulk of the semiconductor, a phenomenon known as downward band bending, and from the bulk to the surface, which is referred to as upward band bending.<sup>23</sup> Eventually, the band bending can impact the separation and migration of charge carriers in a semiconductor as well as across the interface with an adsorbate and a co-catalyst, which could be beneficial for better understanding photocatalytic processes.<sup>101</sup>

The clean  $\text{TiO}_2$  surface in the dark is considered to be non-stoichiometric due to the undercoordinated surface atoms.<sup>28</sup> Such defects can be understood as unpaired electrons that predominantly reside in Ti 3d orbitals in form of  $\text{Ti}^{3+}$  cations, acting as donor-like states.<sup>40, 94</sup> As a consequence, electrons accumulate in the space charge region (accumulation layer) of  $\text{TiO}_2$  inducing the downward band bending.<sup>28</sup> However, as soon as  $\text{TiO}_2$  is exposed to the ambient atmosphere, the adsorption of present water can occur. As already discussed, water adsorption at  $\text{TiO}_2$  surface is strongly dependent on the structure of the surface. Thus, in case water adsorbs associatively at the  $\text{TiO}_2$  surface, no charge transfer is expected to happen.<sup>23</sup> The effect is ascribed to the low electronegativity of  $\text{H}_2\text{O}$  (<4.5 eV).<sup>102</sup> The water dissociation occurs only in the presence of  $\text{Ti}_{5c}$  on oxygen vacant site by a charge transfer from the 3d Ti orbitals of  $\text{Ti}^{3+}$  to the molecular orbitals of OH.<sup>103</sup> Based on this, it can be concluded that dissociative adsorption of gas phase water at  $\text{TiO}_2$  surface leads to upward band bending due

to the formation of negatively charged species at the surface and thus to the decrease of charge carrier density in the space charge layer.<sup>23</sup> Therefore, the direction in which bands are bent strongly depends on the surface composition.

When TiO<sub>2</sub> is illuminated with a light of energy higher than its band gap, photogenerated charge carriers are created in the outer surface region of the material due to the limited light penetration.<sup>21</sup> In the space charge region, charge carrier recombination is less likely to occur since electrons and holes move in different directions due to the near surface electric field. Upon continuous illumination the bands flatten resulting in the annihilation of the electric field. On one hand side the band flattening can be explained as a surface effect due to the move of free electrons to the bulk, while free holes accumulate at the surface where the negative charge is neutralized.<sup>104</sup> Alternatively, it can be explained by a band shifting in the bulk region, as the number of electrons increases in the bulk upon illumination.<sup>23</sup> Nevertheless, the TiO<sub>2</sub> behavior under illumination could indicate that photogenerated electrons in pure TiO<sub>2</sub> may not be available directly at the surface which negatively affects reduction reactions. The accumulation of electrons in TiO<sub>2</sub> occurs through formation of Ti<sup>3+</sup> ions that gradually turn the color of TiO<sub>2</sub> from white to blue.<sup>105 106</sup>

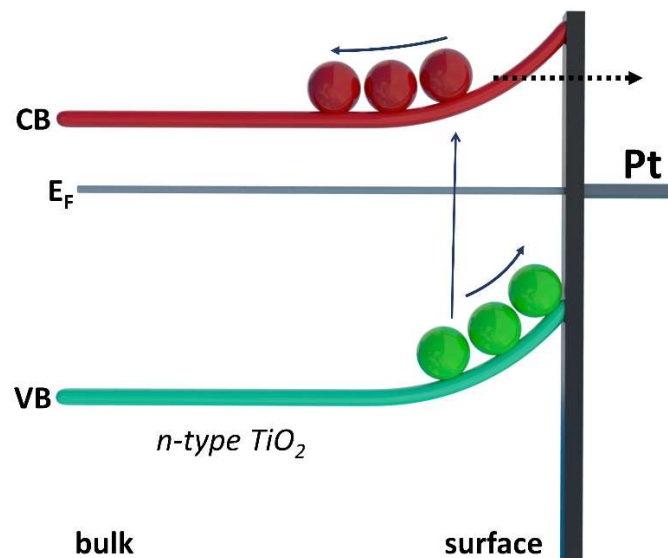


Figure 8. Influence of Pt particle on photogenerated charge carrier dynamics in TiO<sub>2</sub>. The red and green spheres represent CB electron and VB hole, respectively. The straight arrow indicates the direction of CB electron transfer due to the Schottky barrier, and the dotted arrow indicates the actual transfer to the Pt contact. Adapted from<sup>23</sup>

The accumulation of electrons could be mitigated, for instance, if the surface of TiO<sub>2</sub> is brought in contact with noble metals. During the *in-situ* photodeposition of metal particles, the growth of particles onto the TiO<sub>2</sub> surface is driven by the reduction of metal ions with photogenerated

electrons under photocatalytic conditions. A typical example of such a system is the combination of Pt and TiO<sub>2</sub>.

Based on the Schottky barrier model, photogenerated electrons would be expected to be repelled from the interface due to the accumulation of holes in the charge space layer.<sup>15</sup> Nevertheless, this combination is, in fact, catalytically active and often serves as a photocatalyst for H<sub>2</sub> production. It has been shown for Pt/TiO<sub>2</sub> that both trapped electrons and free bulk electrons migrate to the Pt contact and thus to the TiO<sub>2</sub> surface.<sup>107, 108</sup> Moreover, the probability of electron migration from TiO<sub>2</sub> to Pt enhances as the Pt coverage increases.<sup>107</sup> The same conclusion can be applied for the Pt/TiO<sub>2</sub> P25 catalysts, that is that Pt facilitates electron transfer from P25 allowing subsequent reduction reaction of protons to occur.<sup>85</sup> However, the electron migration never reaches unity, since residual Ti<sup>3+</sup> ions can be detected in Pt/TiO<sub>2</sub>.<sup>109</sup> Nevertheless, the deviation from Schottky-type electrical contact in the Pt/TiO<sub>2</sub> catalyst may occur due to the small contact area at the co-catalyst/semiconductor interface that cannot effectively generate electric field.<sup>15</sup>

## 1.4 Hydrogen production by heterogeneous photocatalysis on TiO<sub>2</sub>

The utilization of sunlight to produce hydrogen via photocatalysis holds a great promise for scale-up of renewable energy. Since the first report on hydrogen production from water with TiO<sub>2</sub>-based photoelectrochemical cell, the concept of hydrogen production was quickly extended to particulate photocatalysis as well as hydrogen production from water/alcohol mixtures.<sup>29, 110, 111</sup> Many semiconductor materials were reported to produce hydrogen, including metal oxides and chalcogenides.<sup>112-114</sup> Though numerous chalcogenide systems have been reported to be photocatalytically active, often they suffer from a lack of stability which ruins their catalytic performance over time.<sup>115, 116</sup> For instance, CdS is showing H<sub>2</sub> production from methanol and water just at high pH owing to the higher stability of CdS to photocorrosion in alkaline environment.<sup>117</sup> In non-oxide semiconductors, anions such as sulfide (S<sup>2-</sup>) are thermodynamically unstable in aqueous solution and will be oxidized by holes under illumination to neutral or positive valence states, S or SO<sub>4</sub><sup>2-</sup>, respectively.<sup>118</sup> Considering this, inorganic electron donors like sulfides or sulfites (SO<sub>3</sub><sup>2-</sup>), very efficient hole scavengers, are a good choice for H<sub>2</sub> production on chalcogenides.<sup>118</sup> However, to produce H<sub>2</sub> in the resource wise manner, it would be more meaningful to use particulate photocatalysts that have a high stability in aqueous environment e.g., TiO<sub>2</sub>. Hence, the photocatalytic H<sub>2</sub> production from water and water/alcohol mixture on TiO<sub>2</sub> catalysts will be discussed next.

### 1.4.1 The photocatalytic H<sub>2</sub> production from water

The photocatalytic H<sub>2</sub> production from water, known as overall water splitting (OWS), cleaves water over a photocatalyst into H<sub>2</sub> and O<sub>2</sub> in the ratio 2:1 (fig. 9). The OWS is an uphill process with an associated increase in Gibbs free energy of  $\Delta G^0 = 237 \text{ kJmol}^{-1}$  (eq. 1.12).<sup>119</sup> During reaction, the photoexcited electrons and holes diffuse to the surface of the particle and participate in half-reactions, hydrogen evolution reaction (HER) and oxygen evolution reaction (OER) as given by equations 1.13 and eq. 1.14:

Water splitting:



Hydrogen evolution reaction:



Oxygen evolution reaction:



Considering thermodynamics, the CBM of the photocatalyst must be at more negative potential than the H<sup>+</sup>/H<sub>2</sub> potential (0-(0.059·pH)), V versus NHE), whereas the VMB must be more positive than the O<sub>2</sub>/H<sub>2</sub>O potential (1.23-(0.059·pH)), V versus NHE).<sup>13</sup> accounting for this, the energy input required for this reaction equals the photon energy of 1.23 eV in the case of one-step photoexcitation. However, in the practice a photon energy of at least 2 eV is necessary in order to account, in addition to the thermodynamic water splitting potential, for overpotential and ohmic drop losses.<sup>120</sup> Generally, oxides with two specific electronic structures are active in water splitting: transition metal cations with d<sup>0</sup> electronic configuration (Ti<sup>4+</sup>, Ta<sup>5+</sup>, W<sup>6+</sup>), and metal cations with d<sup>10</sup> configurations (Ga<sup>3+</sup>, Sn<sup>4+</sup>, Sb<sup>5+</sup>). Beside semiconductors, indispensable components of water-splitting photocatalytic systems are co-catalysts, whose main function is to catalyze the HER and OER by decreasing the overpotentials.<sup>119</sup> Commonly used co-catalysts that promote HER are Pt, Rh, Ru, Ir and Ni, whereas oxides of Co, Fe, Ni, Mn, Ru and Ir accelerate the OER.<sup>15</sup> Since 1972 and pioneering work on PEC water splitting on TiO<sub>2</sub> electrodes, TiO<sub>2</sub> and various titanates were studied in the water splitting process.<sup>26, 31, 110, 113, 121, 122</sup> For example, water vapor can be split into H<sub>2</sub> and O<sub>2</sub> when a thin layer of NaOH is applied to a Pt/TiO<sub>2</sub> catalyst.<sup>121</sup> Furthermore, OWS is achieved even with a two-step system that combines anatase and rutile TiO<sub>2</sub> phases, as the hydrogen evolution photocatalyst (HEP) and oxygen evolution photocatalyst (OEP), respectively, and IO<sub>3</sub><sup>-</sup>/I<sup>-</sup> redox couple as an aqueous shuttle.<sup>123</sup> As typical case in photocatalysis on TiO<sub>2</sub>, the effect of its polymorphism on OWS has been addressed. Initially, it has been reported that OWS only proceeds over rutile TiO<sub>2</sub>, but not with anatase and brookite. The rutile activity has

been ascribed to the intrinsic nature of the rutile surface in respect to the photoreduction of  $O_2$ .<sup>31</sup> However, the OWS becomes feasible when anatase or brookite polymorphs were treated with ultraviolet irradiation for prolonged time, which introduces numerous trapped states near the valence bands in anatase and brookite, reducing the driving force for water oxidation.<sup>122</sup> Despite the achieved progress, overall, the efficiency of OWS systems based on  $TiO_2$  catalysts remained rather low. To a large extent this is due to the energy demanding nature of OER.<sup>124</sup> Consequently, a substantial amount of resources is spent on making  $O_2$ , the OWS by-product with low market value.<sup>9</sup> Hence, thermodynamically more favorable  $H_2$  production from alcohols and sugars could be an alternative to the  $H_2$  production from water provided that the oxidation potential of such molecules is considerably more negative than the oxidation potential of water.<sup>125</sup>

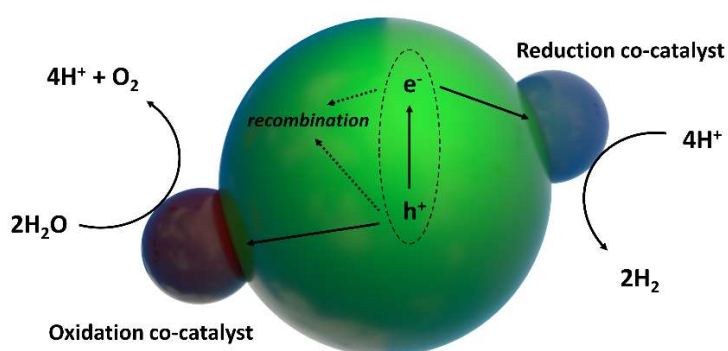


Figure 9. Schematic illustration of the photocatalytic overall water splitting process. Adapted from<sup>26</sup>

#### 1.4.2 Photocatalytic $H_2$ production from water/alcohol mixture

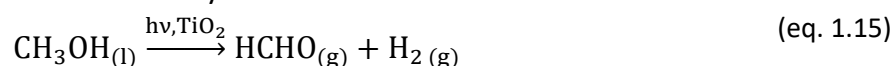
The presence of electron donors in photocatalytic  $H_2$  production from water leads to an increase in the  $H_2$  production rate by overcoming the kinetic limitations of the oxidation process.<sup>126</sup> These electron donors are more easily oxidized than water due to the less demanding oxidation potentials and lower overpotentials due to the intermediates that need to be stabilized.<sup>9</sup> In this way, faster oxidation chemistry removes holes from the semiconductor and thus improves the lifetime of the photogenerated electrons resulting in the higher  $H_2$  production rates.

Various organic compounds such as alcohols, organic acids or amines can be used as electron donors in photocatalytic  $H_2$  production. In the case of  $TiO_2$ , however, due to its high stability against (photo)corrosion, alcohols like methanol, ethanol, 2-propanol and glycerol have been utilized, with methanol being used most frequently. This can be ascribed to the fact that short chain alcohols have a higher initial performance due to the complete oxidation that requires a smaller number of reaction intermediates.<sup>127</sup> The commonly used HER co-catalyst with  $TiO_2$  is platinum owing to its optimal binding energy to H, which leads to a remarkably low

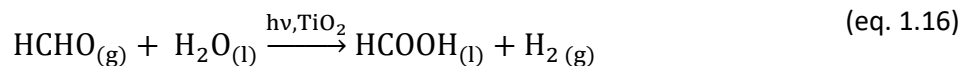
overpotential.<sup>128</sup> Table 1 summarizes the state of the art in H<sub>2</sub> production on self-doped TiO<sub>2</sub> and rutile TiO<sub>2</sub> considering the relevant factors e.g., type of incident light, water/ methanol ratio and amount of used co-catalyst.

During H<sub>2</sub> production on a Pt/TiO<sub>2</sub> catalyst methanol is oxidized by holes from TiO<sub>2</sub> and protons get reduced to H<sub>2</sub> by electrons on Pt. Methanol is initially oxidized to formaldehyde, and can be further decomposed to CO<sub>2</sub> depending on the reaction conditions and reaction time.<sup>129</sup> The overall methanol decomposition is given by equations 1.15-1.18.<sup>111, 130</sup> During methanol oxidation by VB holes, hydroxymethyl radicals are formed, which can subsequently inject excess electrons into the conduction band of TiO<sub>2</sub> in a process known as "current doubling".<sup>23, 131</sup> The current doubling considers that, beside photogenerated electrons, there will be extra electrons in the catalyst which can facilitate the reduction of protons. However, it has been shown that the amount of the electron current never doubles comparing to the hole current, where the extent of photocurrent doubling depends on factors such as crystal doping, methanol concentration or light intensity.<sup>131, 132</sup> For instance, low doping level of TiO<sub>2</sub> and the solvent acidity lowers the photocurrent doubling effect.<sup>131</sup>

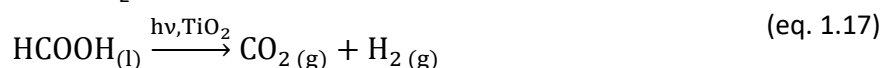
Methanol oxidation to formaldehyde:



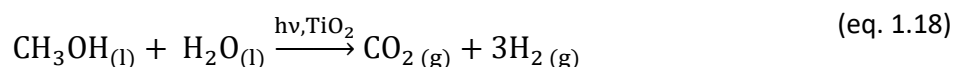
Formaldehyde oxidation to formic acid:



Formic acid oxidation to CO<sub>2</sub>:



Overall reaction:



H<sub>2</sub> production only occurs in the absence of molecular oxygen. When O<sub>2</sub> is present, hydroxymethyl radicals and the photogenerated CB electrons react with dissolved oxygen molecules according to equations 1.19 and 1.20, where the former one allows formation of formaldehyde as the dominant stable product in a quantitative reaction.<sup>130</sup>

Reaction of hydroxymethyl radical with molecular oxygen:

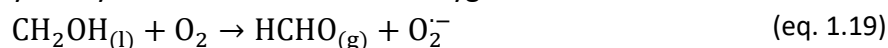
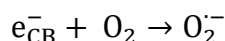


Table 1. Summary of photocatalytic H<sub>2</sub> production on self-doped TiO<sub>2</sub>

Photocatalyst	Reduction reagent	Incident light	Reaction solution	Co-catalyst	H <sub>2</sub> production rate	Ref.
Li-EDA treated P25	Li/EDA solution	AM 1.5 (100 mW/cm <sup>2</sup> )	1:1 methanol/H <sub>2</sub> O	0.5 wt% Pt	13.89 mmolg <sup>-1</sup> h <sup>-1</sup>	85
P25				w/o Pt	3.46 mmolg <sup>-1</sup> h <sup>-1</sup>	
				0.5 wt% Pt	2.05 mmolg <sup>-1</sup> h <sup>-1</sup>	
				w/o Pt	0.023 mmolg <sup>-1</sup> h <sup>-1</sup>	
Self-doped blue TiO <sub>2</sub>	NaBH <sub>4</sub>	AM 1.5G	1:4 methanol/H <sub>2</sub> O	w/o co-cat.	0.149 mmolg <sup>-1</sup> h <sup>-1</sup>	84
Ti <sup>3+</sup> -doped TiO <sub>2</sub>	2-ethylimidazole	>400 nm	1:3 methanol/H <sub>2</sub> O	1 wt% Pt	0.05 mmolg <sup>-1</sup> h <sup>-1</sup>	79
Hydrogenated blue TiO <sub>2</sub>	TiH <sub>2</sub>	300 W Xe	1:4 methanol/H <sub>2</sub> O	0.5 wt% Pt	5.8 mmolg <sup>-1</sup> h <sup>-1</sup>	90
P25					3 mmolg <sup>-1</sup> h <sup>-1</sup>	
Colored TiO <sub>2</sub>	NaBH <sub>4</sub>	300 W Xe	1:3 methanol/H <sub>2</sub> O	1 wt% Pt	6.5 mmolg <sup>-1</sup> h <sup>-1</sup>	81
P25		>400 nm			0.18 mmolg <sup>-1</sup> h <sup>-1</sup>	
		300 W Xe			0.9 mmolg <sup>-1</sup> h <sup>-1</sup>	
Hydrogenated blue TiO <sub>2</sub>	Li/EDA solution	AM 1.5	1:4 methanol/H <sub>2</sub> O	0.5 wt% Pt	3.8 mmolg <sup>-1</sup> h <sup>-1</sup>	86
P25					2.5 mmolg <sup>-1</sup> h <sup>-1</sup>	
Sub-10 nm rutile TiO <sub>2</sub> nanoparticles		AM 1.5 (100 mW/cm <sup>2</sup> )	1:9 methanol/H <sub>2</sub> O	1 wt% Pt	1.954 mmolg <sup>-1</sup> h <sup>-1</sup>	133
P25					0.565 mmolg <sup>-1</sup> h <sup>-1</sup>	
Rutile TiO <sub>2</sub>		UV/VIS	1:4 methanol/H <sub>2</sub> O	0.3 wt% Pt	0.216 mmolg <sup>-1</sup> h <sup>-1</sup>	129]
Cl-doped rutile nanosheets		AM 1.5 (100 mW/cm <sup>2</sup> )	1:1 methanol/H <sub>2</sub> O	0.5 wt% Pt	7.6 mmolg <sup>-1</sup> h <sup>-1</sup>	112
P25					3.8 mmolg <sup>-1</sup> h <sup>-1</sup>	

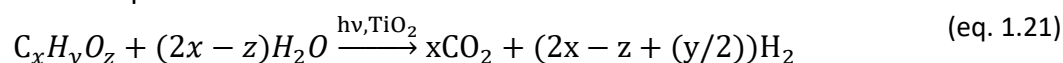


Reaction of a conduction band electron with molecular oxygen: (eq. 1.20)



As already mentioned, alcohols such as methanol, ethanol or glycerol can serve as donor molecules in H<sub>2</sub> production. Upon reaction, the stoichiometric amount of H<sub>2</sub> and CO<sub>2</sub> is produced according to equation 1.21.<sup>127 134</sup>

Overall decomposition of donor molecules:



However, when tert-butyl alcohol is used as donor in H<sub>2</sub> production, no H<sub>2</sub> can be evolved in the reaction, thus indicating that solely alcohols with a hydrogen atom in the  $\alpha$ -position can lead to H<sub>2</sub> production.<sup>117</sup>

H<sub>2</sub> production from water/methanol mixture ( $\Delta G_0 = 16.1 \text{ kJmol}^{-1}$ ) results, generally, in a lower amount of energy that can be stored in comparison with H<sub>2</sub> production from water ( $\Delta G_0 = 237 \text{ kJmol}^{-1}$ ).<sup>130, 135</sup> However, if overall decomposition is considered as sum of three reactions (eq. 1.15-1.17), then the first two reactions, methanol oxidation to formaldehyde and formaldehyde oxidation to formic acid, have a positive change of free Gibbs energy, while the formic acid oxidation to CO<sub>2</sub> has a large negative change of Gibbs energy.<sup>130</sup> Although it represents an intrinsic barrier for the undesired reactions of produced H<sub>2</sub>, in the same time it lowers the solar energy conversion that can be achieved by decomposition of alcohols. Having said that limiting the formic acid oxidation in the methanol decomposition would be the way to achieve the optimal ratio in terms of amount of H<sub>2</sub> that is produced and solar energy that is converted in the reaction. In prospective, the approach of selective oxidation of donor molecules would be meaningful in H<sub>2</sub> production and biomass valorization through the production of oxidation products from renewables with high added value other than CO<sub>2</sub>.<sup>9, 129</sup>

## 1.5 Aims and outline of the thesis

A huge photocatalytic potential of TiO<sub>2</sub>, particularly due to the high UV activity and stability against (photo)corrosion in wide range of operation conditions, makes it one of the most studied semiconductor photocatalysts. In practice, however, transition from UV to solar illumination is associated with substantial decrease in photocatalytic activity. For this reason, design and construction of efficient solar TiO<sub>2</sub> catalysts is still primary goal of work in the field. Intrinsically, photocatalytic activity of TiO<sub>2</sub> can be modulated by either doping or nanostructuring. While doping mainly strives to enhance solar light harvesting of TiO<sub>2</sub>, nanostructuring deals with improvement of charge carrier dynamics by shortening bulk charge carrier diffusion path in TiO<sub>2</sub>. Therefore, the aim of this thesis is to design highly efficient TiO<sub>2</sub>

catalysts for solar H<sub>2</sub> production following doping and nanostructuring principles. It also aims to correlate the structure with photocatalytic activity and provide guideline for design of next generation TiO<sub>2</sub> catalysts for solar application. The effect of TiO<sub>2</sub> doping on solar light harvesting and photocatalytic H<sub>2</sub> production is studied with self-doped TiO<sub>2</sub>. At the beginning, the synthesis of the material is introduced and co-doping of structure with the elements present in the reaction medium is addressed by studying surface and bulk composition. Further, a spatial distribution of Ti<sup>3+</sup> ions within TiO<sub>2</sub> framework is scrutinized followed by assessing the impact of Ti<sup>3+</sup> ions on solar light harvesting in self-doped TiO<sub>2</sub>. Here, it is also shown how light absorption can be modulated in self-doped samples. To conclude the in-depth characterization of the material, a structural model of self-doped TiO<sub>2</sub> is proposed. Finally, the solar H<sub>2</sub> production is tested and influence of Ti<sup>3+</sup> ions on photocatalytic activity under solar light in self-doped TiO<sub>2</sub> are discussed. In the next chapter impact of nanostructuring on TiO<sub>2</sub> is investigated on rutile structures. After the synthesis of rutile needles is introduced, morphology and structure of rutile samples is analyzed. Since rutile TiO<sub>2</sub> in general shows structural anisotropy, the needle structures are studied in two crystallographic directions, in crystal ab plane and along c-axis. Further, optical absorption as well as analysis of surface states is performed to check for defects and chemical impurities in rutile needles. The solar H<sub>2</sub> production of rutile needles is benchmarked with nanoparticulate rutile TiO<sub>2</sub> and TiO<sub>2</sub> P25. Real potential of best performing rutile catalyst in solar H<sub>2</sub> production is confirmed in H<sub>2</sub> production test under direct sun illumination. Lastly, the structure-activity relationship is established, and key structural feature of rutile catalyst is identified.

## 2. Experimental

### 2.1 Catalyst synthesis

#### 2.1.1 Synthesis of blue titania in reaction with Na/K alloy (B-TiO<sub>2</sub>)

**Attention: All synthetic steps involving Na/K alloy should be carried out with extreme caution under strict exclusion of air or moisture while appropriate personal protection (hood, blast shields, face shield, protective and fire-resistant clothing) should be used and worn all the time.**

B-TiO<sub>2</sub> was synthesized in reaction with liquid Na/K alloy originally proposed for functionalization of carbon nanotubes.<sup>136</sup> In a typical synthesis, TiO<sub>2</sub> (1.00 g, TiO<sub>2</sub> nanopowder, Sigma-Aldrich) was added to an oven-dried 250 mL flat-bottom flask containing a glass-coated magnetic stirring bar. The flask was placed in a drying oven heated at 110 °C for 4 h. Then, the flask was sealed with a rubber septum and transferred to an Ar glovebox (O<sub>2</sub> and H<sub>2</sub>O concentrations < 0.1 ppm) where anhydrous 1,2-dimethoxyethane (DME, 100 mL) and Na/K alloy were added with syringe. Once the reagents were added, the flask was removed from the glovebox and ultrasonicated for 15 min to yield a blue suspension, which was afterwards vigorously stirred at room temperature. The amount of added Na/K alloy and reaction times are summarized in Table 2.

Table 2. Experimental details on amount of added Na/K alloy and reaction times during the synthesis of blue titania samples

Sample	Amount of added Na/K / mL	Reaction time / days
B_TiO <sub>2</sub>	0.45	70
B_TiO <sub>2</sub> _0.05	0.05	1*
B_TiO <sub>2</sub> _0.25	0.25	5
B_TiO <sub>2</sub> _0.5	0.5	5
B_TiO <sub>2</sub> _1	1	5
B_TiO <sub>2</sub> _2	2	5
B_TiO <sub>2</sub> _4	4	5
Blue rutile TiO <sub>2</sub>	0.45	5

\*Na/K alloy was completely reacted after 15 min of sonication

Methanol (10 mL) was then added to quench any excess of alloy, and the mixture was stirred at room temperature for 10 min. For workup, the reaction mixture was filtered through a 0.1  $\mu\text{m}$  PTFE membrane. The filter cake was washed with 0.2 M HCl (500 mL) and deionized water until the test reaction on  $\text{Cl}^-$  was negative ( $\text{Ag}^+$  test was used to examine the residual  $\text{Cl}^-$ ). The as-purified material was freeze-dried overnight.

### *2.1.2 Synthesis of grey titania by thermal annealing of B-TiO<sub>2</sub> (G-TiO<sub>2</sub>)*

B-TiO<sub>2</sub> (500 mg) was added to a combustion boat and placed inside a tubular furnace. The tube was flushed with 100 mL/min flow of Ar for 1 h and then annealing was performed under Ar flow (100 mL/min) at 400 °C for 1 h. A heating ramp of 5 K/min was applied. After annealing, the powder was cooled down to room temperature inside the furnace under Ar flow and sample was denoted as G-TiO<sub>2</sub>. G-TiO<sub>2</sub> (250 mg) was then washed with 0.2 M HCl (200 mL) and deionized water until negative reaction on  $\text{Cl}^-$ , and as-purified material was freeze-dried overnight and denoted as G-TiO<sub>2</sub>/AC, where AC stands for acid cleaning.

### *2.1.3 Synthesis of rutile needles under ambient conditions*

TiO<sub>2</sub> rutile needle samples were synthesized from aqueous solution by crystallization at ambient conditions.<sup>137</sup> In a typical synthesis of rutile TiO<sub>2</sub> needles, 190 mL deionized water and 8 mL concentrated HNO<sub>3</sub> were mixed. After 30 min of stirring 12.5 mL isopropanol (IPA) were added and the mixture was kept stirring. After further stirring of 30 min, 3.8 mL of titanium-tetraisopropoxide (TTIP) were added and a white solid was obtained. The reaction was sonicated for 10 min and afterwards left at room temperature for 4 days to let rutile TiO<sub>2</sub> needles form. The white solid was recovered from the mixture by centrifugation, washed copiously with water and dried at 120 and 200 °C, where depending on the applied temperature samples were denoted as rTiO<sub>2</sub>-needle<sub>120</sub> and rTiO<sub>2</sub>-needle<sub>200</sub>, respectively.

## **2.2 Photocatalytic H<sub>2</sub> production testing**

In this work, H<sub>2</sub> production tests were performed in a home-built set-up with top-illuminated reactor. In the following, the most important characteristics of the reactor and set-up for H<sub>2</sub> production tests will be discussed.

The body of the top-illuminated reactor is made from stainless steel which includes various connections for different purposes (fig. 10). On the top side of the body is a DN 40 CF connection. The connection allows sealing of the reactor with a lid. The lid is a view port flange containing a flat quartz window straddled by two stainless steel discs. The quartz glass enables

irradiation of the catalyst with high transparency for solar light while the flat glass surface reduces light loss due to light scattering. The glass-metal contacts in the lid are sealed with two elastomeric O-rings from top and bottom side. Beside DN 40 CF connection, there are two Swagelok® Tube Fitting connections on the reactor body. These are used for gas management during catalytic test, as an inlet and an outlet for purging (inert) gas and reaction products. The catalysts are tested in form of a slurry. The catalyst slurry is added in a quartz dish which is then placed in the central cavity of the reactor. The catalyst slurry is agitated by a magnetic stirrer during the H<sub>2</sub> production test. The temperature of the reaction is kept constant by external water circulation. The top-illuminated reactor was operated in flow mode allowing on-line product detection by means of a mass spectrometer (MS).

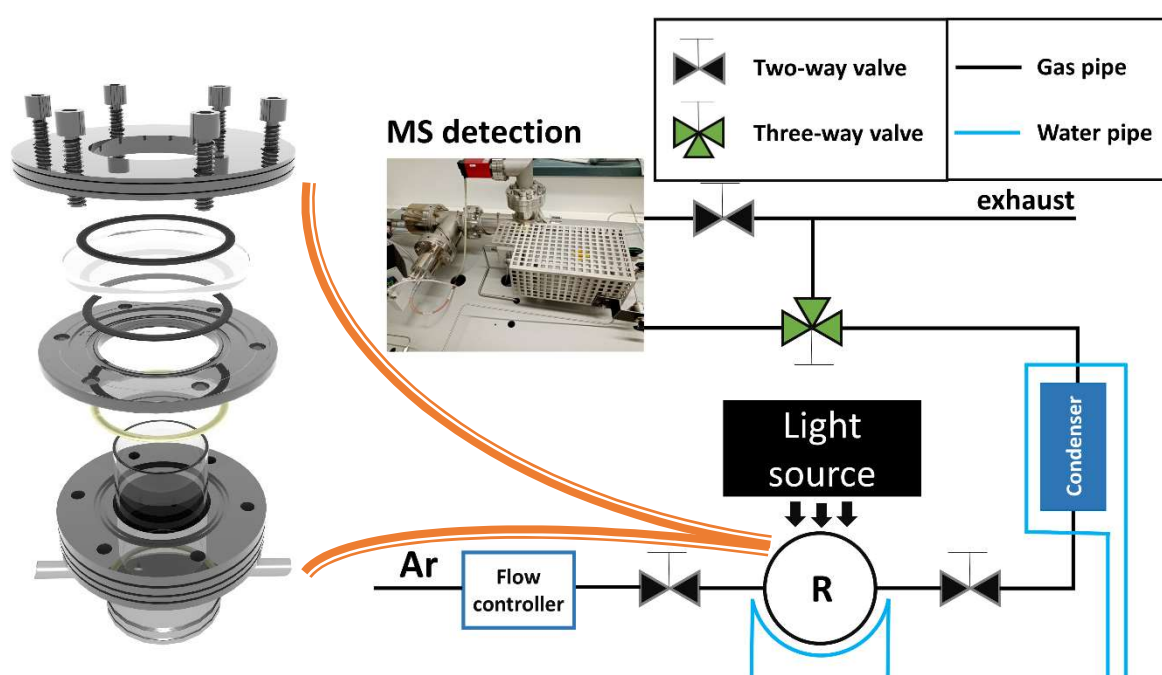


Figure 10. Schematic illustration of the reactor (left) and set-up for H<sub>2</sub> production (right)

Flow mode operation is achieved by over-flow of Ar where the flow rate of the gas is controlled by a flow controller. After passing through the reactor, Ar is enriched with produced H<sub>2</sub> in the reaction as well as gas-phase methanol and water. To reduce the amount of organics and water in the downstream gas, a condenser is installed in the gas line between reactor and MS. The temperature of the condenser is controlled by in-house cooling water circulation. After capturing the volatile organics in the condenser, produced H<sub>2</sub> is quantified by MS as H<sub>2</sub> production rate in mmolg<sup>-1</sup>h<sup>-1</sup> according to equation 2.1:

$$\text{H}_2 \text{ production rate} = \frac{c_{\text{H}_2} \cdot Q_{\text{Ar}} \cdot 60}{m_{\text{cat}} \cdot V_m \cdot 1000} \quad (\text{eq. 2.1})$$

where  $c_{\text{H}_2}$  is the concentration of hydrogen in parts per million (ppm),  $Q_{\text{Ar}}$  is the flow of Ar in  $\text{mLmin}^{-1}$ ,  $m_{\text{cat}}$  is the mass of catalyst in mg, and  $V_{m,25^\circ\text{C}}$  is molar volume of gas derived from ideal gas law:

$$V_m = \frac{n \cdot R \cdot T}{p} \quad (\text{eq. 2.2})$$

in which  $n$  is amount of gas in mol,  $R$  is universal gas constant of  $8.314 \text{ Jmol}^{-1}\text{K}^{-1}$ ,  $T$  is absolute temperature of  $298.15 \text{ K}$ , and  $p$  is pressure of  $101325 \text{ Pa}$ .

Beside produced  $\text{H}_2$ , a formic acid in the liquid phase after catalytic reaction is analyzed by high-performance liquid chromatography (HPLC).

The  $\text{H}_2$  production tests are run under simulated solar light irradiation. In this thesis a  $300 \text{ W}$  xenon (Xe) lamp (Newport) is used as the light source for solar simulation. This light source emits photons in UV, visible and infrared spectral range. The output spectrum was corrected with an AM 1.5 filter (Newport) and the output light intensity was set to  $100 \text{ mWcm}^{-2}$ . The light beam is directed by a reflecting mirror, so that top-illumination geometry of the reactor is achieved. In addition to the AM 1.5 (solar light), one  $\text{H}_2$  production experiment was done by direct sun utilization as a light source (sun light). The experiment was run in total for  $2 \text{ h}$  and light intensity was  $65 \text{ mWcm}^{-2}$ . In the experiment with sun irradiation, the top-illumination reactor could not be used due to technical reasons. First, the reactor does not allow whole volume of the catalyst slurry to be irradiated by light since it casts shadow. Second, the reactor cannot be tilted towards the sun due to the limited volume of the cavity. Therefore, to mitigate the drawbacks of the top-illuminated reactor under sun light irradiation, the reaction here was run in a  $50 \text{ mL}$  cylindrical pyrex glass Schlenk reactor keeping all the other reaction conditions the same. To obtain a defined illuminated surface, the pyrex reactor is tilted which leads to an increase of the illuminated area compared with the top-illuminated reactor. To compare  $\text{H}_2$  production activities under solar and sun light, the  $\text{H}_2$  production rates ( $\text{mmolg}^{-1}\text{h}^{-1}$ ) were normalized in terms of light intensity and illuminated area according to the equation 2.3:

$$\text{Specific } \text{H}_2 \text{ production rate} = \frac{\text{H}_2 \text{ production rate}}{\text{Light intensity} \cdot \text{Illuminated area}} \quad (\text{eq. 2.3})$$

where specific  $\text{H}_2$  production rate is in  $\text{mmolg}^{-1}\text{h}^{-1}\text{mW}^{-1}$ ,  $\text{H}_2$  production rate in  $\text{mmolg}^{-1}\text{h}^{-1}$ , light intensity in  $\text{mWcm}^{-2}$  and illuminated area in  $\text{cm}^2$ .

## Experimental description:

15 mg TiO<sub>2</sub> catalyst was dispersed in 15 mL (1:1 V/V) water-methanol mixture and H<sub>2</sub>PtCl<sub>6</sub> (0.5 wt% Pt) was added by means of a micropipette. Then, the reaction mixture was sonicated for 1 min. After sonication, the quartz dish with the catalyst slurry was transferred to the reactor and the reactor was closed. The slurry was agitated by a magnetic stirrer. The oxygen was removed by purging of Ar at a rate of 10 mLmin<sup>-1</sup> for 3 h unless it was mentioned otherwise. Reaction temperature was kept at 25 °C. After 3 h, the reaction was started by switching on the light source. The solar simulated or direct sun light was used in H<sub>2</sub> production tests. At the beginning of the test, photo deposition of Pt proceeds in parallel with the H<sub>2</sub> production. The illumination time was 2.5 h. Additionally, to test the tolerance of the samples on switching off the light source (day-night), a test with three illumination cycles was applied. In this test two light intervals were interrupted by 30 min dark interval. H<sub>2</sub> production was monitored by on-line MS and photocatalytic activity of TiO<sub>2</sub> catalysts is plotted either as mmolg<sup>-1</sup>h<sup>-1</sup> or mmolg<sup>-1</sup>h<sup>-1</sup>mW<sup>-1</sup>. After photocatalytic test aliquot of catalyst slurry is filtered through 0.1 μm PTFE syringe filter with glass fibers (Captiva, Agilent) and tested for formic acid by HPLC.

Additional to the flow mode photocatalytic tests, few batch mode H<sub>2</sub> production tests under solar light were performed as well. The 50 mL cylindrical pyrex Schlenk reactor was used for batch tests. The catalyst slurry was prepared following the procedure used for flow mode test. Afterwards, the slurry was bubbled with Ar for 30 min to remove oxygen. The slurry was agitated by a magnetic stirrer and the reaction temperature was kept at 25 °C. After 30 min of Ar bubbling, the reactor was closed, and the light source was switched on. The reaction was run for 2.5 h and headspace gas was sampled by a degassed 5 mL gas-tight syringe. The produced H<sub>2</sub> in the reaction was quantified by gas chromatography (GC) and plotted as mmolg<sup>-1</sup> according to equation 2.4:

$$\text{H}_2 \text{ production} = \frac{V_{\text{exp}}}{m_{\text{cat}} \cdot V_{m,25\text{ }^\circ\text{C}}} \quad (\text{eq. 2.4})$$

where  $V_{\text{exp}}$  is experimentally determined volume of H<sub>2</sub> in mL,  $m_{\text{cat}}$  is the mass of catalyst in mg, and  $V_{m,25\text{ }^\circ\text{C}}$  is molar volume of ideal gas at 25 °C. Pressure increase in batch experiments was not accounted for.

## 2.3 Catalyst characterization

### 2.3.1 X-ray diffraction (XRD)

The crystal structure of semiconductor photocatalysts can strongly influence the photocatalytic activity, therefore XRD is an important characterization technique for

crystalline semiconductor catalysts. X-ray diffraction is based on the interaction of lattice atoms with a monochromatic beam of incident X-rays that causes their constructive and destructive interference (fig. 11). Diffraction signals are obtained only in case when constructive interferences occur. The condition for constructive interference is given by Bragg's law (eq. 2.5)<sup>138</sup>. This law relates the wavelength of electromagnetic radiation to the diffraction angle and the interplanar spacing in the crystalline sample:

$$n\lambda = 2d\sin\theta \quad (\text{eq. 2.5})$$

in which,  $n$  is the order of a reflection,  $\lambda$  is the wavelength of applied X-rays,  $d$  is the distance between parallel crystal planes and  $\theta$  is the angle between the incident beam and a crystal plane, known as Bragg angle. The Bragg law is important in indexing X-ray diffraction patterns as well as for  $d$ -spacing calculation.

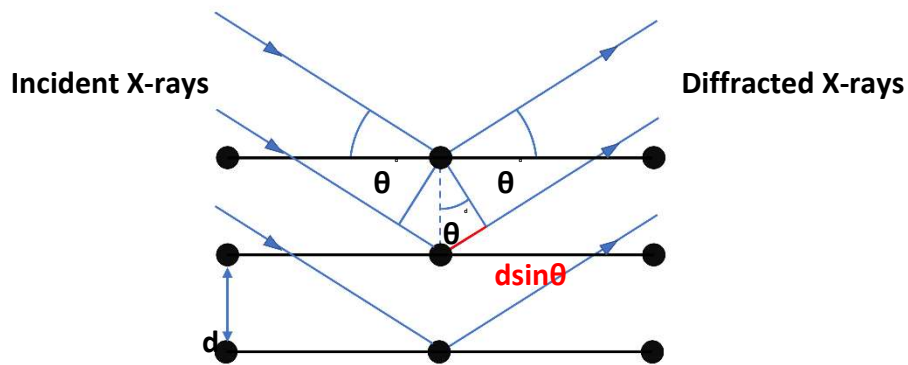


Figure 11. Diffraction of X-rays by a crystal.

Apart from that, XRD data is used to determine mean crystallite size in crystalline samples. The mean crystallite size ( $D$ ) can be estimated from diffraction peak broadening according to the Scherrer's formula (eq. 2.6):<sup>139</sup>

$$D = \frac{K\lambda}{\beta\cos\theta} \quad (\text{eq. 2.6})$$

where  $K$  is the dimensionless shape factor with a value of 0.9,  $\lambda$  is the wavelength of X-rays,  $\beta$  is the full width at half maximum (FWHM) and  $\theta$  is the diffraction (Bragg) angle.



### Experimental description:

XRD powder patterns were recorded on a Panalytical X'Pert diffractometer equipped with a Xcelerator detector using automatic divergence slits and Cu K $\alpha$ 1/ $\alpha$ 2 radiation (40 kV, 40 mA;  $\lambda$ = 0.15406 nm, 0.154443 nm). Cu beta-radiation was excluded using a nickel filter foil. The collected data were converted from automatic divergence slits to fixed divergence slits (0.25°) before data analysis to obtain the correct intensities. Peak positions and profile were fitted with Pseudo-Voigt function. Phase identification was done by using the PDF-2 database of the International Center of Diffraction Data (ICDD).

### 2.3.2 Transmission electron microscopy (TEM)

TEM utilizes high energy electrons for signal generation. Electrons are one type of ionizing radiation, the radiation capable of removing inner-shell electrons from the attractive field of the nucleus by energy transfer. Advantage of using ionizing radiation is that it produces a wide range of secondary signals from specimen which can be used in imaging and analytical electron microscopy providing useful information about structure, morphology, and elemental composition of the specimen. Some of the secondary signals generated in TEM are summarized in fig. 12.<sup>140</sup>

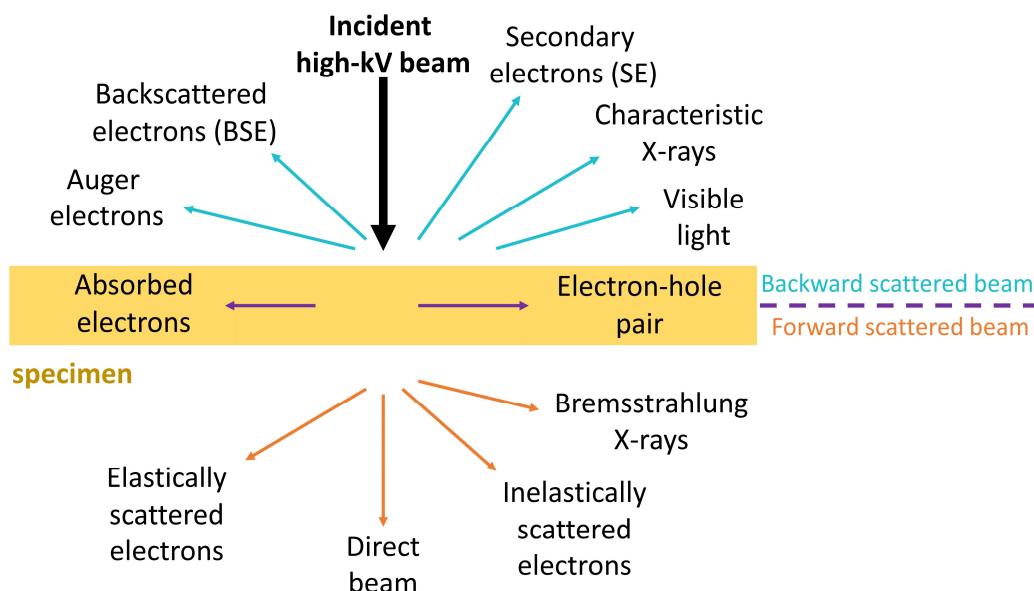


Figure 12. Signals generated when a high-energy beam of electrons interacts with a thin specimen. Adapted from<sup>140</sup>

A bright field (BF) detector creates two-dimensional images by projecting direct beam electrons that either passed unscattered or were scattered to very low angles onto a screen. The BF image without specimen is bright. Thus, dark pixels in the BF image are spots where strong scattering occur due to the presence of the material since less electrons are reaching the detector.

In scanning transmission electron microscopy (STEM), unlikely in static-beam TEM, the imaging signal is generated by scanning the electron beam on the specimen and forward beam scattered electrons are detected by an electron detector (scintillation or semiconductor). The working principle of STEM is the same as used in other scanning-beam instruments such as a scanning electron microscope (SEM) or scanning-tunneling microscope (STM). As the probe is scanned, scattered electrons form a dark field image, bright signal on a dark background. The annular dark field (ADF) detector is used to collect electrons that were scattered by the specimen. The configuration allows maximization of the Rutherford-scattering effect while diffraction contrast effects are smoothed out, which is favorable for electron energy-loss spectroscopy (EELS). The most common ADF detector is called the high angle annular darkfield detector (HAADF) allowing atomic resolution high Z-contrast imaging of the specimen.

Electron energy-loss spectroscopy (EELS) is the analysis of the energy distribution of electrons coming through the specimen that suffered inelastic (electron-electron) collisions. The energy-loss events can tell about chemical and electronic structure of the specimen. Comparing with energy dispersive X-ray spectroscopy (XEDS) for determination of chemical composition, EELS generally offers better spatial resolution and analytical sensitivity as well as detection of light elements, which are difficult to analyze with XEDS. Moreover, due to the difference in electronic structure, EELS is capable to distinguish between different crystal phases of material. For example, it can distinguish between the anatase and rutile crystal phase in  $\text{TiO}_2$ .

#### **Experimental description:**

The TEM measurements were performed either at 80 or 200 kV with a TEM Zeiss EM902 or probe aberration-corrected JEM-ARM200F (JEOL, Corrector: CEOS), respectively. The JEM-ARM200F microscope is equipped with an Enfinium ER (Gatan, USA) electron energy loss spectrometer (EELS) for chemical analysis. STEM imaging was performed using High-Angle Annular Dark Field (HAADF) while the annular dark field (ADF) detector was used during EELS acquisition. The sample was deposited on a Cu-grid (mesh 300) with a holey carbon film without pre-treatment and transferred to the microscope.

#### *2.3.3 Diffuse reflectance UV-Vis-NIR spectroscopy (DRS)*

Interaction of incident light photon with matter can lead to interplay of different optical phenomena e.g., reflection, refraction, transmission, and absorption, which extent is

dependent of the materials' properties. The flat material surface, for example, favors specular, mirror-like reflection, to occur. Here, the angle of incident and specular light is equal (fig. 13, left). In contrast, in the case of rough surfaces as well as when photons penetrate deeper into solid, light starts to reflect in various direction leading to diffuse reflection. (fig. 13, right). A use of an integrating sphere is indispensable whenever fluctuations of the light beam received by the detector occur due to e.g. diffuse reflection. The integrating sphere is a spherical cavity whose inner wall is coated with a highly reflective material such as barium sulfate where light undergoes multiple reflections until the reflected light enters the detector. The information about the sample from DRS is available only in the case when diffuse reflection interferes with light absorption of the material. Therefore, DRS measures scattering of the light in the UV-Vis-NIR spectral range on the semiconductor, which varies with wavelength to give the reflectance spectrum that is recorded.

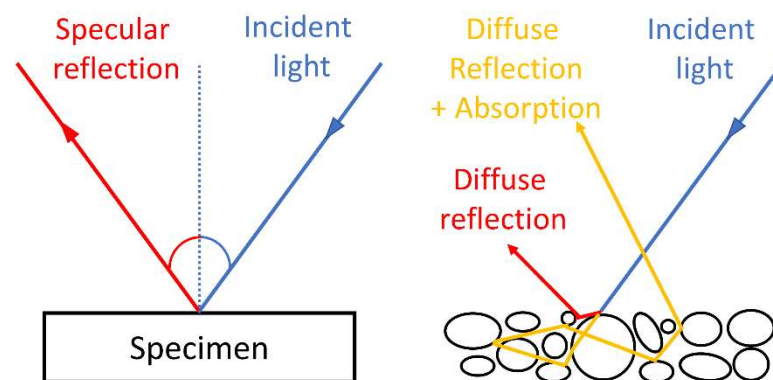


Figure 13. Specular and diffuse reflection of incident light photon

Optical absorption of the  $\text{TiO}_2$  can be estimated from DRS data by applying a Kubelka-Munk function:

$$F(R_\infty) = \frac{K}{S} = \frac{(1 - R_\infty)^2}{2R_\infty} \quad (\text{eq. 2.7})$$

where  $R_\infty$  is the reflectance of an infinitely thick specimen, while K and S are an absorption and scattering coefficients, respectively.<sup>141</sup> Alternatively, apparent absorption can be derived from DRS data by applying a following equation:

$$\text{Apparent absorption} = \log(1/R) \quad (\text{eq. 2.8})$$

where R is diffuse reflectance.

In this thesis eq 2.8 is used over eq. 2.7 for the estimation of the absorption of TiO<sub>2</sub> samples from reflectance data due to two reasons (fig. 14). First, later formula gives a stronger signal in Vis and NIR spectral region than that is obtained using the former one; second, it allows more convenient comparison of the results since this method prevails in literature reporting optical absorption of colored TiO<sub>2</sub> materials. Sometimes this fact is not so apparent, but commercially available softwares (e.g. Perkin Elmer) employs eq. 2.8 for conversion of reflectance data into absorbance. In case of rutile samples, eq. 2.8 become useful as an indicator of the absence of Vis absorption since it is more sensitive in the Vis spectral region.

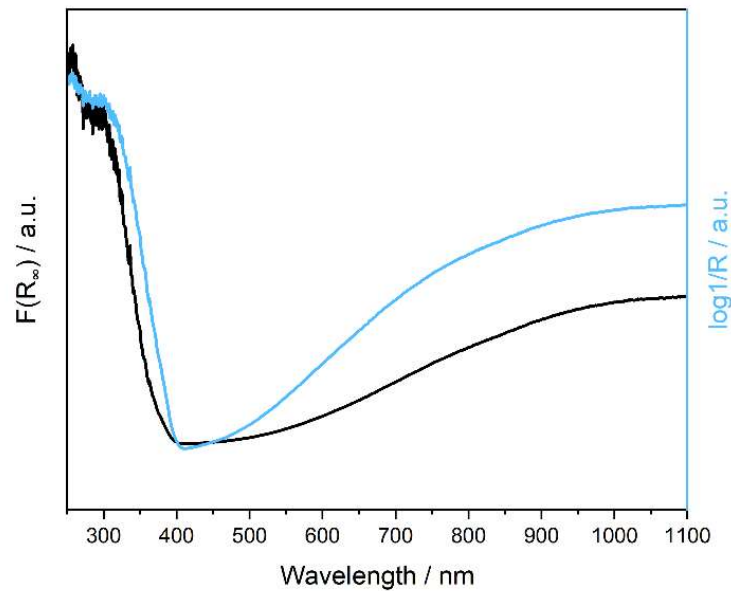


Figure 14. Comparison of Vis-NIR absorption of B-TiO<sub>2</sub> derived from reflectance data using  $F(R_{\infty})$  and  $\log 1/R$  formula

The onset of absorption edge (band gap) is determined by Tauc method based on the assumption that the energy-dependent absorption coefficient  $\alpha$  can be expressed as follows:

$$(\alpha \cdot hv)^{1/\gamma} = B(hv - E_g) \quad (\text{eq. 2.9})$$

where  $h$  is the Planck constant,  $\nu$  is the photon's frequency,  $\gamma$  is the factor that describes electron transition,  $E_g$  is the band gap energy, and  $B$  is a constant. Putting  $F(R_\infty)$  (eq. 2.8) instead of  $\alpha$  allows band gap calculation from diffuse reflectance data (eq. 2.10)

$$(F(R_\infty) \cdot h\nu)^{1/\gamma} = B(h\nu - E_g) \quad (\text{eq. 2.10})$$

### Experimental description:

Diffuse reflectance UV–Vis–NIR spectra of TiO<sub>2</sub> samples were measured on a Perkin Elmer Lambda 365 spectrophotometer equipped with the integrating sphere. The spectra were recorded in the range between 250 – 1100 nm with 0.5 nm resolution in a powder cell. Barium sulphate powder was used as reference material for background measurement.

### 2.3.4 X-ray photoelectron (XP) spectroscopy

X-ray photoelectron spectroscopy is a surface-sensitive spectroscopic technique that measures the elemental composition as well as the chemical state of the elements at the surface of a solid catalyst. It is based on the principle of the photoelectric effect. XP spectra are obtained by irradiating a material with a beam of aluminum or magnesium K $\alpha$  X-rays while simultaneously measuring the kinetic energy (KE) of electrons that escape from the depth of up to 10 nm (fig. 15)<sup>142</sup>.

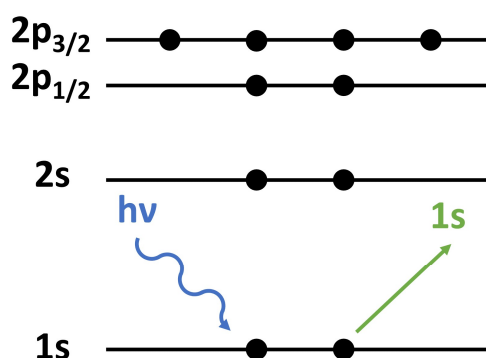


Figure 15. Schematic diagram of photoelectron emission from x-ray bombardment of a material surface

The electrons ejected from the sample are collected by a hemispherical electron energy analyzer which measures the kinetic energy of the ejected electrons. The kinetic energy of electrons can then be used to determine the binding energy (BE) of the respective electron from equation 2.11<sup>143</sup>

$$BE = h\nu - KE - \phi_s \quad (\text{eq. 2.11})$$

in which  $h$  is the Planck's constant,  $\nu$  is the frequency of incident X-ray and  $\phi_s$  is the work function of the spectrometer. Each ejected electron from an element has a characteristic binding energy and the value of this binding energy is used to identify the element and core level of the electron by comparison with values from binding energy databases.

The peak positions can also be used to determine oxidation states of the element. In general, the binding energy increases by increasing oxidation state, where the peak position is typically shifting between 0-3 eV.

#### **Experimental description:**

The X-ray photoelectron measurements were performed on an ESCALAB 220iXL (ThermoFisher Scientific, Waltham, MA, USA) with monochromatic Al K $\alpha$  radiation ( $E = 1486.6$  eV). Samples are prepared on a stainless-steel holder with conductive double-sided adhesive carbon tape. The electron binding energies were obtained with charge compensation using a flood electron source and referenced to the C 1s peak of C-C and C-H bonds at 284.8 eV.

#### *2.3.5 Electron paramagnetic resonance (EPR)*

Electron paramagnetic resonance is a method of choice to study paramagnetic electrons in organic and inorganic samples. An electron has a spin quantum number,  $s = \frac{1}{2}$ , which has magnetic components  $m_s = \frac{1}{2}$  and  $m_s = -\frac{1}{2}$ . In the absence of a magnetic field, the energy of the two  $m_s$  states equals. However, a strong external magnetic field generates a difference between the energy levels of the electron spins states,  $m_s = +\frac{1}{2}$  and  $m_s = -\frac{1}{2}$ , which results in resonance absorption of an applied microwave energy (fig. 16). The energy difference between the two states is dependent on the strength of the magnetic field (eq. 2.12). This is called the Zeeman effect.

$$\Delta E = h\nu = g_e \mu_B B_0 \quad (\text{eq. 2.12})$$

where  $\Delta E$  is the energy difference between the spin levels,  $g_e$  is the g-factor (for free electrons = 2.0023),  $\mu_B$  is the Bohr magneton ( $9.274 \cdot 10^{-24} \text{ JT}^{-1}$ ),  $B_0$  is the strength of the external magnetic field (gauss or Tesla),  $h$  is the Planck's constant ( $6.626 \cdot 10^{-34} \text{ Js}$ ),  $\nu$  is the microwave frequency (GHz or MHz). From the relationship, there are two important factors to note. The first one is that two spin states have the same energy when there is no applied magnetic field and the second one is that the energy difference between the two spin states increases linearly with increasing magnetic field strength. EPR spectrometers generally can vary either

the strength of the external magnetic field or the frequency of the microwave radiation. Usually, however, most of the spectrometers work in the way that magnetic field is changing while holding the frequency constant. Due to technical reasons, controlling the external magnetic field is more convenient. EPR spectra can be recorded in different frequency regions, the most important ones are L-band (1-2 GHz), S-band (2-4 GHz), X-band (8-10 GHz), Q-band (~35 GHz) and W-band (~90 GHz).

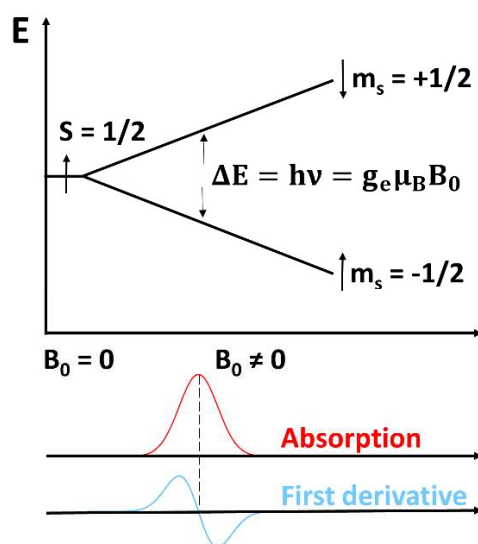


Figure 16. Electron Zeeman interaction for a spin  $S = 1/2$  system in the presence of an external magnetic field

In this work, a continuous wave (CW) X-band frequency EPR spectrometer was used. During CW acquisition of the spectra the applied microwave frequency is held constant. In this case, the magnetic field is varied until the resonance condition is fulfilled and the microwave energy matches the energy difference for the allowed spin transitions. The spectra were recorded in the dark which allows studying paramagnetic centers for instance that have been formed upon self-doping of titania.

#### Experimental description:

The EPR measurements in X-band (microwave frequency  $\approx 9.8$  GHz) were performed at 96 and 296 K by an EMX CW-micro spectrometer (Bruker Biospin GmbH, Rheinstetten, Germany). The samples were measured under the same conditions (microwave power: 6.9 mW, attenuation: 15 dB, receiver gain:  $1 \times 10^4$ , modulation frequency: 100 kHz, modulation amplitude: 5 G).  $g$  values have been calculated from the resonance field  $B_0$  and the resonance frequency  $\nu$  using the resonance condition  $h\nu = g\beta B_0$ . The calibration of the  $g$  values was performed using DPPH (2,2-diphenyl-1-picrylhydrazyl,  $g = 2.0036 \pm 0.00004$ ).

### 2.3.6 Atomic absorption spectroscopy (AAS)

Atomic absorption spectroscopy is a technique used to determine the content of metals in the specimen. It relies on the phenomenon that atoms can absorb light at a characteristic wavelength once heat energy from a flame has converted the sample into free ground state atoms (fig. 17). When light of this wavelength is provided, the light is absorbed by the atom while electrons move from the ground state to the excited state. Depending on the photon energy, electron transitions to higher excited states are possible as well. For AAS analysis, however, the wavelength of the ground state to the first excited level is typically of most interest because this transition is the most intense.

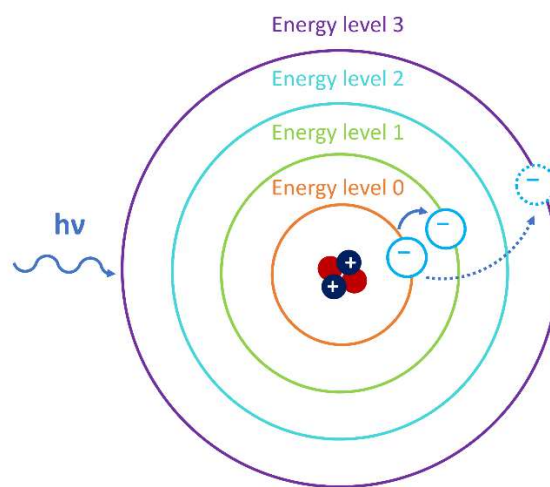


Figure 17. Excitation of an atom by a photon

The signal in AAS is generated as the difference between the amount of light emitted from the lamp and light that reaches the detector. The Beer Lambert law describes the relationship between light absorption and concentration of the metal. According to the law, the amount of light absorbed is proportional to the number of atoms excited from the ground state in the flame (eq. 2.13)<sup>144</sup>

$$A = abc \quad (\text{eq. 2.13})$$

where A is the absorbance, a is the constant for a given system, b is the length of the cell and c is the concentration of the analyte atoms in the flame.

This expression predicts a linear relationship between absorbance and concentration as long as a and b remain constant.



**Experimental description:**

A quantitative analysis of sodium and potassium was performed on a contraAA800D (Analytic Jena) with flame atomization and short arc Xe lamp. The sample (40 mg) was placed in quartz crucible where sodium and potassium were extracted from the sample by aqua regia. The acidic solution containing alkaline metal ions were atomized in an air/acetylene flame and sodium and potassium were quantified by measuring the absorbance at 589 and 766 nm, respectively, where their content was shown as weight percent (wt%).

**2.3.7 Analysis of carbon impurities**

Elemental analysis is used for rapid determination of carbon in various samples from organic matrices to inorganic materials. The working principle of the carbon analysis relies on high-temperature catalytic combustion of the sample in an oxygen enriched atmosphere. The combustion oxidizes solid carbon from the sample into gaseous CO<sub>2</sub> which was then carried out by a gas flow and analyzed by an IR detector. For example, in our studies, carbon analysis was applied to determine the amount of carbon impurities in the self-doped TiO<sub>2</sub> samples. The advantage of the combustion method is that total carbon impurities, both surface and bulk, can be determined.

**Experimental description:**

A multianalyzer TruSpec (Leco) was used for the quantitative analysis of carbon. The sample (10 mg) was placed in a Ag crucible where the sample is catalytically combusted in O<sub>2</sub>/He flow at 1100 °C. The CO<sub>2</sub> that has been formed during combustion was quantified by an IR detector and the carbon content was shown as weight percent (wt%).

### 3. Impact of $\text{Ti}^{3+}$ ions on light harvesting and photocatalytic activity of self-doped $\text{TiO}_2$ as seen from solar $\text{H}_2$ production

#### 3.1 Synthesis of self-doped $\text{TiO}_2$ and composition analysis

Self-doped blue titanium dioxide (B- $\text{TiO}_2$ ) was synthesized in the reaction of  $\text{TiO}_2$  and sodium-potassium alloy (Na/K) in dimethoxyethane (DME) at room temperature (fig 18).<sup>136</sup>

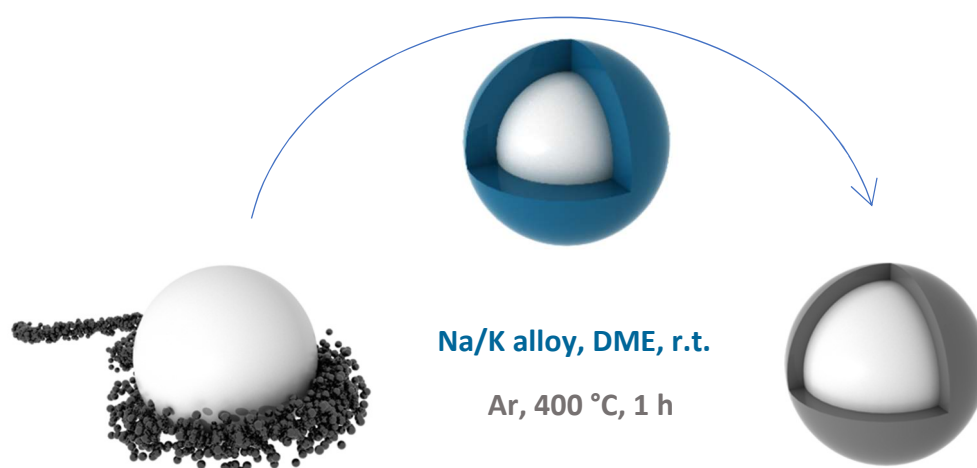


Figure 18. Synthesis of blue titania in reaction of  $\text{TiO}_2$  with Na/K alloy and synthesis of grey titania by thermal annealing at 400°C for 1h in Ar atmosphere.

The reaction is based on a reduction of  $\text{Ti}^{4+}$  ion to  $\text{Ti}^{3+}$  ion with electrons from Na/K alloy according to the equation 3.1:



In general, the reaction between  $\text{TiO}_2$  and Na/K alloy could proceed in two ways: by transfer of solvated electrons to  $\text{TiO}_2$  or by direct electron transfer from Na/K to  $\text{TiO}_2$  and subsequent injection of electrons into empty 3d orbitals of  $\text{Ti}^{4+}$  ion. For example, when reaction is attempted in the absence of  $\text{TiO}_2$ , a “blue solution” of solvated electrons in DME cannot be obtained under applied reaction conditions.<sup>145</sup> This implies

that reaction involving transfer of solvated electrons from solution to the  $\text{TiO}_2$  is not likely to occur. Hence, the reaction mechanism that considers direct electron transfer from Na/K alloy to  $\text{TiO}_2$  framework is presumably the dominant in the synthesis of B- $\text{TiO}_2$ .

Further, the transfer of electrons can occur, for example, by a contact of Na/K alloy with the surface of  $\text{TiO}_2$  or in the  $\text{TiO}_2$  bulk, where the latter would require intercalation of alkaline metals into  $\text{TiO}_2$  framework. The intercalation, generally, depends on the properties of intercalant and structure of the host.<sup>37, 38, 51, 52, 136, 146, 147</sup> When compared with layered inorganic hosts e.g., graphene nanoribbons, where alkaline metals easily intercalate and deintercalate from the graphene host, in  $\text{TiO}_2$  fast intercalation/deintercalation is less likely to occur.<sup>136</sup> The diffusion channels in  $\text{TiO}_2$ , where intercalation predominantly happens, reduce the contact area with surrounding media and limit the diffusion rate in and out of  $\text{TiO}_2$ . Thus, diffusion in  $\text{TiO}_2$  takes longer, while stable  $\text{TiO}_2$  intercalation compounds are expected to be formed. Another aspect where  $\text{TiO}_2$  structure differs from graphene nanoribbons is structural rigidity of  $\text{TiO}_2$ . The  $\text{TiO}_2$  structure does not allow excessive lattice expansion as in case of layered material (particularly interlayer distance), therefore, the size match between intercalant and diffusion channels in  $\text{TiO}_2$  is becoming a primary determinant if intercalation compound can be formed.<sup>38, 51, 52, 146, 147</sup> While the intercalation of smaller Na is feasible into  $\text{TiO}_2$  framework, potassium intercalation is restricted due to its big radius. Thus, formation of Na- $\text{TiO}_2$  intercalation compound could be potentially expected in the reaction of  $\text{TiO}_2$  with Na/K alloy.

Generally, the reaction between Na/K and  $\text{TiO}_2$  proceeds slowly. During reaction, three distinct stages in the reaction dynamics were observed: first, a 15 minutes sonication of reaction mixture caused that initially white suspension turns the color to light blue; second, in the first few days of reaction the alloy was rapidly consumed and the blue tone of B- $\text{TiO}_2$  progressively darkened; third, the reaction of  $\text{TiO}_2$  with the rest of the Na/K alloy was substantially slowed down, taking in total 70 days for completion. Moreover, during the third stage no further change in the color of B- $\text{TiO}_2$  occurred. Taken together, it can be inferred that first two stages in the synthesis, particularly the second one, is the one where self-doping of  $\text{TiO}_2$  grossly takes place. After synthesis the B- $\text{TiO}_2$  was worked-up with diluted HCl (0.2 M) to wash away alkaline impurities from the surface of material. Its blue color remained unchanged after work-up and color of as-prepared B- $\text{TiO}_2$  has not bleached over two years of storing the sample under ambient conditions.

The  $\text{TiO}_2$  intercalation compounds with alkaline metals, particularly Na- $\text{TiO}_2$ , are prone to Na deintercalation when exposed to elevated temperatures.<sup>148</sup> Thus, to check for Na intercalation into B- $\text{TiO}_2$ , the sample was thermally annealed. Here, an annealing atmosphere and temperature are meaningful input parameters. For instance, if the oxidative atmosphere is employed during annealing, the present oxygen will reoxidize

Ti<sup>3+</sup> ion to Ti<sup>4+</sup> ion, which can screen an effect that Na deintercalation may have on Ti<sup>3+</sup> ions in B-TiO<sub>2</sub>. Also, if the annealing temperature exceeds the onset temperature of anatase-to-rutile transformation, phase transformation can induce that Na diffuses out of TiO<sub>2</sub> framework due to the different structure in anatase and rutile polymorphs, particularly structure of diffusion channels.<sup>37 51</sup> Therefore, in such case it will become hard to entangle extent to which heating of B-TiO<sub>2</sub> impacts the Na deintercalation from the effect of phase transformation.

To determine the phase transformation temperature in B-TiO<sub>2</sub>, in situ XRD measurement was carried out. The evolution of B-TiO<sub>2</sub> crystal structure was monitored from room temperature to 800 °C in the 10-26° 2 Theta range and results are shown in figure 19.

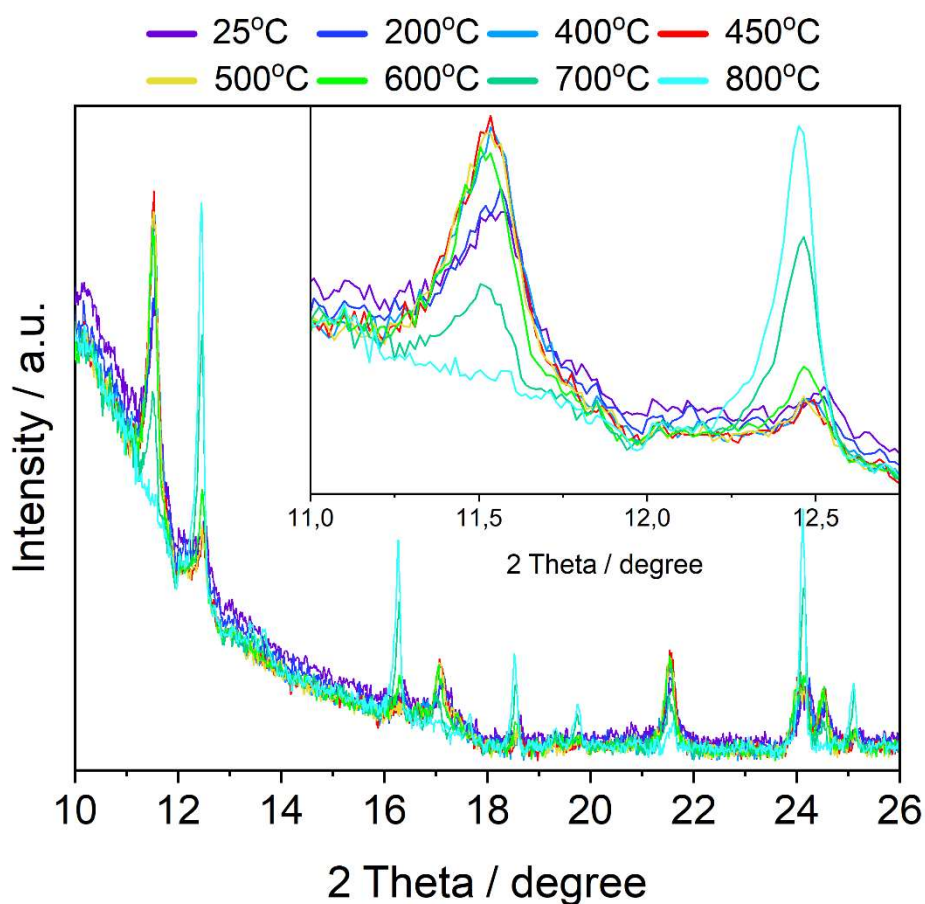


Figure 19. In-situ XRD pattern of blue titania. The pattern was acquired in Bragg-Brentano geometry using the Mo anode. The inset enlarges the patterns of 2 Theta region from 11 to 13° where anatase 101 and rutile 110 Bragg peaks appear at 11.5 and 12.4 2 Theta degrees, respectively.

From XRD patterns it can be noticed that the signal of anatase 101 peak reaches maximum value at temperature of 450 °C, while above 500 °C rutile 110 peak starts to enhance suggesting that anatase-to-rutile phase transformation starts taking place.<sup>34</sup> When the temperature is further increased, for example to 800 °C, the anatase diffraction peak cannot be anymore observed in the pattern, meaning that the anatase phase is completely transformed into rutile (rutilized). Considering in situ XRD results, the temperature of B-TiO<sub>2</sub> annealing was fixed to 400 °C, which balanced between the thermal healing of anatase phase and anatase-to-rutile phase transformation. The annealing was carried out in inert atmosphere of argon for 1 h. Upon annealing, the blue color of B-TiO<sub>2</sub> turned to grey (G-TiO<sub>2</sub>). The color shift indicates thermally induced changes in the B-TiO<sub>2</sub>. The color of the G-TiO<sub>2</sub>, like of B-TiO<sub>2</sub>, has exhibited profound long-term stability against fading upon storage under ambient conditions.

Now, having the four different TiO<sub>2</sub> samples (see experimental section), pristine TiO<sub>2</sub> (TiO<sub>2</sub>), self-doped TiO<sub>2</sub> (B-TiO<sub>2</sub>), annealed B-TiO<sub>2</sub> (G-TiO<sub>2</sub>) and acidic worked-up G-TiO<sub>2</sub> (G-TiO<sub>2</sub>/AC), surface and bulk elemental analysis was carried out aiming to check following hypotheses related to self-doping reaction mechanism:

- The intercalation of Na into TiO<sub>2</sub> is involved in the formation of B-TiO<sub>2</sub>.
- Na deintercalation from B-TiO<sub>2</sub> during annealing is caused by thermal effect that does not require phase transformation.
- Acidic work-up efficiently removes metal impurities from the surface of TiO<sub>2</sub>, but not intercalated impurities from the TiO<sub>2</sub> bulk.

The elemental analysis of TiO<sub>2</sub> samples was performed by XPS, AAS, and multianalyzer and results are summarized in figure 20. XP analysis was carried out to study the surface impurities in the TiO<sub>2</sub> samples. Figure 20 left shows normalized survey XP spectra in the range of 0 to 1200 eV. In all four samples Ti and O were the main surfaces constituents, while some carbon can be observed as well. Based on the XP spectra, the surface of TiO<sub>2</sub> and B-TiO<sub>2</sub> samples seem to be comparable. An absence of Na and K signals in B-TiO<sub>2</sub> suggests that work-up with diluted HCl removes alkaline impurities from the B-TiO<sub>2</sub> surface. This is consistent with the literature reporting that Li residues are completely removed from TiO<sub>2</sub> surface by a work-up with diluted acid.<sup>86</sup> The most notable differences among the TiO<sub>2</sub> surfaces, however, occur after annealing of B-TiO<sub>2</sub> and subsequent acidic work-up of G-TiO<sub>2</sub> sample. In G-TiO<sub>2</sub> spectra, for example, the intensity of the peak in Ti Auger region is substantially enhanced. This peak, beside the Ti Auger signal, can be contributed by Na 1s signal as well, since two signals overlap in TiO<sub>2</sub>. In case of G-TiO<sub>2</sub>, though, it is less likely that the increase in the signal comes from Ti Auger contribution, because all the other peaks stayed grossly the same. Therefore,

the signal increase is presumably related to surface Na impurities. The fact that Na appears at the surface of G-TiO<sub>2</sub> may indicate first, that a formed Na-TiO<sub>2</sub> intercalation compound is stable against diluted acid and second, that Na deintercalates from B-TiO<sub>2</sub> upon annealing. However, it should be mentioned that high resolution XP analysis would be required to confirm and quantify the amount of sodium at the TiO<sub>2</sub> surface, but, as being said previously this is not straightforward since the Na 1s signal overlaps with Ti Auger signal. Nevertheless, XP analysis can provide valuable insight into trends of the surface composition of TiO<sub>2</sub> samples. Another change in surface composition is observed in G-TiO<sub>2</sub>/AC sample. After acidic work-up, Na 1s signal in G-TiO<sub>2</sub>/AC is reduced and becomes comparable to the signal detected in TiO<sub>2</sub> or B-TiO<sub>2</sub>, meaning that once Na is exposed to the surface of TiO<sub>2</sub> it can be washed away with acid. It is also noteworthy that while the surface content of Na varied from sample to sample, potassium at the same time was not detected at all at the surfaces of TiO<sub>2</sub> samples.

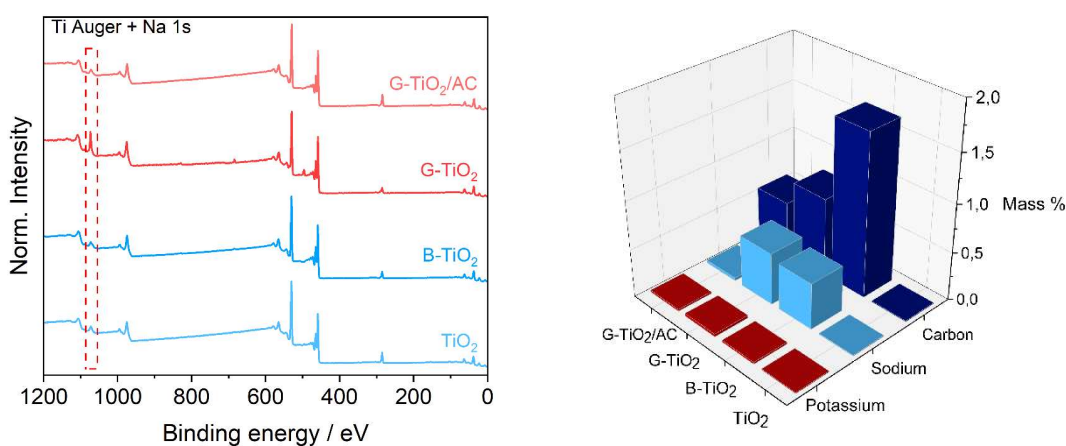


Figure 20. Elemental analysis of TiO<sub>2</sub> samples. Survey XP spectra (left) and bulk sodium, potassium, and carbon content (right) in TiO<sub>2</sub> samples.

The most relevant impurities in TiO<sub>2</sub> samples, sodium, potassium and carbon were further analysed by tracking their content in the bulk. The content of bulk impurities in TiO<sub>2</sub> samples is graphically presented in figure 20, right. In TiO<sub>2</sub> the amount of sodium, potassium and carbon was 0.01 wt.%, which implies that pristine TiO<sub>2</sub> was virtually free from impurities. The self-doped B-TiO<sub>2</sub> sample contained comparable amount of potassium (0.02 wt%) as in case of pristine TiO<sub>2</sub>, but sodium and carbon content increased to 0.48 and 1.68 wt%, respectively. The increase of sodium amount in B-TiO<sub>2</sub> shows that only sodium diffuses into TiO<sub>2</sub> during B-TiO<sub>2</sub> synthesis and intercalates into the TiO<sub>2</sub> framework, which is consistent with the survey XP results as well as

literature.<sup>38</sup> In G-TiO<sub>2</sub>, on one hand, no obvious change in sodium and potassium content was observed. On the other hand, the amount of residual carbon was cut by half to 0.81 wt%. The partial removal of carbon impurities can be due to the moderate temperature that was applied during thermal annealing as well as inert atmosphere and short annealing time. In G-TiO<sub>2</sub>/AC sample, acidic work-up did not show any effect on potassium. The potassium amount was small (0.02 wt%) and it is comparable to either the B-TiO<sub>2</sub> or G-TiO<sub>2</sub> sample. However, the content of sodium impurities dropped from 0.55 wt% to 0.03 wt%. The sharp drop in sodium level implies that once present at the surface, sodium can be removed by diluted acid, substantiating the conclusion derived from XP data. Even though the carbon content was further decreased by acidic work-up, the residual amount of carbon in G-TiO<sub>2</sub>/AC was still relatively high, exceeding 0.5 wt%. The carbon impurities in G-TiO<sub>2</sub> and G-TiO<sub>2</sub>/AC samples, among other, could be a reason for materials' grey color and their influence on features of G-TiO<sub>2</sub> and G-TiO<sub>2</sub>/AC will be discussed in the following chapters.

After surface and bulk elemental analysis being carried out, following conclusions on the three hypotheses based on the data can be drawn:

- The data approves that upon self-doping of TiO<sub>2</sub> with Na/K alloy, Na intercalates into TiO<sub>2</sub> framework. This may suggest that in case of Na, its diffusion into TiO<sub>2</sub> precedes the electron transfer reaction. Conversely, the surface electron transfer appears to be more likely in the case of K since it is restricted to diffuse into the bulk of TiO<sub>2</sub>.
- Results show that Na-TiO<sub>2</sub> intercalation compound is stable against diluted acid. Alternatively, long contact time or high acid concentration could facilitate diffusion of Na out of B-TiO<sub>2</sub>. Also, deintercalation of Na from the TiO<sub>2</sub> framework can be achieved at elevated temperatures and deintercalation is a thermally driven process requiring no rutile formation.
- XP and AAS results confirm that washing of samples with diluted HCl efficiently removes Na from the surface, but not the intercalated one from the bulk. This raises the question which is often overlooked in the literature reporting self-doped or colored TiO<sub>2</sub>, that is that TiO<sub>2</sub> can become doped by used reducing agent along with self-doping with Ti<sup>3+</sup> ions. Double doping in certain cases can be a reason for enhanced stability and photocatalytic activity of self-doped TiO<sub>2</sub> materials. Also, this shows that the use of surface analysis methods only is not sufficient for characterization of self-doped samples, but doping should be studied in the conjunction with analysis methods that allow the bulk to be studied.

## 3.2 Crystal structure and morphology of self-doped TiO<sub>2</sub>

Since the crystal structure of TiO<sub>2</sub> samples has been already briefly introduced in the previous section, here the in-depth structure of TiO<sub>2</sub> samples as well as microstructural parameters like crystallite size and interplanar spacing will be discussed. Moreover, structure and morphology analysis by TEM will be further discussed in the context of proposed structure based on XRD data.

The XRD pattern of starting TiO<sub>2</sub> material recorded in the 5-80 2 Theta degree range contains diffraction peaks indexed to the tetragonal anatase (icdd\_pdf\_01-076-3177) and rutile (icdd\_pdf\_00-021-1276) crystal phases (figure 21, top), which confirms the mix-phased character of pristine TiO<sub>2</sub>. Ti<sup>3+</sup> centres created by self-doping of TiO<sub>2</sub> in the reaction with Na/K alloy are expected to disrupt the crystal structure of the TiO<sub>2</sub> host.<sup>87</sup> XRD analysis reveals that upon self-doping, the intensity of anatase diffraction peaks in B-TiO<sub>2</sub> sample decreases compared to pristine TiO<sub>2</sub>. The signal decrease does not show facet selectivity, all anatase diffraction peaks are affected by the reaction. While anatase phase being affected by Na/K alloy, the signals of rutile diffraction peaks at the same time remained grossly unaltered. Such behavior of mixed-phase TiO<sub>2</sub> has been previously observed in the reaction of TiO<sub>2</sub> with Na metal. There, it was speculated that chemical inertness of rutile phase might be a reason for selective modification of anatase phase in mixed-phase TiO<sub>2</sub>.<sup>87</sup> This hypothesis will be addressed later in the chapter. As a result of thermal treatment, the signals of anatase peaks in G-TiO<sub>2</sub> are recovered, though partially, while rutile signals seem to be unaffected by thermal treatment. This finding is consistent with in situ XRD measurements indicating that at 450 °C the anatase phase exhibits a maximum intensity of diffraction peaks (fig. 19). For example, longer annealing times at 400 °C could lead to complete healing of the anatase phase.<sup>34</sup> In G-TiO<sub>2</sub>/AC the acidic work-up did not show much effect on the XRD pattern, giving the pattern that is very similar to the pattern of G-TiO<sub>2</sub>.

The changes in microstructural parameters, such as crystallite size and interplanar d-spacing, induced by self-doping and thermal annealing were further studied on TiO<sub>2</sub> samples. The average crystallite size was calculated employing Scherrer method for two of the most intensive Bragg peaks in anatase phase ((101) and (200)) and rutile phase ((110) and (111)) that do not overlap with other peaks. The data on crystallite sizes and d-spacing of anatase and rutile phase for TiO<sub>2</sub> samples is summarized in Table 3. In pristine TiO<sub>2</sub>, generally, crystallites of rutile phase are bigger than that of anatase phase. Also, the crystallites in TiO<sub>2</sub> exhibit a phase dependent crystallite size variation, where smaller anatase crystallites vary more in size due to self-doping and thermal annealing. For example, the average crystallite size in (101) and (200) anatase planes in pristine TiO<sub>2</sub> were 23.5 and 21.1 nm, respectively, while in B-TiO<sub>2</sub> were reduced to 22.0 and 18.7 nm, respectively. The decrease of average crystallite size in rutile phase is not



Table 3. Crystallite size (D) and d-spacing (d) in TiO<sub>2</sub> samples

Sample	D <sub>101</sub> / nm	D <sub>200</sub> / nm	D <sub>110</sub> / nm	D <sub>111</sub> / nm	d <sub>101</sub> / nm	d <sub>110</sub> / nm
TiO <sub>2</sub>	23,5	21,1	31,4	36,0	0,352	0,325
B-TiO <sub>2</sub>	22,0	18,7	31,1	36,1	0,352	0,325
G-TiO <sub>2</sub>	23,4	20,6	32,4	34,8	0,352	0,325
G-TiO <sub>2</sub> /AC	23,3	20,9	32,1	33,8	0,352	0,325

confirmed upon TiO<sub>2</sub> self-doping. The shrinkage of crystallites in anatase phase may indicate that amorphous overlayer in B-TiO<sub>2</sub> sample is formed as a consequence of self-doping.<sup>86</sup> Such modification of surface layer is a common phenomenon occurring in post-growth diffusion-based synthetic routes like reaction of crystalline TiO<sub>2</sub> with Na/K alloy where amount of inserted Na is relatively low. In some instances, though, alkalis can be intercalated to greater extent into TiO<sub>2</sub> framework such by electrochemical insertion.<sup>149</sup> The high alkaline content may trigger the formation of titanate phases, which is sharp contrast comparing with B-TiO<sub>2</sub>. In the G-TiO<sub>2</sub> sample it is observed that anatase crystallites grow in (101) and (200) planes to 23.4 and 20.6 nm, respectively. According to the results, the crystallites are completely recovered in (101), but not fully in (200) plane. The acid treatment of G-TiO<sub>2</sub> sample did not further affect the size of anatase crystallites. On the other hand, minor changes in rutile crystallites were observed in G-TiO<sub>2</sub>, where simultaneous growth of crystallite in (110) rutile plane and shrinkage in (111) plane are confirmed. The increase of crystallites in crystal ab plane (110) presumably occurs on the expense of high energy facets, meaning that high energy surfaces are converted upon thermal annealing to the most thermodynamically stable (110) surface.<sup>40, 150</sup> The similar thermal phenomenon of crystallites can be operable for the anatase phase as well, which may explain why crystallites in the thermodynamically most stable (101) plane is completely recovered although the anatase signal in the XRD pattern is not.<sup>40, 150</sup> Despite the subtle thermal effect could be observed upon annealing, based on XRD data the anatase-to-rutile phase transformation can be excluded to occur in TiO<sub>2</sub> samples.

For d-spacing calculation the most intensive anatase (101) and rutile (110) diffraction signals in TiO<sub>2</sub> samples were utilized. The d-spacing was determined employing Bragg equation. The interplanar spacing for (101) and (110) Bragg diffraction peaks in all TiO<sub>2</sub> samples were the same, 0.352 and 0.325 nm, the values that are typical for defect-free anatase and rutile phase. These results may suggest that the core of the particles that is left after reaction with Na/K retains the structure of pristine TiO<sub>2</sub> and allows for distinguishing between an outer layer with distorted structure and an unmodified crystalline TiO<sub>2</sub> core.

Now, after the crystal structure of  $\text{TiO}_2$  samples have been comprehensively discussed, the selective modification of the anatase phase in mixed-phase  $\text{TiO}_2$  upon self-doping will be addressed. As mentioned previously, it has been speculated that the chemical inertness of the rutile phase might be a reason why only anatase becomes affected by self-doping in mixed-phase  $\text{TiO}_2$ .<sup>87</sup> In the case when mixed-phase  $\text{TiO}_2$  was replaced by pure rutile  $\text{TiO}_2$  nanoparticles and reaction with Na/K alloy runs under otherwise same reaction

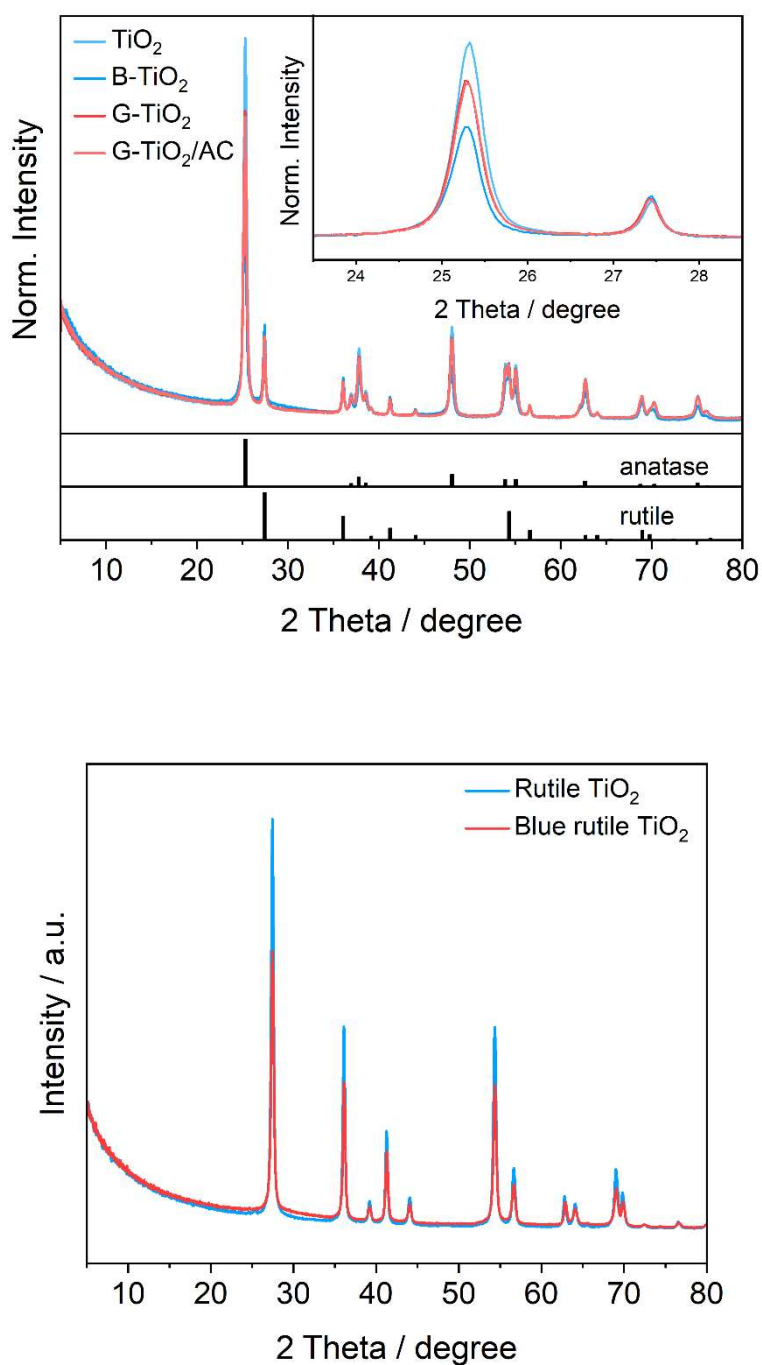


Figure 21. XRD patterns of  $\text{TiO}_2$ , B- $\text{TiO}_2$  and G- $\text{TiO}_2$  nanoparticles and pdf cards of the anatase (icdd-pdf-01-076-3177) and rutile (icdd-pdf-00-021-1276) crystal phase (top) and XRD patterns of rutile  $\text{TiO}_2$  and blue rutile  $\text{TiO}_2$  (bottom)

conditions, blue rutile  $\text{TiO}_2$  was obtained. Due to strong similarities with the color change observed for mixed-phase  $\text{TiO}_2$ , it is expected that self-doping of rutile  $\text{TiO}_2$  occurred in the reaction with Na/K alloy. To substantiate the experimental observation, XRD analysis of white and blue rutile  $\text{TiO}_2$  was carried out (figure 21, bottom). From these patterns it become clear that the intensity of signals in blue rutile  $\text{TiO}_2$  is decreased comparing with white rutile  $\text{TiO}_2$  in the similar fashion like in the anatase phase of mixed-phase  $\text{TiO}_2$ . This shows that the rutile phase is not chemically inert under reaction conditions, but more likely the different affinity toward Na/K alloy as well as the surface energy of anatase and rutile polymorphs might play a role here.<sup>52,</sup>

53

The structure and morphology of the  $\text{TiO}_2$  samples were further studied by transmission electron microscopy (TEM). High-angle annular dark field scanning transmission electron microscopy (HAADF)-STEM was employed for structural analysis and micrographs of  $\text{TiO}_2$ , B- $\text{TiO}_2$ , and G- $\text{TiO}_2$  are depicted in figure 22, left. The micrograph of pristine  $\text{TiO}_2$  shows that  $\text{TiO}_2$  has faceted particles with a resolved edge and lattice features, which indicate that the starting material is well crystallized (fig. 22, top left). In B- $\text{TiO}_2$  (fig. 22, middle left), the main effect of self-doping is reflected in roughening of the particle's surface. Meanwhile the surface of particles is altered, the crystalline core remains defined. In general, the alteration becomes more pronounced for particles with smaller diameter. The STEM results on B- $\text{TiO}_2$  confirm that the surface layer undergoes modifications in the reaction with Na/K and that Na intercalation is a diffusion-driven process, meaning that particles with higher surface-to-volume ratio are modified to a greater extent. In G- $\text{TiO}_2$  (fig. 22, bottom left) the disordered overlayer considerably shrank. The particles show more regular edge structure in comparison with B- $\text{TiO}_2$ , but less defined than that of pristine  $\text{TiO}_2$ . Thus, the STEM analysis points out that ascending order of crystallinity in the three samples is as follows: B- $\text{TiO}_2$ , G- $\text{TiO}_2$  and pristine  $\text{TiO}_2$ . Furthermore, the STEM observations corroborate the XRD data that suggest the formation of a disordered overlayer in B- $\text{TiO}_2$  as well as partial healing of disordered structures upon thermal annealing. Apart from structural TEM analysis, the low-magnification bright-field (BF)-TEM images reveal that particle size distribution and morphology of particles in  $\text{TiO}_2$ , B- $\text{TiO}_2$ , and G- $\text{TiO}_2$  samples (fig. 22, top, middle, bottom right, respectively) did not change either after self-doping or thermal annealing.

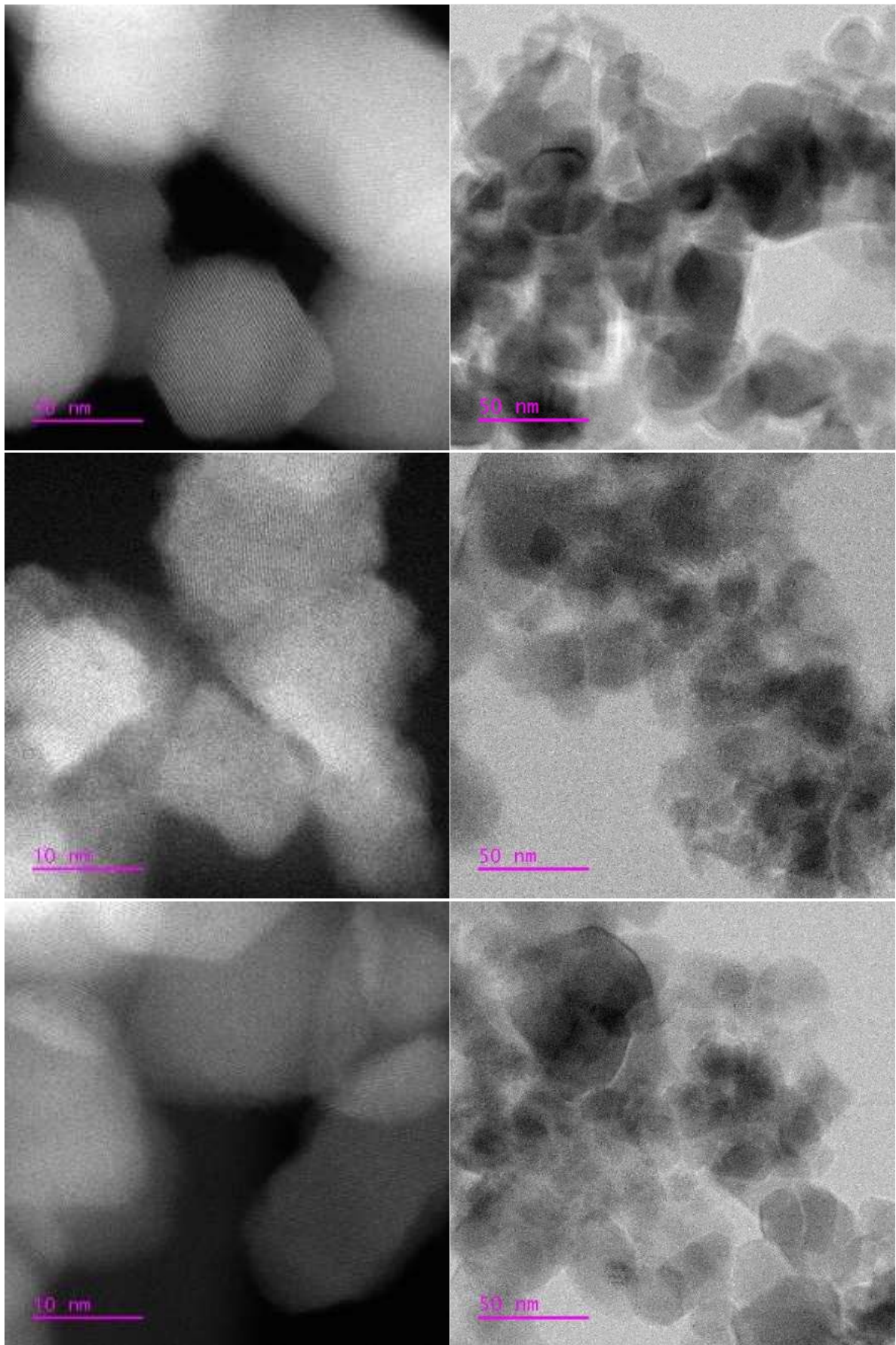


Fig. 22 HAADF - STEM and BF - TEM images of TiO<sub>2</sub> (top left and right), B-TiO<sub>2</sub> (middle left and right) and G-TiO<sub>2</sub> (bottom left and right) nanoparticles

### 3.3 Optical properties of self-doped TiO<sub>2</sub>

The light harvesting ability of TiO<sub>2</sub> samples was examined by means of diffuse reflectance spectroscopy (DRS) in the spectral range from 250 to 1100 nm and DRS spectra are shown in figure 23. The pristine TiO<sub>2</sub> exhibits band-to-band transition,

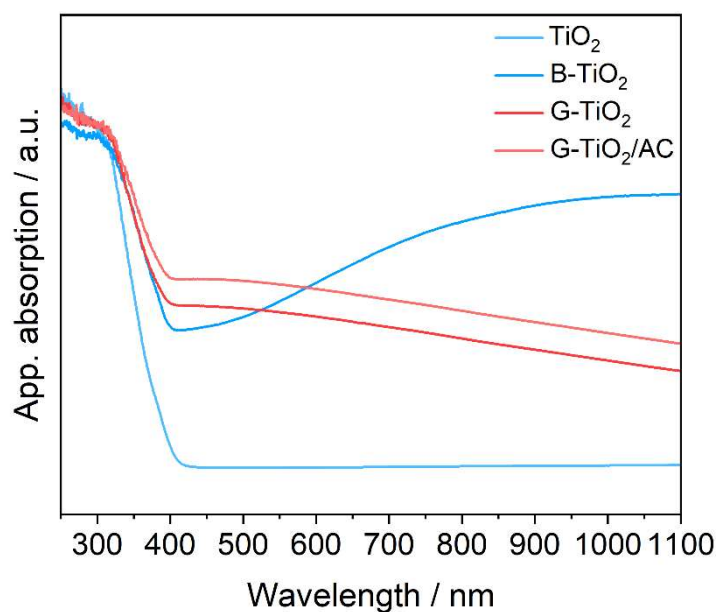


Figure 23. DRS spectra of TiO<sub>2</sub>, B-TiO<sub>2</sub>, G-TiO<sub>2</sub> and G-TiO<sub>2</sub>/AC samples

which implies that the TiO<sub>2</sub> structure is free of defects that act as color centres. In B-TiO<sub>2</sub> in addition to band gap absorption, strong light absorption in Vis and NIR region emerges, with NIR absorption being the dominant contributor. The deep Ti<sup>3+</sup> mid-gap states in B-TiO<sub>2</sub> that are introduced by TiO<sub>2</sub> self-doping induces the sub-band gap absorption. Consequently, the light harvesting capability of B-TiO<sub>2</sub> is greatly enhanced, thereby widening the range of sunlight that B-TiO<sub>2</sub> can capture and generate charge carriers for photocatalytic reactions. After thermal annealing the Vis/NIR light absorption of G-TiO<sub>2</sub> is still notable, but less intensive than that of the B-TiO<sub>2</sub> sample. Also, light absorption in G-TiO<sub>2</sub> is flipped, with the Vis light being absorbed to higher extent than the NIR. The reduction in NIR absorption could be assigned to a lack of Ti<sup>3+</sup> states in G-TiO<sub>2</sub>. This would, however, mean that thermal annealing induces not only the Na deintercalation from TiO<sub>2</sub>, but also destabilizes Ti<sup>3+</sup> ions in the TiO<sub>2</sub> framework. As of now, the influence of thermal annealing on Ti<sup>3+</sup> centres will not be further discussed, but instead it will be addressed in the following chapter. The sub-band gap absorption in G-TiO<sub>2</sub> can be roughly split into two regions. The first one, that falls

between 400-500 nm is characterized by an absorption plateau, while the second one lays above 500 nm and light absorption monotonically decreases throughout the rest of Vis and in NIR region. The origin of visible light absorption in the G-TiO<sub>2</sub> sample can be somewhat controversial and at least two explanations have been offered in the literature. On one hand, it has been shown that oxygen vacancies present in TiO<sub>2</sub> act as color defects, thus enabling absorption of visible light by TiO<sub>2</sub>.<sup>151</sup> On the other hand, doping of TiO<sub>2</sub> with carbon has been proven to enhance visible light absorption of TiO<sub>2</sub> in a similar way as in the case of G-TiO<sub>2</sub>.<sup>68, 152</sup> Since 0.81 wt% of carbon impurities was detected in G-TiO<sub>2</sub> sample, the carbon doping seems more likely to be responsible for color and light absorption of the sample. The G-TiO<sub>2</sub>/AC shows light absorption envelop very similar to that of G-TiO<sub>2</sub>, but with slightly enhanced intensity. Presumably, the increased light absorption can be attributed to the chemically clean G-TiO<sub>2</sub>/AC surface. After all, it can be concluded that the light harvesting ability of the TiO<sub>2</sub> samples follows the order: TiO<sub>2</sub><G-TiO<sub>2</sub><G-TiO<sub>2</sub>/AC<B-TiO<sub>2</sub>.

Next, the band gap of TiO<sub>2</sub> samples was determined from DRS data using Tauc analysis and results are presented in figure 24. At the beginning it should be mentioned that all studied samples show complex Tauc envelopes with multiple absorption edges. For example, pristine TiO<sub>2</sub> shows two absorption edges, the rutile edge at 3.05 eV and anatase edge at 3.30 eV, because the sample is a mixed-phase TiO<sub>2</sub>. However, the anatase absorption edge is dominant in the Tauc plot, because the anatase phase is the prevailing crystal phase in pristine TiO<sub>2</sub>. Therefore, in other TiO<sub>2</sub> samples a similar band

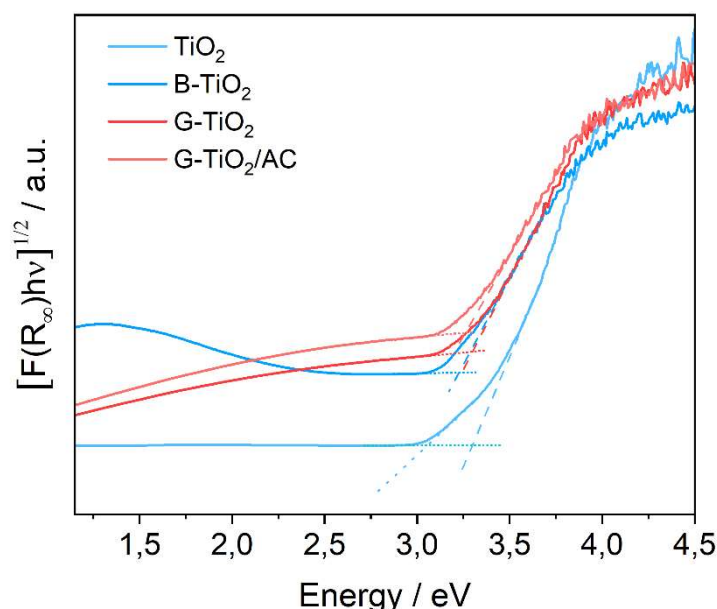


Figure 24. Tauc plots of TiO<sub>2</sub>, B-TiO<sub>2</sub>, G-TiO<sub>2</sub> and G-TiO<sub>2</sub>/AC samples

gap can be expected and for further discussion only the anatase edge of  $\text{TiO}_2$  will be considered due to two reasons: rutile is the minor phase in  $\text{TiO}_2$  and it was not affected by the reaction with Na/K alloy. Thus, the band gaps of B- $\text{TiO}_2$ , G- $\text{TiO}_2$  and G- $\text{TiO}_2/\text{AC}$  samples are 3.24, 3.29 and 3.26 eV, respectively, showing slight red-shift comparing with that of the pristine  $\text{TiO}_2$  sample.<sup>153</sup> Further, a sub-band gap part of the signal falling in Vis/NIR region can be used to study in-band electronic states in the samples. In three samples that show Vis/NIR absorption the analysis of in-band electronic states is convenient only in the case of B- $\text{TiO}_2$ . In G- $\text{TiO}_2$  and G- $\text{TiO}_2/\text{AC}$  samples, the lack of clear absorption features and a non-linear absorption decrease hamper further analysis. In Vis/NIR region the envelope of B- $\text{TiO}_2$  exhibits an absorption maximum at around 1.3 eV due to the  $\text{Ti}^{3+}$  deep electronic states in the anatase phase, which reasonably good matches with the position of  $\text{Ti}^{3+}$  in-band electronic states in  $\text{TiO}_2$  that has been reported in the literature.<sup>94, 154</sup>

In the next experiment, the influence of the  $\text{Ti}^{3+}$  concentration on the intensity of Vis/NIR light absorption in the self-doped  $\text{TiO}_2$  was studied (fig. 25, left). Here, the self-doped  $\text{TiO}_2$  samples were prepared applying standard reaction conditions, with differences being the reaction time (limited to 5 days) and amount of added alloy (samples are denoted as B- $\text{TiO}_2_x$ , where x represents the amount of added Na/K alloy (mL)). Additionally, the amount of bulk sodium, potassium and carbon were quantified in B- $\text{TiO}_2_x$  samples (fig. 25, right).

DRS results show that the light harvesting ability of B- $\text{TiO}_2_x$  samples depend on the amount of added alloy i.e.,  $\text{Ti}^{3+}$  concentration. Initially, a rapid increase in Vis/NIR light absorption is observed when the volume of Na/K alloy increases from 0.25 to 1 mL. The light absorption for the B- $\text{TiO}_2_1$  sample reaches its maximum and a further increase

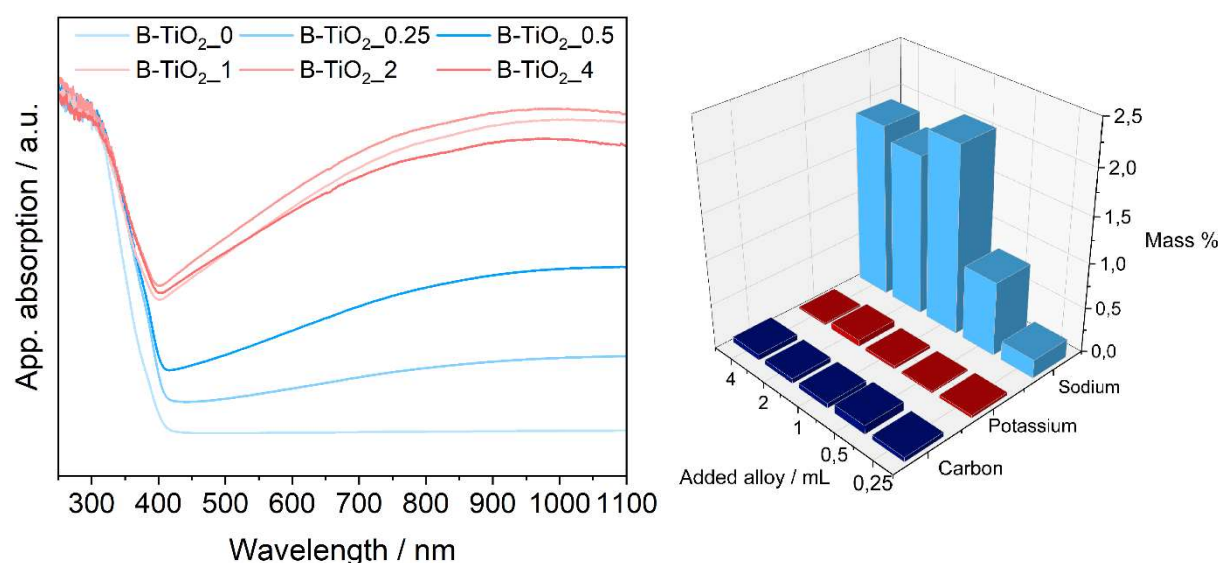


Figure 25. DRS spectra (left) and content of bulk sodium, potassium and carbon impurities (right) in B- $\text{TiO}_2_x$  samples

in the Na/K amount does not enhance the Vis/NIR absorption in B-TiO<sub>2</sub>\_2 and B-TiO<sub>2</sub>\_4 samples. The DRS results can be substantiated by the development of the color of B-TiO<sub>2</sub>\_x: the blue color darkens from B-TiO<sub>2</sub>\_0.25 to B-TiO<sub>2</sub>\_0.5 and become dark blue for the sample B-TiO<sub>2</sub>\_1. For B-TiO<sub>2</sub>\_2 and B-TiO<sub>2</sub>\_4 samples no obvious difference in color comparing with B-TiO<sub>2</sub>\_1 could be anymore observed. Altogether, this reveals that the maximum concentration of Ti<sup>3+</sup> centres in B-TiO<sub>2</sub>\_x samples is likely reached in the case of 1 mL of added Na/K alloy.

Next, a possible correlation of optical absorption and level of impurities in the B-TiO<sub>2</sub>\_x samples were studied. Generally, accumulation of either potassium or carbon does not occur in B-TiO<sub>2</sub>\_x. Their amount is almost constant throughout the B-TiO<sub>2</sub>\_x series and does not exceed 0.1 wt.%. (fig 25, right). Such low amount of potassium can be expected since potassium does not intercalate into the TiO<sub>2</sub> framework. However, in the case of carbon the results are surprising, particularly concerning the fact that carbon accumulation in B-TiO<sub>2</sub> sample was well above 1 wt.%. The reason for a low amount of carbon in B-TiO<sub>2</sub>\_x samples could be the short reaction time, which would not allow carbon impurities to accumulate in the disordered layer. On the other hand, the sodium accumulation in bulk is in sharp contrast either to potassium or carbon accumulation, presumably because the change in reaction conditions does not affect Na intercalation. For example, the Na content increases until B-TiO<sub>2</sub>\_1, where the TiO<sub>2</sub> framework becomes saturated with intercalated Na and Na content does not further change. In fact, the Na intercalation and Vis/NIR absorption in B-TiO<sub>2</sub>\_x strongly correlates. This correlation may imply that impurities other than Na are spectators in B-TiO<sub>2</sub> and suggests that Na can be essential for self-doping and stabilization of Ti<sup>3+</sup> ions in B-TiO<sub>2</sub>.

### 3.4 Study of Ti<sup>3+</sup> ions in self-doped TiO<sub>2</sub>

Upon TiO<sub>2</sub> self-doping, the extra electron from Na/K alloy is injected into empty 3d orbitals of Ti<sup>4+</sup> ion forming Ti<sup>3+</sup> ion. The increased electron density around Ti cation then triggers a shift in its bound state as well as change of magnetic properties from diamagnetic to paramagnetic, which represents a basis for studying self-doped TiO<sub>2</sub> by X-ray photoelectron spectroscopy (XP) and electron paramagnetic resonance (EPR), respectively. Beside Ti<sup>3+</sup> detection, the combination of these method can reveal the depth profile of Ti<sup>3+</sup> centers in self-doped TiO<sub>2</sub>.

At the beginning, the chemical bonding of Ti and O ions at the surface of TiO<sub>2</sub> samples will be discussed. The Ti spectra were recorded in the 2p region and results are shown in figure 26, top. The doublet in the spectra of TiO<sub>2</sub> samples arises from spin orbit-splitting Ti 2p<sub>3/2</sub> and Ti 2p<sub>1/2</sub> of 5.8 eV that is characteristic for the Ti<sup>4+</sup> state in TiO<sub>2</sub>.<sup>28</sup> Herein, the surface differences in the samples are evaluated from the Ti 2p<sub>3/2</sub> peak,



which for pristine  $\text{TiO}_2$  has a binding energy of 458.6 eV. In  $\text{B-TiO}_2$ , the peak is shifted by ca. 0.4 eV towards Fermi level relative to the Ti  $2p_{3/2}$  centre in pristine  $\text{TiO}_2$ . Generally, the decrease in binding energy (BE) is an indication of an addition of a valence electron to the ion which lowers its oxidation state. In addition, the evidence

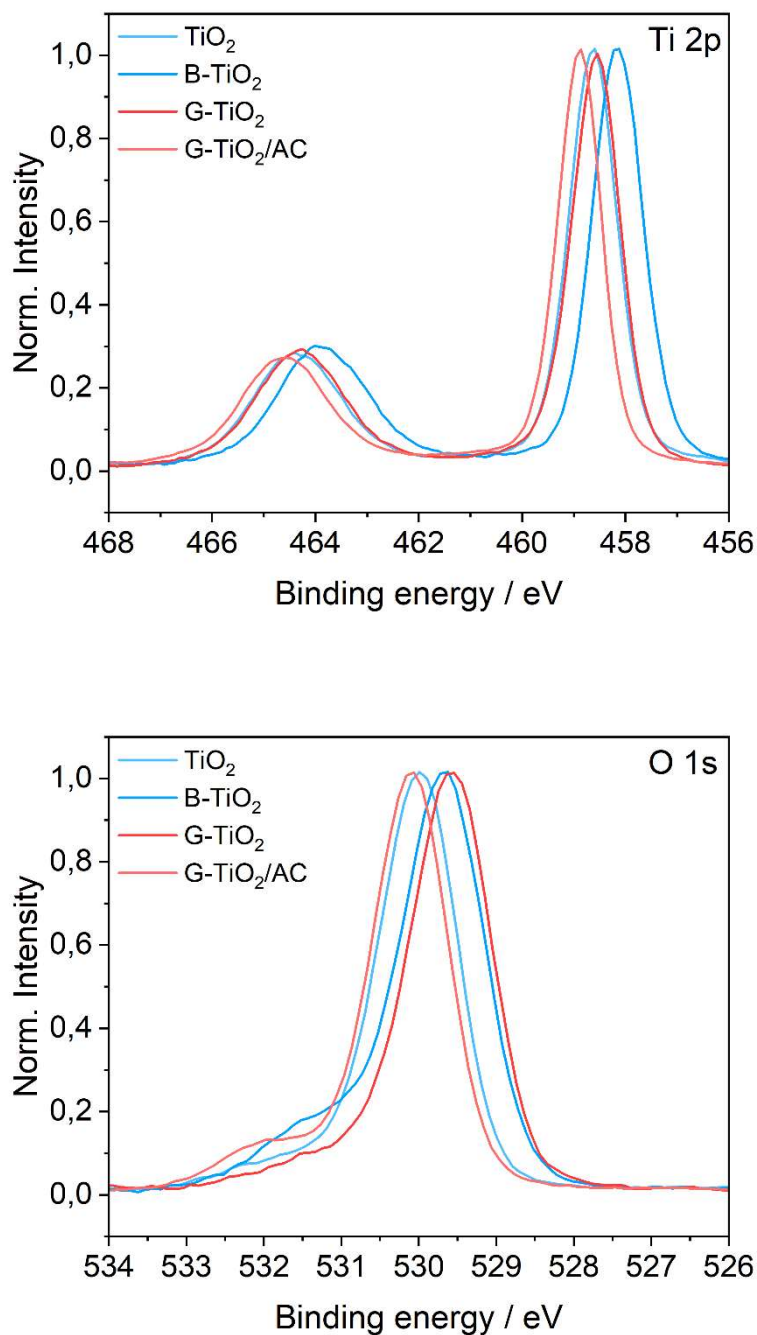


Figure 26. High-resolution XP spectra of  $\text{TiO}_2$ ,  $\text{B-TiO}_2$ ,  $\text{G-TiO}_2$  and  $\text{G-TiO}_2/\text{AC}$  samples in Ti 2p (top) and O 1s (bottom) region

for the presence of the surface  $\text{Ti}^{3+}$  ions could be the emergence of a low BE shoulder in the  $\text{Ti}^{4+}$  signal. In B- $\text{TiO}_2$ , however, no shoulder at the low BE side of the  $\text{Ti}^{4+}$  signal is detected, and the shift of 0.4 eV towards Fermi level is smaller than the shift of 1.5 eV that is expected in the case when  $\text{Ti}^{3+}$  ions are present on the  $\text{TiO}_2$  surface.<sup>155</sup> Also, it should be kept in mind that uncertainty in BE can be up to  $\pm 0.3$  eV, which can give rise to a shift in BE similar to the shift that is observed in B- $\text{TiO}_2$ . Therefore, Ti 2p results suggest that  $\text{Ti}^{3+}$  ions are not exposed at the surface of B- $\text{TiO}_2$  sample. Considering the uncertainty of measurements, no further changes in the Ti  $2p_{3/2}$  peak position are observed either in G- $\text{TiO}_2$  or G- $\text{TiO}_2/\text{AC}$  sample, where the Ti  $2p_{3/2}$  peak is centred at 458.6 and 458.9 eV, respectively. Hence, it can be inferred that the surface of all  $\text{TiO}_2$  samples is composed only out of  $\text{Ti}^{4+}$  ions.

Figure 26, bottom shows O spectra of  $\text{TiO}_2$  samples recorded in the 1s region. The main peak and the high BE shoulder in the O 1s region can be attributed to lattice oxygen and hydroxyl groups, respectively. Here, the surface differences in  $\text{TiO}_2$  samples are assessed from the lattice oxygen peak centred at 530.0 eV in pristine  $\text{TiO}_2$ . In B- $\text{TiO}_2$ , G- $\text{TiO}_2$  and G- $\text{TiO}_2/\text{AC}$  samples the lattice oxygen peak is centred at 529.7, 529.6 and 530.1 eV, respectively. For example, the 0.3 eV negative shift in BE observed in B- $\text{TiO}_2$  sample relative to the pristine  $\text{TiO}_2$  is assigned in the literature to the oxygen vacancies that are present in self-doped  $\text{TiO}_2$ .<sup>87</sup> In this case, however, similarly to the Ti 2p signal such small deviations in peak position fall out of reliability range of the measurement to allow plausibly assignment. Moreover, the negative shift of O 1s is comparable to the shift in the Ti 2p signal in B- $\text{TiO}_2$ , which implies that rather the whole spectrum of B- $\text{TiO}_2$  is equally affected i.e., slightly negatively shifted. Therefore, XP results suggest that no oxygen vacancies are present on the surface of the  $\text{TiO}_2$  samples.

In addition, in  $\text{TiO}_2$  and B- $\text{TiO}_2$  the O 1s and Ti 2p peaks show regular BE distance, which in the case of G- $\text{TiO}_2$  becomes smaller. These tiny negative shifts in BE have been observed for metal and metal oxide surfaces due to electrostatic interactions with ionic adsorbate layers.<sup>156, 157</sup> Therefore, in G- $\text{TiO}_2$  it is reasonable to assume that deintercalated Na present on the G- $\text{TiO}_2$  surface more affects surface oxygen than titanium, causing the negative shift of the O 1s peak and reducing the O 1s and Ti 2p BE distance.

Further, analysis of  $\text{Ti}^{3+}$  ions in  $\text{TiO}_2$  samples was performed by EPR at an X-band frequency (9.35 GHz) in the dark. To study relaxation in  $\text{TiO}_2$  samples, the measurements were conducted at two different temperatures, 96 K and 293 K. The sample tube and  $\text{TiO}_2$  did not give measurable signal under applied conditions, so they will not be further discussed. Also, the G- $\text{TiO}_2/\text{AC}$  sample was not measured, since the acidic work-up was not expected to have a significant influence on the EPR results of G- $\text{TiO}_2$  sample as showcased with previous methods. Therefore, the B- $\text{TiO}_2$  and G- $\text{TiO}_2$  samples were studied, and spectra are shown in figure 27.

At the beginning, the results of B-TiO<sub>2</sub> and G-TiO<sub>2</sub> at low temperatures will be discussed. The spectrum of B-TiO<sub>2</sub> recorded at 96 K indicates the presence of two paramagnetic centres. The first, more pronounced signal is the broad peak centred at  $g = 1.94$ . The general consensus assigns the signal to the Ti<sup>3+</sup> centres in TiO<sub>2</sub>.<sup>105, 158, 159</sup> Judging from the peak position, it can be ascribed to the subsurface/bulk Ti<sup>3+</sup> centres in B-TiO<sub>2</sub>, because the surface Ti<sup>3+</sup> centre would give a high-field signal at 1.92.<sup>105</sup> Therefore, the EPR data confirms that paramagnetic Ti<sup>3+</sup> species in B-TiO<sub>2</sub> are not exposed to the surface, but they are rather located at the subsurface or the bulk of the material. Apart from Ti<sup>3+</sup> peak, the less intensive low-field isotropic signal at  $g = 2.003$  can be observed as well. The assignation of this features is, however, a matter of heated debate in the literature.

To a greater extent, it is believed that the signal originates from electrons that become trapped at oxygen vacant sites, although medium polarized free electrons or carbon impurities have been proposed to contribute to this feature as well.<sup>86, 159-162</sup> For example, probably the heaviest critic concerning the oxygen vacancy model is that it cannot address the lack of interaction of molecular oxygen with oxygen vacant sites. Known as good electron scavenger, the adsorption of O<sub>2</sub> would cause an electron transfer from a vacant site to an O<sub>2</sub> molecule. As a result, the formation of a superoxide radical anion (O<sub>2</sub><sup>-</sup>), that would give a rhombic signal, is expected to occur.<sup>163</sup> However, the isotropic oxygen vacancy peak withstands in the presence of oxygen and the new signal from O<sub>2</sub><sup>-</sup> does not appear.<sup>86</sup> Since the vacancy model left short towards interaction with O<sub>2</sub>, the signal is alternatively assigned to the medium polarized free electrons, which would explain a slight difference in the observed  $g$  value in comparison with the  $g$  value of free electrons (2.003 vs. 2.0023, respectively) as well as the lack of interaction with oxygen. It should be noted, however, that both models, oxygen vacancy and medium polarized free electron model, assume that TiO<sub>2</sub> is free of impurities. The more realistic scenario is though that lab prepared TiO<sub>2</sub> samples will contain leftover impurities e.g., from synthesis of the catalyst. Therefore, a third model considers that the signal at  $g = 2.003$  originates from impurities, particularly from residual carbon. The similar signal like this is regularly detected in carbon containing samples including carbon doped TiO<sub>2</sub>, graphene oxide and its derivatives, but not in high-quality graphene.<sup>162, 164, 165</sup> Also, the signal is common in coals.<sup>166</sup> Thus, this might suggest that the signal derives from trapped electrons most likely at functional groups, though, the determination of the nature of this peaks was out of the scope of this thesis.<sup>164</sup> The fact that carbon impurities were confirmed in the B-TiO<sub>2</sub> cannot be ignored and, therefore, the peak centred at  $g = 2.003$  is to be due to the present carbon in B-TiO<sub>2</sub>.

In G-TiO<sub>2</sub> the intensity of the two EPR signals change; the intensity of the Ti<sup>3+</sup> signal heavily decreases while the carbon signal is intensified. As already shown by the DRS measurement (fig. 25, left), the amount of Na that intercalates into the TiO<sub>2</sub> framework influences the extent to which TiO<sub>2</sub> will be self-doped, thus determines the properties

of the material. This EPR measurement, on the other hand, shows that Na deintercalation out of  $\text{TiO}_2$  can result in the annihilation of  $\text{Ti}^{3+}$  ions. Hence, DRS and EPR analyses indicate that Na has a profound effect on the formation and stabilization of  $\text{Ti}^{3+}$  ions in B- $\text{TiO}_2$ . The changes in intensity of the carbon peak may be understood in the way that thermal treatment in inert atmosphere enhances the electron trapping ability of impurities.

When recorded at 293 K, the EPR envelope of B- $\text{TiO}_2$  contains signature resonances of both paramagnetic centres detected at low temperature. However, the intensity of the  $\text{Ti}^{3+}$  peak here is substantially weakened, which reveals an adverse effect of temperature increase on the  $\text{Ti}^{3+}$  signal. The variation of the  $\text{Ti}^{3+}$  signal with temperature can be explained by the impact of temperature on the spin-relaxation time.<sup>167</sup> Generally, spin-relaxation time shortens with temperature and this can be applied for the majority of paramagnetic signals. At the same time the carbon signal deflects from the regular temperature behaviour and stays grossly unaffected by temperature. In G- $\text{TiO}_2$  at 293 K the  $\text{Ti}^{3+}$  peak completely vanishes, while only the carbon peak is detected. As in case with B- $\text{TiO}_2$ , the carbon peak in G- $\text{TiO}_2$  shows irregular behaviour with temperature, the behaviour that is valid in the case of paramagnetic centres in reduced graphene oxide.<sup>164</sup> Also, the comparable peak characteristics in B- $\text{TiO}_2$  and G- $\text{TiO}_2$  may suggest the same nature of the trapping sites, which are likely enhanced by number after thermal annealing.

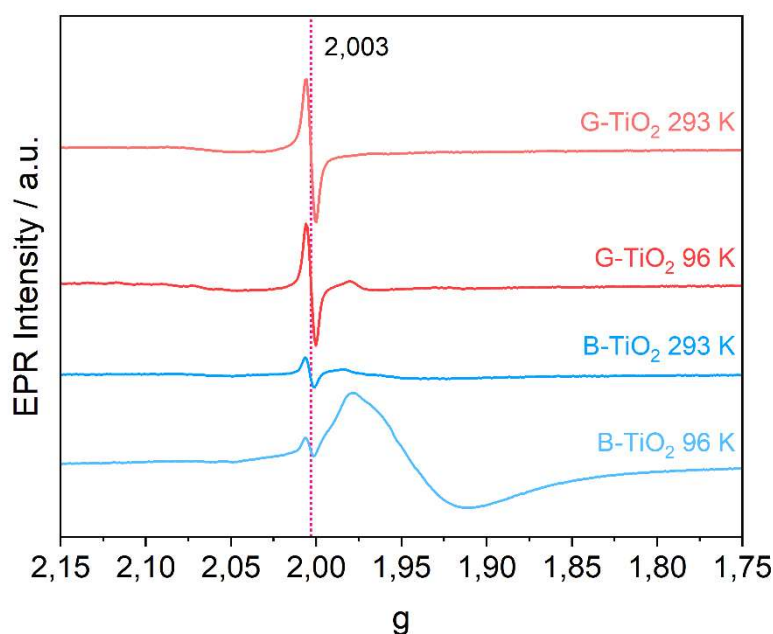


Figure 27. CW X-band EPR spectra of B- $\text{TiO}_2$  and G- $\text{TiO}_2$  nanoparticles recorded at 96 K and 293 K.

Finally, the structural changes that are introduced in TiO<sub>2</sub> framework by self-doping and thermal annealing were verified by studying Ti and O chemical environments in pristine TiO<sub>2</sub>, B-TiO<sub>2</sub> and G-TiO<sub>2</sub> samples on a particle level by scanning transmission electron microscopy - electron energy-loss spectroscopy (STEM-EELS). The STEM-EELS results for the three samples are shown in figure 28.

First, figure 28, top left shows an annular dark-field STEM (ADF-STEM) image of pristine TiO<sub>2</sub> with comparable particle size distribution to the one already discussed in figure 22, top right. To differentiate the core from the shell of the nanoparticles, STEM-EELS analysis was carried out in the Ti-L<sub>3,2</sub> and O-K edge region as shown in figure 28, top right. Analysed surface and bulk regions of pristine TiO<sub>2</sub> are enclosed by red squares in figure 28, top left. The energy-loss near-edge structure (ELNES) of TiO<sub>2</sub> in Ti-L<sub>3,2</sub> region is generally dominated by the main four white lines arising from  $2p6^3d^0 \rightarrow 2p^53d^1$  electronic transition for a tetravalent ion in an octahedral site. The core-hole spin-orbit coupling gives rise to two main features, L<sub>3</sub> and L<sub>2</sub> edges, which further split under the effect of the octahedral crystal field on the 3d states.<sup>168</sup> Further, the shoulder in the second white line in the L<sub>3</sub> edge is caused by transition from the  $2p_{3/2}$  to  $e_g$  (L<sub>3</sub>- $e_g$ ) states and reflects differences in the octahedral coordination of O around Ti in anatase and rutile, thus representing the basis for distinguishing between the two polymorphs.<sup>169</sup>

The shoulder is located at the low energy-loss side of the L<sub>3</sub> line in rutile polymorph, while in anatase it is centred at the high energy-loss end. Apparently, in the case of pristine TiO<sub>2</sub> all three measured areas correspond to the anatase polymorph. Furthermore, the very strong similarities between surface and bulk regions that are observed herein confirming good crystallinity and well-resolved edge structure in TiO<sub>2</sub>. Apart from the Ti-L<sub>3,2</sub> edge, the O-K edge shows two principal features that originate from the transition between oxygen 2p states hybridized with Ti 3d  $t_{2g}$  and  $e_g$  orbitals.<sup>168</sup> Two defined white lines in the O-K edge of sample in the bulk region and at the surface further confirm the crystalline nature of the nanoparticles in pristine TiO<sub>2</sub>.<sup>170</sup>

In B-TiO<sub>2</sub>, the ELNES of Ti-L<sub>3,2</sub> and O-K edges in the bulk region confirms that the core of the particles retain crystal structure after self-doping with Na/K alloy (fig. 28, middle right). Also, in this sample anatase and rutile particles have been detected, as indicated by the position of the L<sub>3</sub>- $e_g$  shoulder on the Ti-L<sub>3,2</sub> edge of two bulk regions (area 1 and area 3). However, the main spectral differences in B-TiO<sub>2</sub> arise from the surface region (area 2), where peaks become poorly resolved. Moreover, the changes such as low energy-loss shift of the onset of the Ti-L<sub>3,2</sub> edge, splitting of the first white line in the L<sub>3</sub> edge into two peaks, and broadening of the white lines in O-K edge could be speculated to occur. However, to approve these secondary changes rather high-resolution EELS analysis would be required. Nonetheless, STEM-EELS analysis suggests that structure in surface region of B-TiO<sub>2</sub> is altered due to presence of Ti<sup>3+</sup> in TiO<sub>2</sub>, which induce

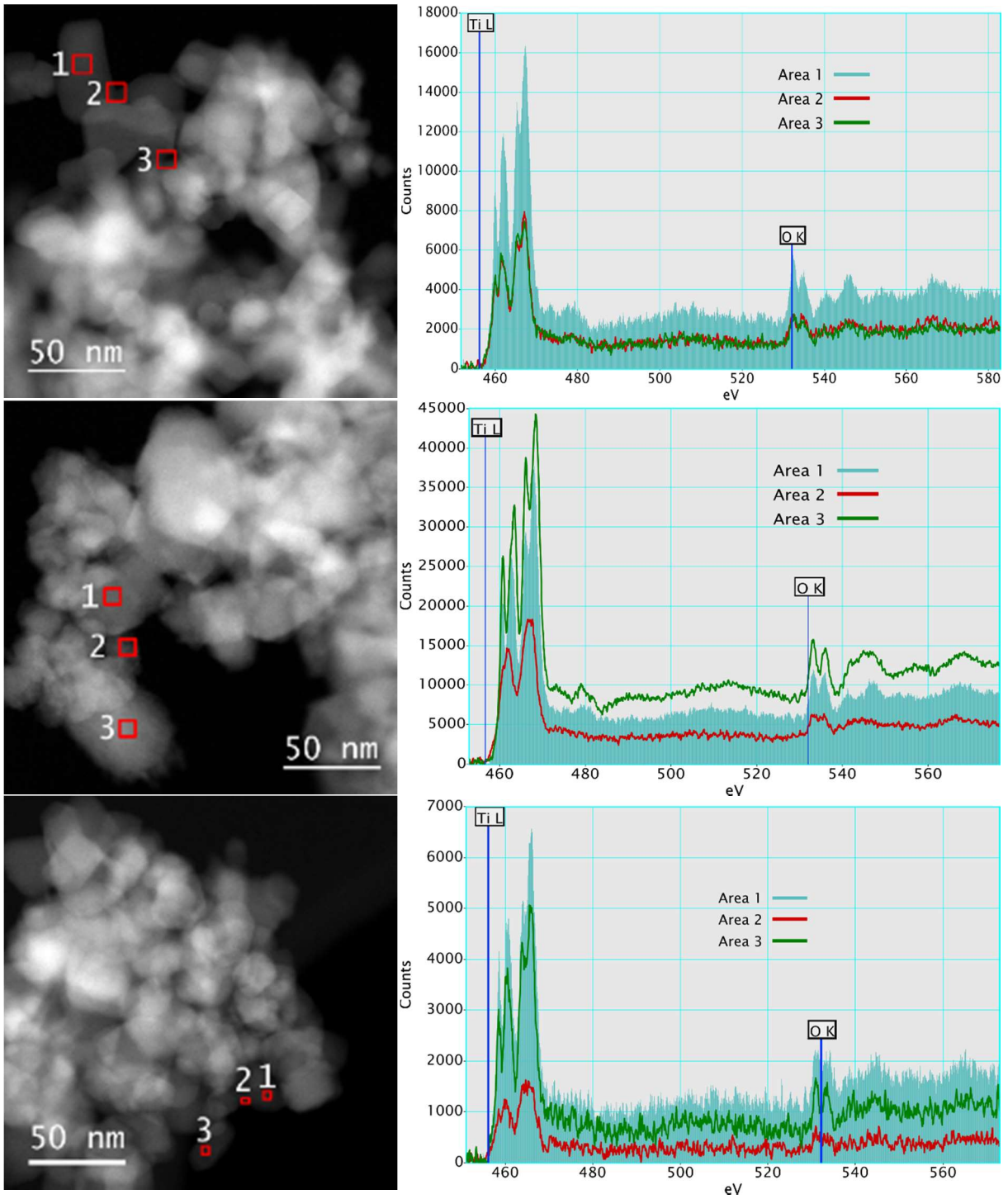


Figure 28. ADF-STEM images (left) and EELS spectra in the Ti-L<sub>3,2</sub> and O-K edge from surface and bulk regions enclosed by red squares in ADF-STEM images of pristine TiO<sub>2</sub> (top), B-TiO<sub>2</sub> (middle) and G-TiO<sub>2</sub> (bottom) samples.

variations in chemical environment around  $\text{Ti}^{4+}$  ion and eventually lead to the more complex ELNES structure.<sup>170</sup>

The STEM-EELS analysis of G- $\text{TiO}_2$  shows that core of the particles has the anatase structure, thus confirming that temperature during thermal annealing do not affect the particle core. Conversely to the core of the particles, the thermal annealing shows an impact on the surface region in G- $\text{TiO}_2$ . For example, when compared with B- $\text{TiO}_2$ , it can be noticed that the edge onsets of surface and bulk Ti after thermal annealing once again become well aligned. Furthermore, it is found that the first white line in the  $L_3$  edge reappears. However, the resolution is still lower than that of  $\text{TiO}_2$ , indicating that structure in G- $\text{TiO}_2$  sample is only partially recovered. Taken together, STEM-EELS results substantiate the structure reordering in G- $\text{TiO}_2$  after thermal annealing accompanied by  $\text{Ti}^{3+}$  ion reoxidation to the  $\text{Ti}^{4+}$  state.

Following the unique identification of the core and the shell in B- $\text{TiO}_2$  and G- $\text{TiO}_2$ , fine edge structures were used as a model in the multilinear least-square (MLLS) fitting. Fitting of ADF-STEM images allows computing of overlay as well as single color phase distribution maps of the B- $\text{TiO}_2$  and G- $\text{TiO}_2$  samples (fig. 29). The overlay image of B-

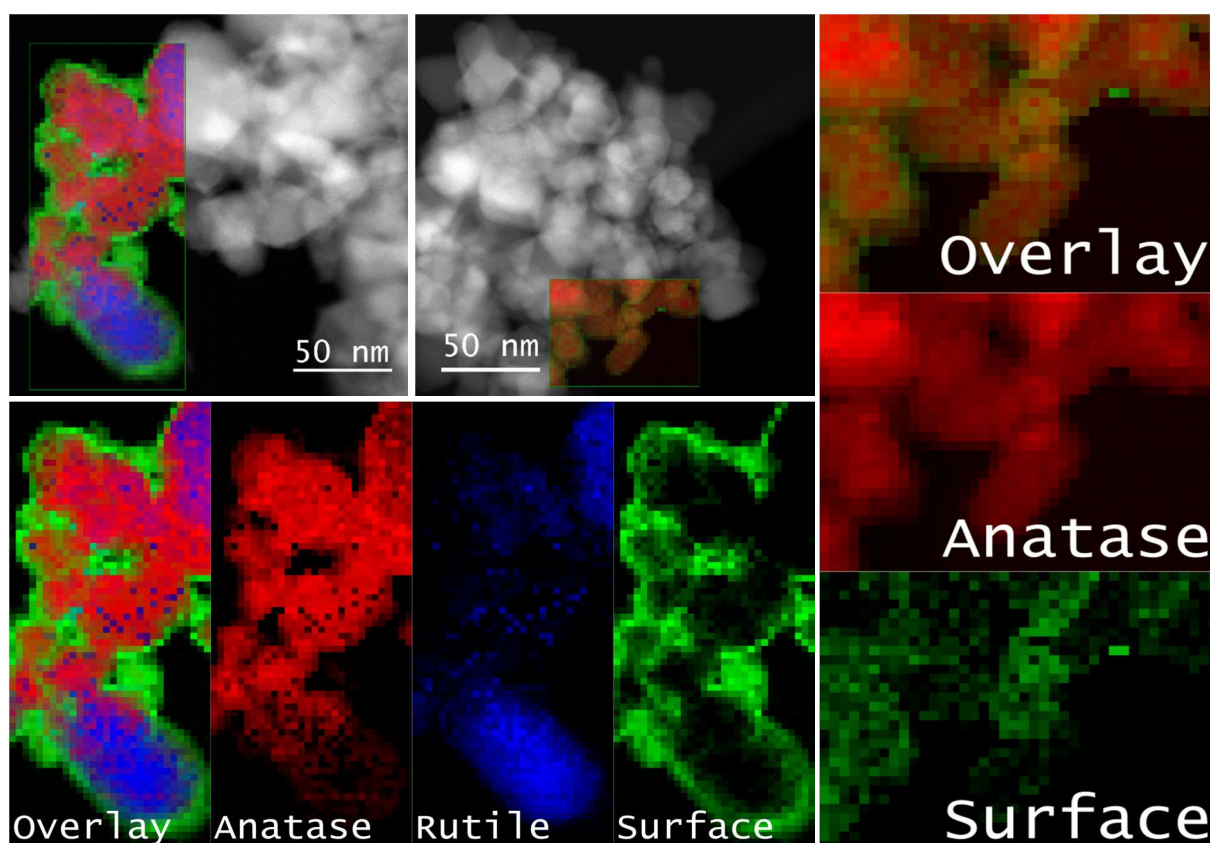


Figure 29. Overlaid ADF-STEM images of B- $\text{TiO}_2$  (top left) and G- $\text{TiO}_2$  (top middle) and overlay and single-color phase distribution maps derived from EELS fine structures by MLLS fitting for B- $\text{TiO}_2$  (bottom) and G- $\text{TiO}_2$  (right) samples.

TiO<sub>2</sub> (fig. 29, bottom) shows that a thick surface layer surrounds anatase and rutile nanoparticles. Such distribution of a disordered layer in B-TiO<sub>2</sub> is a bit controversial concerning the previous characterization, particularly XRD, which indicated that disorder is introduced solely in the anatase phase after the reaction with Na/K alloy. The reason for this discrepancy may arise from the fact that rutile particles are embedded into anatase as indicated by single phase distribution map of anatase, where smaller anatase particles encircle big rutile particle (fig. 29, bottom). Therefore, the surface signal most likely arises from modified anatase phase in B-TiO<sub>2</sub>. To fully clarify the issue from the EELS standpoint, STEM-EELS analysis of isolated rutile particle would be highly desired.

In G-TiO<sub>2</sub>, on the other hand, the surface layer loses its compactness and shrinks confirming the previous conclusion that the disordered layer restructures upon thermal annealing due to Na deintercalation and Ti<sup>3+</sup> ion reoxidation to Ti<sup>4+</sup> ion (fig. 29, right).

### 3.5 Structural model of self-doped TiO<sub>2</sub>

The characterization that has been done with TiO<sub>2</sub> materials aimed to provide information on structural changes within the TiO<sub>2</sub> framework after it being self-doped in the reaction with Na/K alloy. The questions such as Na intercalation as well as formation and stability of Ti<sup>3+</sup> ions in the TiO<sub>2</sub> framework were of particular interest, and their influence on catalytically relevant features of TiO<sub>2</sub> material like light harvesting ability and surface composition. Based on XRD, TEM, EPR, XPS and STEM-EELS measurements a triple-hybrid TiO<sub>2</sub>@Ti<sup>3+</sup>/TiO<sub>2</sub>@TiO<sub>2</sub> structural model of B-TiO<sub>2</sub> is

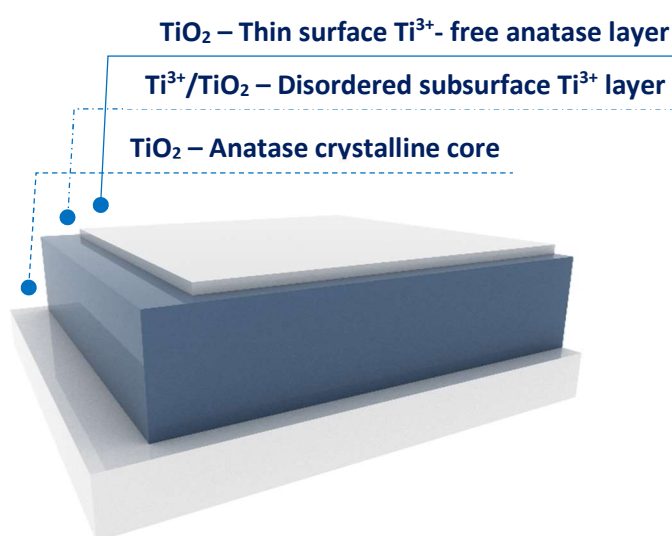


Figure 30. Triple hybrid TiO<sub>2</sub>@Ti<sup>3+</sup>/TiO<sub>2</sub>@TiO<sub>2</sub> structural model of B-TiO<sub>2</sub>



proposed (figure 30). It should be, however, mentioned that this model applies only to anatase particles in B-TiO<sub>2</sub>. The first structural segment in the model is an unreacted anatase crystalline core. The reaction of TiO<sub>2</sub> with Na/K alloy is a diffusion-based reaction; therefore, it is limited by the rate of transport of Na through the TiO<sub>2</sub> matrix. Generally, the smaller the anatase particle, the bigger the extent of modification with Na/K alloy. The second structural segment is a disordered layer that surrounds the anatase crystalline core. The intercalated Na accumulates here and reduces Ti<sup>4+</sup> ion to Ti<sup>3+</sup> ion. The disordered layer determines the light harvesting ability of B-TiO<sub>2</sub>. The third and outermost segment in B-TiO<sub>2</sub> structure consists of a thin anatase layer composed of Ti<sup>4+</sup> ions and is free of intercalated Na. Therefore, according to the TiO<sub>2</sub>@Ti<sup>3+</sup>/TiO<sub>2</sub>@TiO<sub>2</sub> structural model the advantage of B-TiO<sub>2</sub> in solar H<sub>2</sub> production comparing with pristine TiO<sub>2</sub> may arise from a wider range of sunlight that B-TiO<sub>2</sub> can capture to generate charge carriers.

## 3.6 Photocatalytic activity of self-doped TiO<sub>2</sub>

### 3.6.1 H<sub>2</sub> production under 1.5 AM solar simulated light

The catalytic performance of the B-TiO<sub>2</sub> and G-TiO<sub>2</sub>/AC samples was investigated in the photocatalytic H<sub>2</sub> production from a water/methanol mixture under AM 1.5 simulated solar light and results are shown in figure 31. The catalytic performance of the B-TiO<sub>2</sub> and G-TiO<sub>2</sub>/AC catalysts was benchmarked with TiO<sub>2</sub> P25 and in all catalysts nominally 0.5 wt% Pt co-catalyst was deposited by in situ photoreduction of H<sub>2</sub>PtCl<sub>6</sub>. Even structurally very similar, G-TiO<sub>2</sub>/AC was chosen over G-TiO<sub>2</sub> catalyst for the H<sub>2</sub> production test because the surface of the latter contains deintercalated Na and loosely bound carbon impurities that can hinder deposition of the co-catalyst and adsorption of a reactant, and thus hamper the H<sub>2</sub> production on the G-TiO<sub>2</sub> catalyst. At time 0 hours the light illumination was switched on, where in situ photodeposition of Pt co-catalyst takes place in parallel with the photocatalytic H<sub>2</sub> production. The catalysts were tested for 2.5 h and H<sub>2</sub> production rate in μmolg<sup>-1</sup>h<sup>-1</sup> was determined at the end of the test.

Photocatalytic results for the TiO<sub>2</sub> samples indicate that under 1.5 AM illumination the TiO<sub>2</sub> P25 benchmark exhibits the highest H<sub>2</sub> production rate of 400 μmolg<sup>-1</sup>h<sup>-1</sup>, followed by G-TiO<sub>2</sub>/AC and B-TiO<sub>2</sub> with the rates of 190 and 44 μmolg<sup>-1</sup>h<sup>-1</sup>, respectively. In TiO<sub>2</sub> P25 the photocatalytic activity steadily increases during the test, while the H<sub>2</sub> production in B-TiO<sub>2</sub> and G-TiO<sub>2</sub>/AC catalysts is stable, especially after the first 30 minutes on. It should be mentioned that TiO<sub>2</sub> samples showed reverse order in photocatalytic activity when compared with their light harvesting ability. This means that B-TiO<sub>2</sub>, the material with the most color centers performs the least efficient. No formic acid is detected after photocatalytic tests with TiO<sub>2</sub> samples.

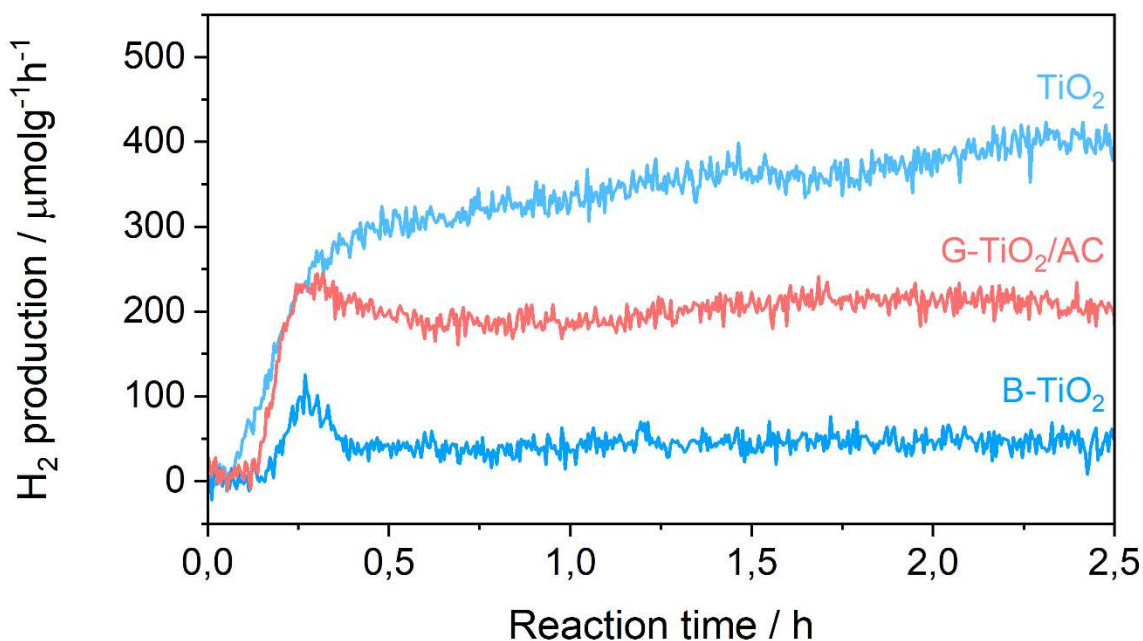


Figure 31. Photocatalytic H<sub>2</sub> production on B-TiO<sub>2</sub>, G-TiO<sub>2</sub>/AC and TiO<sub>2</sub> P25 catalysts

### 3.6.2 Effect of Ti<sup>3+</sup> ions on solar H<sub>2</sub> production of self-doped TiO<sub>2</sub>

To check if the concentration or the nature of color centers play a role in photocatalytic performance of B-TiO<sub>2</sub>, a H<sub>2</sub> production test was run with the B-TiO<sub>2</sub>\_0.05 catalyst which has the lowest amount of centers that can still turn the color of TiO<sub>2</sub> to blue. The test was performed with B-TiO<sub>2</sub>\_0.05 and TiO<sub>2</sub> P25 catalysts under AM 1.5 illumination. In this experiment a pyrex glass reactor was used instead of a top-irradiated reactor with flat quartz window and results are shown in figure 32. The mass-specific activity of B-TiO<sub>2</sub>\_0.05 and TiO<sub>2</sub> P25 after 2.5 h of the reaction was 718 and 890 μmol g<sup>-1</sup>, respectively, which makes a decrease in the activity of B-TiO<sub>2</sub>\_0.05 of around 20 % comparing with TiO<sub>2</sub> P25 benchmark. Please note that in these experiments a pressure increase was not accounted for. Thus, these results indicate that the amount of Ti<sup>3+</sup> centers plays a role in the deactivation of B-TiO<sub>2</sub> samples in the way that Ti<sup>3+</sup> promotes TiO<sub>2</sub> deactivation and this effect is increasing with the of amount of Ti<sup>3+</sup> ions.

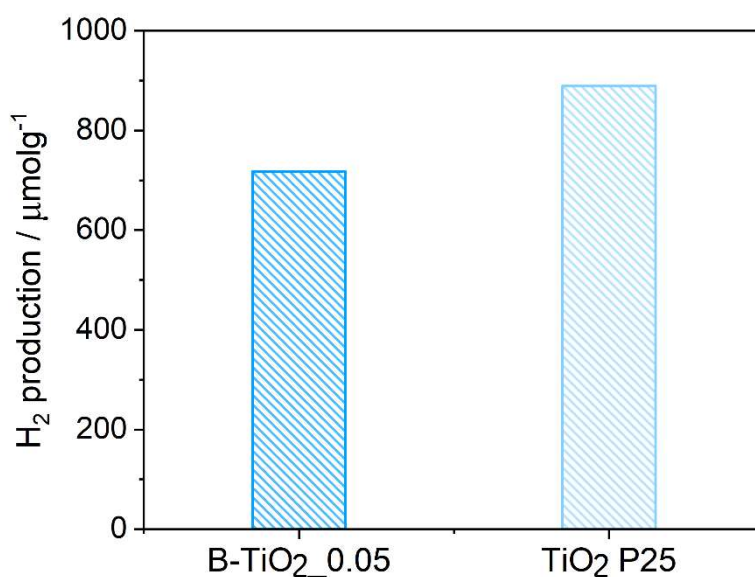


Figure 32. Photocatalytic H<sub>2</sub> production on B-TiO<sub>2</sub>, G-TiO<sub>2</sub>/AC and TiO<sub>2</sub> P25 catalysts

The hindering effect of Ti<sup>3+</sup> ions in self-doped TiO<sub>2</sub> on the photocatalytic H<sub>2</sub> production is more likely related to the Ti<sup>3+</sup> ion nature and spatial distribution within the TiO<sub>2</sub> framework. On one hand, DRS data have shown that in-band Ti<sup>3+</sup> level can act dually, as donor and acceptor level. Juggling on this, it can be speculated if this level decreases or increases charge recombination. On the other hand, combination of XPS and EPR analysis have revealed that Ti<sup>3+</sup> ions are preferentially located in the subsurface/bulk region of TiO<sub>2</sub>. Generally, bulk defects in TiO<sub>2</sub> are considered to introduce new charge carrier trapping and recombination centers.<sup>91</sup> These centers would decrease the mobility and diffusibility of the photoexcited charge carriers, making the energy transfer less efficient, thus degrading the performance of the catalyst. It turned out that even though the B-TiO<sub>2</sub> is the better light harvester and most likely produces more charge carriers, due to the poor charge carrier dynamics less of them would reach the surface of the catalyst, where redox reactions take place. This is corroborated by the photocatalytic results of G-TiO<sub>2</sub>\_AC, the material virtually free from Ti<sup>3+</sup> ions, which exhibited better photocatalytic activity by a factor more than 4 than that of B-TiO<sub>2</sub>. Therefore, the choice of type of defect and their distribution in the TiO<sub>2</sub> framework are imperatives for the preparation of efficient doped-TiO<sub>2</sub> photocatalysts for solar applications.

### 3.7 Conclusions

Self-doped TiO<sub>2</sub> were synthesized in the reaction of TiO<sub>2</sub> with Na/K alloy and self-doped blue TiO<sub>2</sub> powders show outstanding color stability under storing at ambient conditions. The structural characterization reveals that self-doped TiO<sub>2</sub> adopt a hybrid TiO<sub>2</sub>@Ti<sup>3+</sup>/TiO<sub>2</sub>@TiO<sub>2</sub>

structure with disordered layer embedded between TiO<sub>2</sub> crystalline core and TiO<sub>2</sub> overlayer. The Ti<sup>3+</sup> ions are preferentially formed in the disordered layer and their amount correlates with the amount of added Na/K alloy i.e., an extent of Na intercalation into TiO<sub>2</sub> framework. Further, intercalated Na seems to be crucial for long-term stabilization of Ti<sup>3+</sup> ions. The Ti<sup>3+</sup> ions unlock visible and near infrared light absorption in self-doped TiO<sub>2</sub> by introduction of in-band electronic states 1.3 eV below the conduction band. Platinized B-TiO<sub>2</sub> (0.5 wt% Pt) achieves a H<sub>2</sub> production rate of 44 μmolg<sup>-1</sup>h<sup>-1</sup> from methanol/water mixture under solar simulated light (AM 1.5), by factor 9 less than that of TiO<sub>2</sub> P25 despite the fact that solar light absorption has been substantially increased in B-TiO<sub>2</sub>. After the Ti<sup>3+</sup> ions are removed from the B-TiO<sub>2</sub> structure, the activity of G-TiO<sub>2</sub>/AC catalyst is enhanced by more than 4 times. When present, Ti<sup>3+</sup> deactivates self-doped TiO<sub>2</sub> catalysts and deactivation is an increasing function of the Ti<sup>3+</sup> amount. Therefore, the nature and spatial distribution of Ti<sup>3+</sup> ions within the TiO<sub>2</sub> framework are primary determinants of H<sub>2</sub> production in self-doped TiO<sub>2</sub>. The Ti<sup>3+</sup> ions formed in the disordered layer increases the bulk defect density in TiO<sub>2</sub>, which hamper charge carrier dynamics and lead to the sluggish H<sub>2</sub> production. The subsurface transformation is a common challenge in diffusion-based post-formation doping routes and has been proven challenging in the case of TiO<sub>2</sub> self-doping with Na/K alloy as well.

## 4. Size effect in rutile structures on photocatalytic H<sub>2</sub> production under solar light

### 4.1 Synthesis of rutile needles

TiO<sub>2</sub> rutile nanoneedles were synthesized by hydrolysis of titania-tetraisopropoxide (TTIP) under acidic conditions at room temperature for 4 days (fig. 33). After workup of the reaction and drying at elevated temperatures (120 or 200 °C), white nanopowders of rutile needles were obtained. The reaction conditions such as temperature, Ti-precursor, pH value or ion concentration in the reaction medium can determine crystal structure and morphology of resulting TiO<sub>2</sub> materials. Hence, in this chapter main factors that influence the synthesis of rutile needles will be discussed.

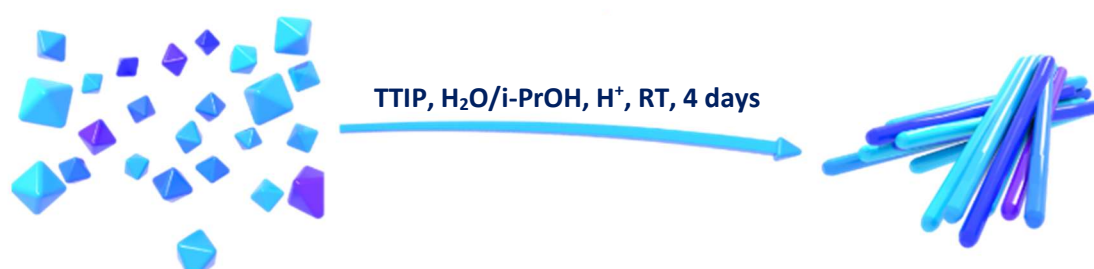


Figure 33. Schematic illustration of rutile needle synthesis

Temperature during synthesis can impact the synthesis in several ways. First, low temperature is required to keep the TiO<sub>2</sub> nucleation rate low, which allows formation of pure phase rutile crystal structures.<sup>171</sup> At temperature as low as 80 °C the anatase crystal phase will start to crystallize leading to mixed phase TiO<sub>2</sub> materials. Second, low temperature synthesis of crystalline TiO<sub>2</sub> allows formation of nanosized rutile crystals due to the slow crystal growth, which is in sharp contrast with high temperature synthesis where sub-micro to microcrystals are typically obtained.<sup>172</sup> Third, low temperature will retard excessive development of parallel layers terminated with (110) facets, the key for efficient photocatalysis with rutile polymorph. The role of (110) facets of rutile catalysts on H<sub>2</sub> production under solar light will be discussed in detail in the following sections.

Beside temperature, the choice of the type of Ti-precursor plays a role mainly in determining the phase composition of TiO<sub>2</sub>. Here, TTIP is used as Ti-precursor. Generally, other fast hydrolyzing Ti-compounds such as TiCl<sub>4</sub> or Ti(SO<sub>4</sub>)<sub>2</sub> are suitable precursors for obtaining crystalline oxide at low temperatures.<sup>133, 171</sup> In TTIP electronegative isopropoxy groups make the metal prone to nucleophilic attack of water. The reaction between alkoxide and water, in

fact, can be considered as a two-step process: a hydrolysis reaction and a condensation<sup>173</sup>. Among two processes hydrolysis occurs first and results in the formation of Ti-OH bonds. Furthermore,  $Ti^{4+}$  ions increase their coordination from 4-fold tetrahedral in TTIP to 6-fold octahedral in  $TiO_2$  by using their vacant d-orbitals to accept oxygen lone pairs from nucleophilic OH ligands by coordination expansion.<sup>173</sup> Then, the follow up condensation occurs along with elimination of water molecules. The  $TiO_2$  formation mechanism can be explained on the basis of a partial charge model. According to the model, solid polymorphs form by condensation of octahedral  $[Ti(OH)_x(H_2O)_y]^{n+}$  units in the precursor solution and the relative amount of each phase varies with the acidity of the aqueous solution since the pH determines the form of the prevalent octahedral species. Thus, for example, high pH causes an increase in the number of OH groups coordinated to Ti(IV) centers. Consequently, the probability for edge-shared bonding is high, favoring the anatase phase where  $[TiO_6]$  octahedrons share 4 edges with their neighbors. Conversely, at low pH, the number of OH ligands are lower and crystallization of rutile phase is preferred since the  $[TiO_6]$  octahedron in rutile phase shares only 2 edges.

Further, the decrease in the pH value of the aqueous solution promotes dissolution-precipitation mechanism in  $TiO_2$  synthesis. Under such conditions, dissolution of precipitated  $TiO_2$  increases substantially, which has a primary effect on the rate of  $TiO_2$  crystallization. Also, higher acidity can help in keeping the  $TiO_2$  crystals small.

Concentration of ions in the solution has been also shown to influence the composition of octahedral Ti-units. The speciation of titanium hydroxochloro complexes upon increasing the concentration of chloride ions in acidic media at elevated ionic strength have resulted in formation of  $[Ti(OH)_2(H_2O)_4]^{2+}$ ,  $[Ti(OH)_2Cl(H_2O)_3]^+$ ,  $[Ti(OH)_2Cl_2(OH)_2]^0$ ,  $[Ti(OH)_2Cl_3(H_2O)_2]^-$ , and  $[Ti(OH)_2Cl_4]^{2-}$  complexes.<sup>174, 175, 176</sup> For example, by varying the Ti : Cl ratio in aqueous solution with HCl and NaCl during  $TiO_2$  synthesis, two hydroxochloro complexes  $[Ti(OH)_2Cl_3(H_2O)_2]^-$  and  $[Ti(OH)_2Cl_4]^{2-}$  were dominant in the solution, which promoted crystallization of brookite and rutile  $TiO_2$ , respectively.<sup>177</sup> In general, the probability that the rutile phase will crystallize increases with increasing symmetry of octahedral Ti-units as in case of  $[Ti(OH)_2Cl_4]^{2-}$ .<sup>178</sup> Further, the strong ion effect has been confirmed even in the case of counter-ion ( $SO_4^{2-}$ ) when  $Ti(SO_4)_2$  is employed as Ti-precursor.<sup>171</sup> For instance, when the NaOH :  $Ti(SO_4)_2$  ratio is above 3, the rutile phase is formed. Otherwise, the anatase phase crystallizes along the rutile producing mixed-phase  $TiO_2$  precipitates. Also, for a NaOH :  $Ti(SO_4)_2$  ratio below 3 residual  $SO_4^{2-}$  ions were detected in the  $TiO_2$  precipitate, which apparently facilitate crystallization of anatase phase.

In  $TiO_2$ , the octahedra agglomerate through corner and edge sharing during the condensation reaction. The condensation reaction itself is comprised of nucleation and crystal growth. The nucleation precedes the crystal growth and determines the crystal phase which will be grown. The  $TiO_2$  nucleus is a unit of three spatially distributed octahedra.<sup>137</sup> Initially, two octahedra undergo a condensation reaction and join at a corner. Upon further condensation, the two will become joined along an edge. When this happens, the cation-cation repulsion causes the

centers of the two octahedra to move apart, and the shared edge becomes shorter.<sup>179</sup> The position of the third octahedron determines whether a rutile or an anatase nucleus is formed. The third octahedron initially joins the two-octahedron cluster at a corner. Then two options exist: to bond such that a right-angle is formed (basic structural motif of anatase, fig. 34, top left) or straight angle (structural motif of rutile, fig.34, bottom left). The straight angle configuration is, however, thermodynamically favorable since it allows largest cation-cation distances. Nevertheless, the configurations that are possible with three joined octahedra statistically favor anatase. Hence, faster reaction rate favors anatase formation. After nucleation, the rutile structure continues to grow through edge and corner sharing (fig. 34, right). Extension of a rutile nucleus by further octahedra condensation forms linear 1D chains along the crystal c-axis. Chains then link in crystal ab plane by sharing corner oxygen atoms, initially forming 2D structures while upon further linking the series of alternate chains eventually form 3D rutile TiO<sub>2</sub> framework. Therefore, the reaction conditions for synthesis of rutile TiO<sub>2</sub> should be chosen in the way to prevent fast crystal growth and incorporation of impurities into the structure which would promote formation of metastable anatase phase. Also, promotion of dissolution of the TiO<sub>2</sub> precipitate during preparation will be beneficial for the synthesis of small rutile structures.

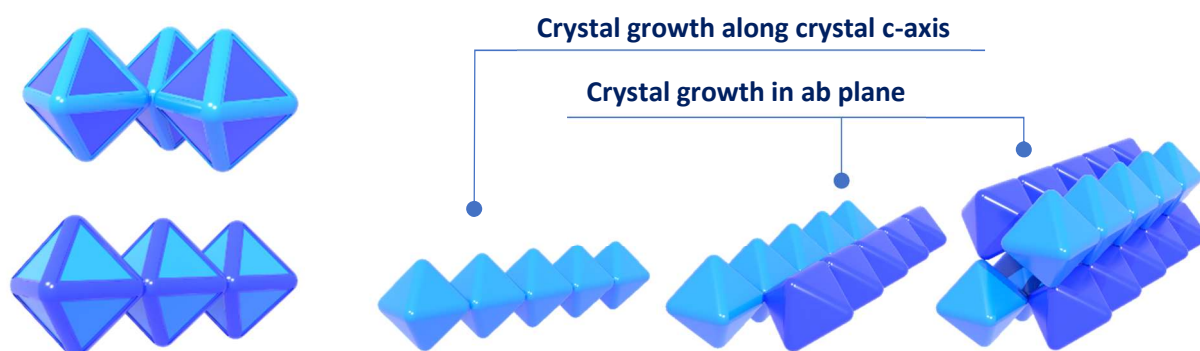


Figure 34. Nucleus of anatase (top left) and rutile (bottom left) TiO<sub>2</sub> and crystal growth of rutile polymorph by edge and corner sharing (right)

## 4.2 Morphology and crystal structure of rutile needles

The morphology of the synthesized rutile nanoneedle samples were studied by TEM analysis. The two rutile needle morphologies were compared with rutile TiO<sub>2</sub> and the bright-field TEM images are shown in figure 35. Low magnification TEM image of rTiO<sub>2</sub>-needle<sub>120</sub> (fig. 35, top left) depicts stubbed needle-shape secondary particles about 200 nm long and upwards of 30 nm wide. Samples rTiO<sub>2</sub>-needles<sub>200</sub> and rutile TiO<sub>2</sub> (nanoparticulate commercial rutile TiO<sub>2</sub>

used as benchmark) (fig. 35, middle and bottom left, respectively) show less uniform morphology comparing with rTiO<sub>2</sub>-needles<sub>120</sub>. For example, in rTiO<sub>2</sub>-needles<sub>200</sub> nanoplates around 100 nm long and 20 nm wide can be observed. Also, TEM analysis showed that rutile TiO<sub>2</sub> has a wide size distribution of nearly spherical to oblong nanoparticles (fig. 35, bottom right).

High magnification TEM image of rTiO<sub>2</sub>-needles<sub>120</sub> (fig. 35, top right) reveals that needle-like precipitates are formed by the aggregation of the primary particles which, as indicated by TEM, are about 5 nm in width. The length of the particles shows more variations, typically they are 10-20 nm long. Such an ordering mechanism was first proposed in the gelation of clays,<sup>180</sup> and has been extended to explain the formation and growth of transition metal oxides, such as V<sub>2</sub>O<sub>5</sub> and ZrO<sub>2</sub>.<sup>181</sup>

The factors that have been proposed to explain ordered aggregation are non-uniform surface charge distribution and anisotropy of the hydration layer. These forces could cause the aggregation to proceed such that the overall energy is minimized. Aggregation therefore occurs preferentially along the c-axis as it is the direction of high surface energy for the rutile structure.<sup>182</sup> However, the aggregation process never allows perfect low energy (110) facets to develop. Thus, the needles do not develop long parallel sides as they occur in the slow natural mineral formation of rutile. Instead, the needles develop a compromised oblong shape. In rTiO<sub>2</sub>-needles<sub>200</sub> primary particles are not observed, indicating that thermally induced coalescence of primary particles takes place at 200 °C (fig. 35, middle right). Further structural analysis cannot be done with present data, but high-resolution TEM analysis would be required.

The crystal structure of the rutile samples was studied by XRD in the 10 - 80 2 Theta degree range and results are shown in figure 36. The diffraction patterns of three samples contain diffraction peaks indexed to the tetragonal rutile crystal phase (icdd\_pdf\_00-021-1276). Additionally, in the pattern of rutile TiO<sub>2</sub> two weak signals at 65.5 and 72.4 2 Theta degrees correspond to the 221 and 311 Bragg peaks of tetragonal rutile structure. The 221 and 311 peaks have intensity of 2 % relative to the 110 peak in rutile TiO<sub>2</sub>. Hence, presumably due to the lower intensity of the signals these peaks were not detected in the patterns of either rTiO<sub>2</sub>-needles<sub>120</sub> or rTiO<sub>2</sub>-needles<sub>200</sub>. Beside rutile diffraction peaks, in the rutile TiO<sub>2</sub> pattern a weak feature centered at 25.4 2 Theta degree is detected and can be ascribed to the anatase (icdd\_pdf\_01-076-3177) crystal phase. This result implies that the commercial nanopowder was not phase pure rutile TiO<sub>2</sub> but contains traces of the anatase crystal phase.

As already noted, the signal intensity and shape in rutile needle samples are weak and broad, deviating from strong and sharp signals in rutile TiO<sub>2</sub>. The ascending order of signal breadth in rutile samples is as follows: rutile TiO<sub>2</sub>, rTiO<sub>2</sub>-needles<sub>200</sub>, rTiO<sub>2</sub>-needles<sub>120</sub>. Generally, in



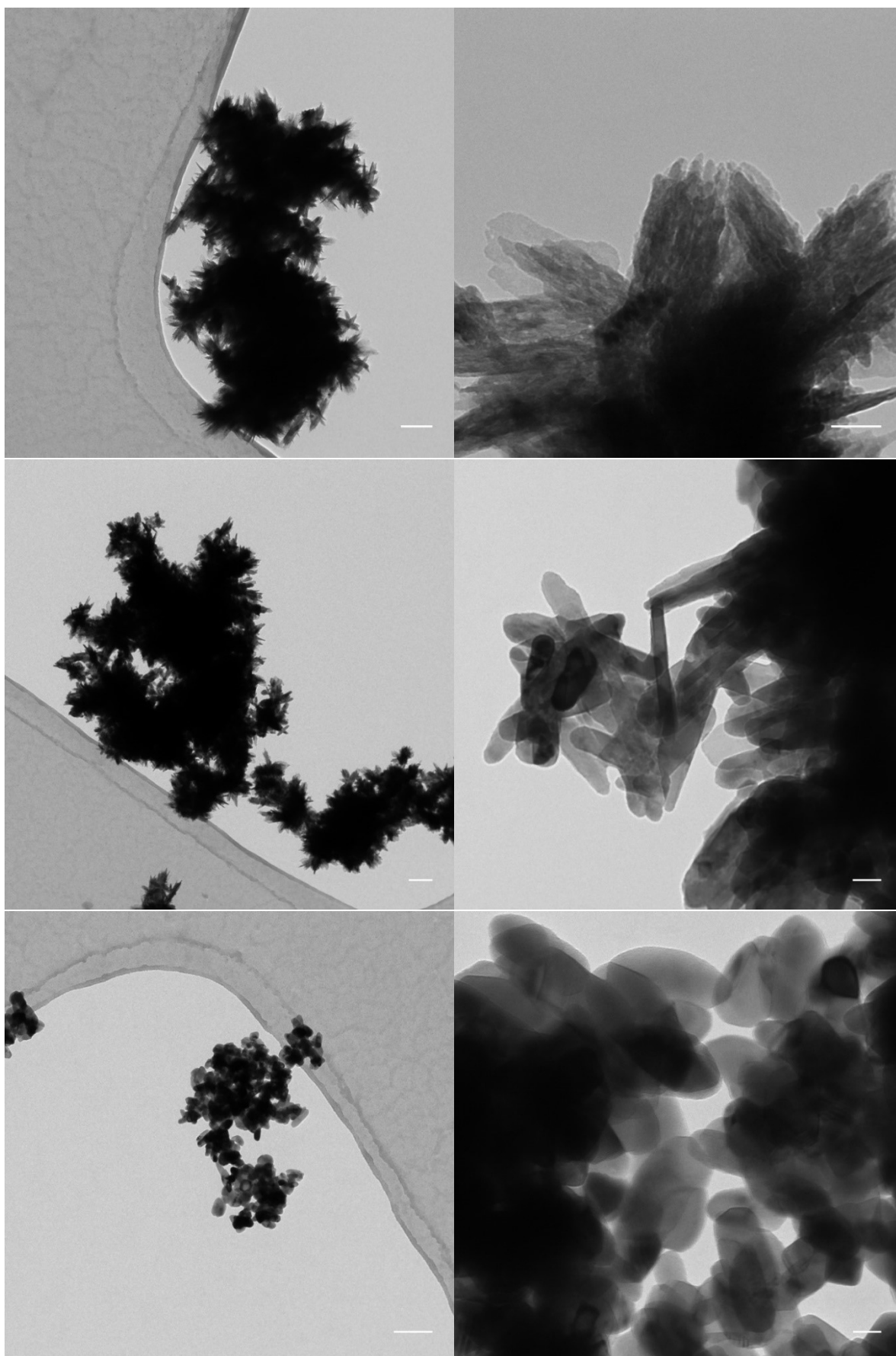


Figure 35. TEM micrographs of rTiO<sub>2</sub>-needles<sub>120</sub> sample (top left and right), rTiO<sub>2</sub>-needles<sub>200</sub> (middle left and right), rutile TiO<sub>2</sub> (bottom left and right). Scale bar is 200 nm (left) and 20 nm (right)

the two needle patterns, the baseline of patterns is comparable with that of the rutile  $\text{TiO}_2$  and no amorphous phase is observed. Alternatively, the amorphous  $\text{TiO}_2$  phase can be transformed into anatase during the work up of the reaction. The minimal temperature that will allow transformation of amorphous  $\text{TiO}_2$  into crystalline anatase  $\text{TiO}_2$  is  $80\text{ }^\circ\text{C}$ , a temperature well below either  $120$  or  $200\text{ }^\circ\text{C}$  which were used in the synthesis of  $\text{rTiO}_2$ -needles<sub>120</sub> and  $\text{rTiO}_2$ -needles<sub>200</sub>, respectively.<sup>171</sup> Even metastable, the anatase phase that is once formed does not spontaneously convert to rutile at temperatures below the anatase to rutile transition temperature. Therefore, if present, patterns of rutile needle samples must contain the anatase diffraction peaks. Yet again, diffraction peaks of the anatase phase are not observed in the  $\text{rTiO}_2$ -needles<sub>120</sub> and  $\text{rTiO}_2$ -needles<sub>200</sub> diffraction patterns. Thus, based on XRD data it can be concluded that rutile needles are synthesized as pure phase rutile crystalline  $\text{TiO}_2$ .

To study the impact of the crystallite size on the broadening of XRD signal in rutile samples, the crystallite size of (110) and (002) Bragg peaks were deduced from XRD data according to the Scherrer equation. The two peaks were chosen because they allow studying crystal growth in two principal growth directions, in ab plane (110) and along the crystal c-axis (002). Interplanar, d-spacing of (110) and (002) Bragg peaks were calculated by the Bragg equation and the data on crystallite size and d-spacing are summarized in Table 4.

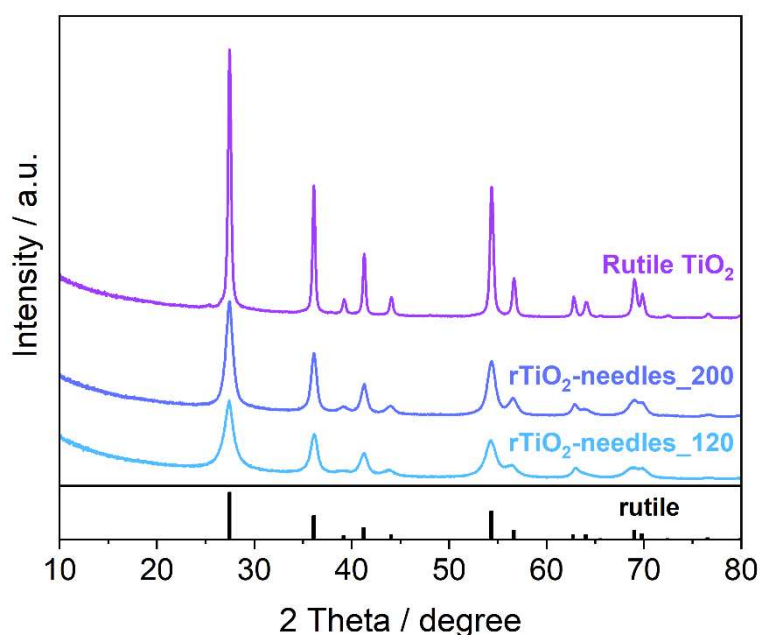


Figure 36. XRD patterns of rutile  $\text{TiO}_2$ ,  $\text{rTiO}_2$ -needle<sub>120</sub>,  $\text{rTiO}_2$ -needle<sub>200</sub> samples

First, the crystallite size of the three rutile samples varies from sample to sample, where the biggest crystallites are confirmed in rutile  $\text{TiO}_2$ . The size in ab plane and c-axis are  $23.6$  and  $27.0\text{ nm}$ . In the needle samples, in general, smaller average crystallite sizes are observed, which depend on the processing temperature of the samples and the crystal direction. In

rTiO<sub>2</sub>-needle\_120 and rTiO<sub>2</sub>-needle\_200 crystallite sizes in ab plane are 6.9 and 9.7 nm, respectively, by factor 3.4 and 2.4 smaller in comparison with rutile TiO<sub>2</sub>, indicating that excessive crystal growth in ab plane at temperatures up to 200 °C does not occur in rutile needles. Along c-axis sizes are 12.7 and 25.9 nm for rTiO<sub>2</sub>-needle\_120 and rTiO<sub>2</sub>-needle\_200, respectively, revealing that crystallites double in length by increase in temperature from 120 to 200 °C. Clearly, the thermally induced coalescence of crystallites is more pronounced along c-axis than in ab plane. The coalescence of crystallites in c-direction, could be explained by reduction of surface energy. At this point it should be stressed that small grains in rTiO<sub>2</sub>-needle\_120 sample do not develop well-defined facets, however the model rutile crystal that consists of tetragonal prism terminated by four lateral (110) facets and two pyramidal caps consisted of four (111) facets each could be a good approximation for further discussion<sup>47</sup>. Generally, (110) facet is the most thermodynamically stable facet in rutile TiO<sub>2</sub> having the lowest surface energy of 15.6 meV / (a.u.<sup>2</sup>).<sup>48</sup> Here, fivefold coordinated Ti<sub>5c</sub> and sixfold coordinated Ti<sub>6c</sub> atoms are bonding with threefold coordinated O<sub>3c</sub> and twofold coordinated O<sub>2c</sub> atoms in the surface plane, leading to the smallest unsaturation density, i.e. the lowest number of the broken bonds per nm<sup>2</sup> of the surface for all facets in rutile TiO<sub>2</sub>.<sup>28, 49, 183</sup> Conversely, (111) facets are considered to be high energy facets.<sup>150</sup> In fact, it has been calculated that the surface energy of the (111) surface is four times larger than that of the (110) surface due to more broken bonds at (111) surfaces (Ti<sub>4c</sub>, Ti<sub>5c</sub>, O<sub>2c</sub>).<sup>184</sup> To stabilize in the solution, such high energy facets in rutile TiO<sub>2</sub> would dissociatively adsorb water molecules, by which increase in number of surface -OH groups and surface hydration occurs.<sup>40 185 186</sup> Thus, the thick hydration layer would keep the grains separate and stabilize small rutile nanoparticles. However, with surface dehydration that occurs at 200 °C, the surface hydration layer shrinks and TiO<sub>2</sub> particles come closer to one another. Therefore, to reduce surface energy at high temperatures, the rutile needle system strives to decrease the amount of exposed (111) facets by aggregation, which induces crystal growth preferentially along c-axis.

At the end, the d-spacing of (110) and (002) Bragg peaks are compared for the three rutile samples. All samples show a 0.325 nm and 0.148 nm d-spacing of (110) and (002) Bragg peaks, suggesting that the rutile crystal structure regularly grows in rTiO<sub>2</sub>-needles\_120 and rTiO<sub>2</sub>-needles\_200 samples. These results imply that bulk doping i.e. incorporation of NO<sub>3</sub><sup>-</sup> ions into TiO<sub>2</sub> structure did not occur to a noticeable extent in the rutile needle samples, which is consistent with the growing mechanism indicating that bulk impurities would lead to the formation of metastable anatase phase along the rutile structures.<sup>171, 187</sup>

Table 4. Crystallite size (D) and d-spacing (d) of rutile TiO<sub>2</sub>, rTiO<sub>2</sub>-needle\_120, rTiO<sub>2</sub>-needle\_200 samples

Sample	D <sub>110</sub> / nm	D <sub>002</sub> /nm	d <sub>110</sub> / nm	d <sub>002</sub> /nm
Rutile TiO <sub>2</sub>	23.6	27.0	0.325	0.148
rTiO <sub>2</sub> -needles_120	6.9	12.7	0.325	0.148
rTiO <sub>2</sub> -needles_200	9.7	25.9	0.325	0.148

### 4.3 Optical properties of rutile needles

Diffuse-reflectance UV-Vis-NIR spectroscopy (DRS) was employed to study the optical properties of the rutile samples. The spectra were recorded in the range 250-1100 nm and results are shown in figure 37. Rutile  $\text{TiO}_2$  exhibits characteristic intrinsic absorption due to band-to-band transition. Moreover, no below-edge absorption in the Vis region was observed. The absence of Vis absorption suggests that the  $\text{TiO}_2$  structure in rutile  $\text{TiO}_2$  is free of defects. The DRS spectrum of  $\text{rTiO}_2$ -needles\_120 is comparable with that of rutile  $\text{TiO}_2$ , showing no below-edge absorption. In the case of  $\text{rTiO}_2$ -needle\_200, however, visible light absorption up to 700 nm can be observed. The reason for Vis absorption here is not fully clear, but it might originate from structural defects/stacking faults upon crystal growth by coalescence. It is reasonable to think that chemical bonding of atoms at joint points can be altered. The weaker bonding at such sites reduces splitting between bonding and antibonding orbitals compared to valence and conduction band states and thus gives rise to electronic states within the semiconductor band gap.<sup>188</sup> However, in spite of them being present, their concentration seems to be rather low, since  $\text{rTiO}_2$ -needles\_200 are a white powder. It has been shown that calcination at higher temperatures, such as 673 K can eliminate some of the defects and reduce the visible light absorption in rutile nanoparticles.<sup>133</sup>

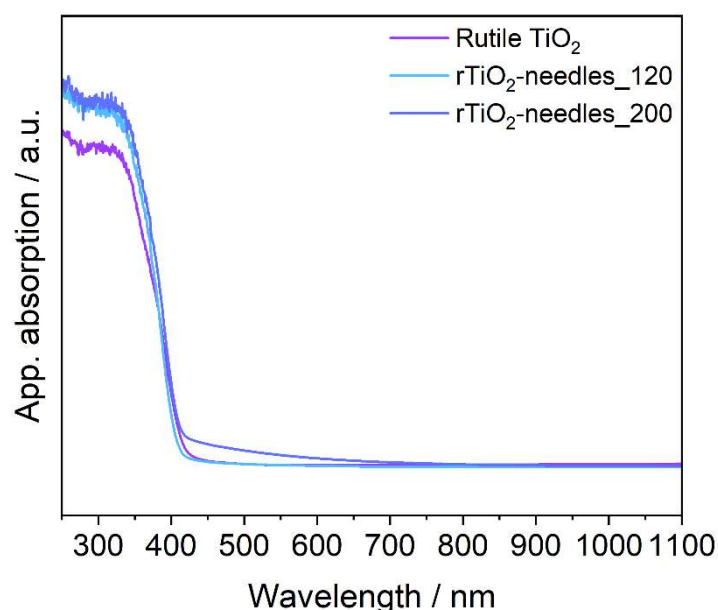


Figure 37. DRS spectra of rutile  $\text{TiO}_2$ ,  $\text{rTiO}_2$ -needle\_120,  $\text{rTiO}_2$ -needle\_200 samples

The onset of the absorption edge in rutile samples was derived from DRS data using Tauc analysis (fig. 38). The band gap of the rutile  $\text{TiO}_2$  is 3.00 eV. In  $\text{rTiO}_2$ -needles\_120 and  $\text{rTiO}_2$ -needles\_200 band gaps are 3.06 and 3.03 eV, respectively, values that are comparable with that of rutile  $\text{TiO}_2$ . In  $\text{rTiO}_2$ -needles\_200, due to the Vis absorption, an additional absorption

edge at 1.79 eV could be determined by the graphical method (fig. 38, inset). However, it should be stressed that Vis absorption is very weak, thus it is not expected to have pronounced influence on photocatalytic performance under solar light, if any.

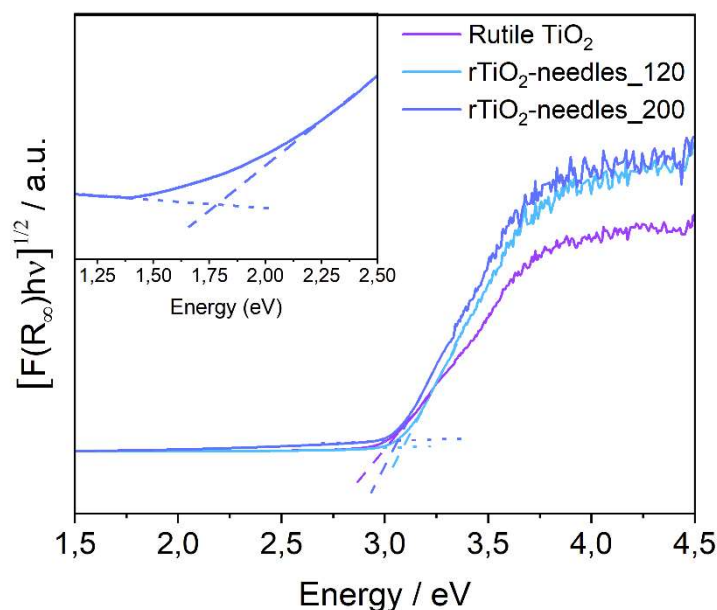


Figure 38. Tauc plots of rutile TiO<sub>2</sub>, rTiO<sub>2</sub>-needle\_120, rTiO<sub>2</sub>-needle\_200 samples. Inset enlarges the 1.15 – 2.50 eV energy range in rTiO<sub>2</sub>-needle\_200 sample

#### 4.4 Analysis of surface states in rutile needles

X-ray photoelectron spectroscopy analysis is performed to study the surface chemical states of the rutile samples (fig. 39). In the Ti 2p spectra of rutile TiO<sub>2</sub> (fig. 39, top), a doublet at binding energies of 458.6 and 464.3 eV arises from spin orbit-splitting of Ti 2p<sub>3/2</sub> and Ti 2p<sub>1/2</sub> of Ti<sup>4+</sup> states in TiO<sub>2</sub>.<sup>155</sup> In the rutile needles samples peaks are shifted by 0.1 eV from Fermi level comparing with commercial rutile TiO<sub>2</sub>, but the spin orbit-splitting constant of 5.7 eV is the same in all three samples. Please note that uncertainty of XP measurements is ±0.3 eV. Thus, based on binding energy and spin orbit-splitting constant values, XP analysis indicates the identical chemical state of surface Ti ions in rutile samples. Beside Ti<sup>4+</sup> ion, no obvious Ti<sup>3+</sup> signals could be observed in the Ti 2p region of the rutile samples.

In the O 1s spectra (Fig. 39, bottom), a well-formed peak at 529.8 eV and a weak shoulder at 531.4 eV are observed in rutile TiO<sub>2</sub>. In the rutile needle samples once again 0.1 eV high energy shift is observed, which falls within uncertainty range similarly as in the case of Ti 2p. The peak at a binding energy of 529.8 eV is attributed to the lattice oxygen in TiO<sub>2</sub>, while the interpretation of the high binding energy shoulder is

somewhat complicated since it could arise from multiple hydroxyl groups.<sup>189, 190</sup> Nevertheless, from the O 1s spectra it becomes clear that the shape of the shoulder at 531.4 eV is very similar in rTiO<sub>2</sub>-needles\_200 and rutile TiO<sub>2</sub>, suggesting similar amount

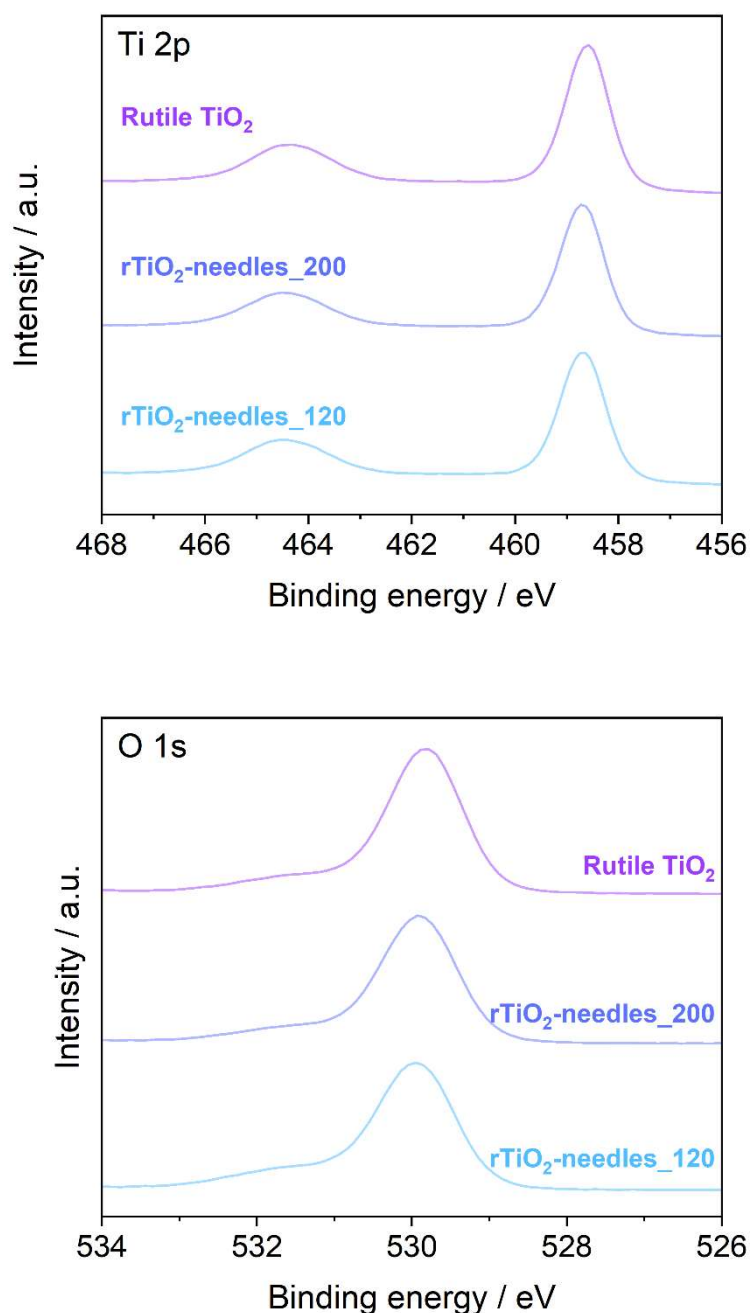


Figure 39. High-resolution XPS spectra of rutile TiO<sub>2</sub>, rTiO<sub>2</sub>-needle\_120, rTiO<sub>2</sub>-needle\_200 samples in the Ti 2p (top) and O 1s (bottom) regions

and nature of hydroxyl groups in both samples. Comparing with them, a higher content of hydroxyl groups was confirmed in the rTiO<sub>2</sub>-needles\_120 sample. The higher hydroxyl content suggests enhanced surface hydration of rTiO<sub>2</sub>-needles\_120 through dissociative adsorption of water, which fits well to the structure data (fig. 35, fig. 36,

Table 4) explaining the mechanism of crystal growth in rutile needles at temperature of 200 °C.<sup>184</sup> Therefore, a stronger hydroxyl signal may arise from hydroxyl groups stabilizing crystal caps in rTiO<sub>2</sub>-needles<sub>120</sub>. Also, in rutile samples no more high binding energy features are observed. The absence of a signal at ca. 533 eV indicates that no physisorption of water occurs at the surface of rutile samples, which agrees with predictions that adsorption of water on the hydroxylated rutile TiO<sub>2</sub> (111) surface is expected to be weak. In fact, the calculated adsorption energy is -0.48 eV, ascribable to the physisorption of H<sub>2</sub>O by hydrogen bonding to the surface hydroxides, and it is close to the water-water interaction energy in solution (ca. -0.4 eV).<sup>184, 191</sup>

Finally, doping of the surface of rutile needles samples with nitrogen was checked by survey XP analysis in the N 1s region (fig. 40). As already discussed in the morphology and crystal structure section, bulk doping of rutile needle samples is not likely to occur. Therefore, if it happens, only the surface of the samples could be doped with nitrogen. However, as can be seen from the spectra, curves for all three samples in the nitrogen region are featureless, confirming that the surfaces of the rutile samples are free of nitrogen impurities.

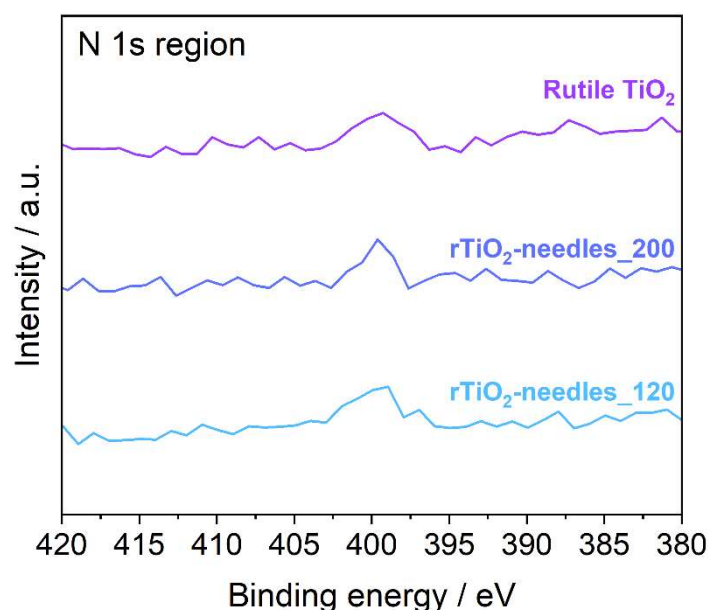


Figure 40. XP survey spectra of rutile TiO<sub>2</sub>, rTiO<sub>2</sub>-needle<sub>120</sub>, rTiO<sub>2</sub>-needle<sub>200</sub> samples in the N 1s region

## 4.5 Photocatalytic activity of rutile needle catalysts in H<sub>2</sub> production

### 4.5.1 H<sub>2</sub> production under 1.5 AM solar simulated light

The catalytic performance of the rutile samples was investigated in the photocatalytic H<sub>2</sub> production under AM 1.5 solar simulated light. Figure 41 shows the photocatalytic H<sub>2</sub> production of rutile TiO<sub>2</sub>, rTiO<sub>2</sub>\_needles\_120 and rTiO<sub>2</sub>\_needles\_200 catalyst from a water/methanol mixture. The catalytic performance of the rutile catalysts was benchmarked with TiO<sub>2</sub> P25. In all catalysts nominally 0.5 wt% Pt co-catalyst was deposited by in situ photoreduction of H<sub>2</sub>PtCl<sub>6</sub>. The samples were tested in three catalytic cycles over 9 hours, where each cycle consists of 2.5 h irradiation and 0.5 h dark intervals. At time 0 hours the light illumination was switched on so that the photocatalytic reaction was started. The in situ photodeposition of the Pt co-catalyst occurs in parallel with the desired catalytic reaction. From H<sub>2</sub> production plots it can be seen that the rutile needle catalysts show higher H<sub>2</sub> production ability under solar light comparing with either rutile TiO<sub>2</sub> or TiO<sub>2</sub> P25 benchmarks, where TiO<sub>2</sub> P25 is more active than rutile TiO<sub>2</sub>. Also, it can be noticed that within the rutile samples only rutile TiO<sub>2</sub> achieved stable operation over all 9 h of test. For example, the rTiO<sub>2</sub>\_needles\_120 catalyst shows exponential decrease in activity within the first 2.5 h. On the other hand, the sharp decrease is substantially smoothed out in the rTiO<sub>2</sub>\_needles\_200 catalyst, though not fully, presumably due to the thermal treatment at 200 °C.

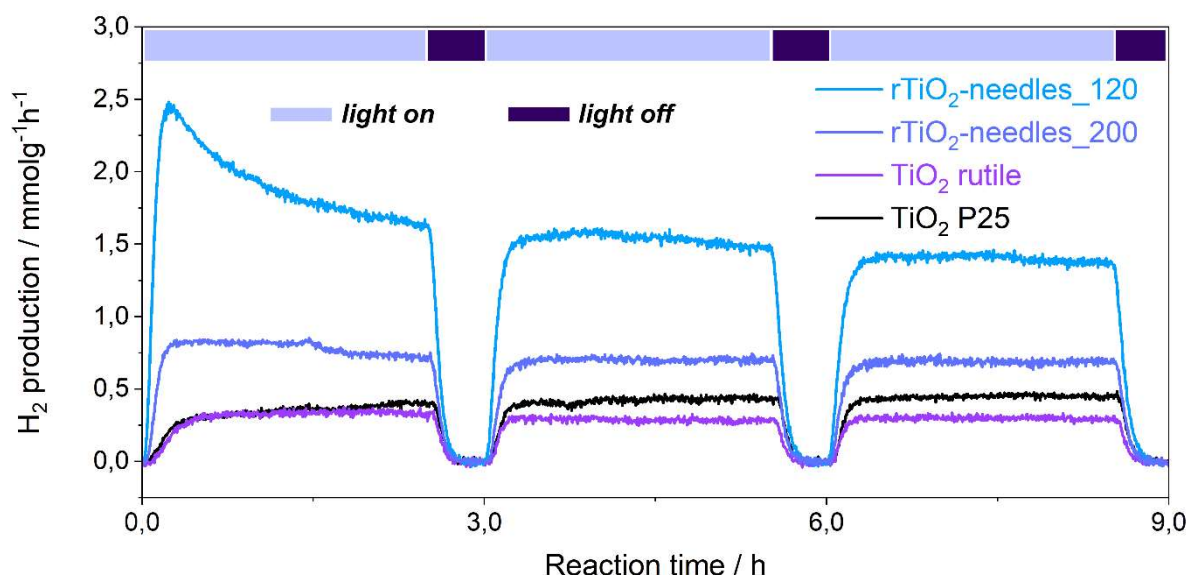


Figure 41. Photocatalytic H<sub>2</sub> production on rutile TiO<sub>2</sub>, rTiO<sub>2</sub>-needle\_120, rTiO<sub>2</sub>-needle\_200 and TiO<sub>2</sub> P25 catalysts



Such decrease in the photocatalytic performance, particularly of the rTiO<sub>2</sub>\_needles\_120 catalyst, might be an indication that the rutile needle structure is not stable under operational conditions, which discussion will follow-up. Alternatively, it may be also caused by non-equilibrium processes that take place at the beginning of catalytic tests. Nevertheless, the H<sub>2</sub> production rate stabilizes during the second test cycle, and finally in the third cycle all rutile catalysts show stable operation. Hence, the photocatalytic activity of TiO<sub>2</sub> catalysts is determined at the end of third test cycle as H<sub>2</sub> production rate in mmolg<sup>-1</sup>h<sup>-1</sup> and results are summarized in Table 5.

Table 5. H<sub>2</sub> production rate of rTiO<sub>2</sub>-needle\_120, rTiO<sub>2</sub>-needle\_200, rutile TiO<sub>2</sub> and TiO<sub>2</sub> P25 catalysts after 7.5 h of illumination

Sample	H <sub>2</sub> production rate / mmolg <sup>-1</sup> h <sup>-1</sup>
rTiO <sub>2</sub> -needles_120	1.38
rTiO <sub>2</sub> -needles_200	0.69
Rutile TiO <sub>2</sub>	0.31
TiO <sub>2</sub> P25	0.45

As already mentioned, rTiO<sub>2</sub>-needles\_120 show the highest H<sub>2</sub> production rate of 1.38 mmolg<sup>-1</sup>h<sup>-1</sup> followed by rTiO<sub>2</sub>-needles\_200, TiO<sub>2</sub> P25 and rutile TiO<sub>2</sub> which produce H<sub>2</sub> at rates of 0.69, 0.45 and 0.31 mmolg<sup>-1</sup>h<sup>-1</sup>, respectively. When compared, rTiO<sub>2</sub>-needles\_120 is twice as active as rTiO<sub>2</sub>-needles\_200, and 3 and 4.5 times more active comparing with TiO<sub>2</sub> P25 and rutile TiO<sub>2</sub>. These results reveal that a temperature increase from 120 to 200 °C during the catalyst preparation strongly influences the catalytic performance of rutile needles and implies that the structure of the material may be a key in design of efficient rutile catalysts for solar H<sub>2</sub> production. After three tests cycles with TiO<sub>2</sub> samples formic acid in liquid phase could not be detected.

#### 4.5.2 H<sub>2</sub> production under sun light

In another photocatalytic experiment, the best performing catalyst under AM 1.5 illumination, rTiO<sub>2</sub>-needles\_120, was re-run in the photocatalytic H<sub>2</sub> production under direct sun light. The sun test was aimed to further study stability of the rTiO<sub>2</sub>-needles\_120 catalyst as well as to benchmark AM 1.5 solar simulated light. Based on H<sub>2</sub> production rates for different TiO<sub>2</sub> materials that are summed-up in Table 1 it can be noticed that photocatalytic activity fluctuates up to seven times even in the case of benchmark TiO<sub>2</sub> P25 catalyst. This can partially be due to the slightly different experimental conditions that were applied e.g., water to methanol ratio or co-catalyst loading. However, it is less likely that they can account for such discrepancies alone. On the other hand, even small deviations of output light spectrum,

particularly in the UV range, from the sun spectrum are known to modulate photocatalytic activity of TiO<sub>2</sub> samples. After all, the higher H<sub>2</sub> production rates would be achieved in the test under simulated light which, though, would not be available by illumination with sun.

To run the sun light test, the rTiO<sub>2</sub>-needles\_120 catalyst was used that was recovered from experiment under AM 1.5 light. Therefore, it is expected that the catalyst shows stable operation under sun light, since the Pt has been already deposited on the catalyst and the Pt-TiO<sub>2</sub> interface has formed. Here, it should be mentioned that the test was performed in a cylindrical pyrex reactor instead of a top-irradiated reactor with flat quartz lid due to technical reasons (see experimental section). The total reaction time under sun light was limited to 2h. The H<sub>2</sub> production rate under sun light is compared with the H<sub>2</sub> production rate at the third cycle under AM 1.5 where stable operation was reached. To account for differences in light intensity as well as illuminated area of the sample in two experiments, the data is presented as specific H<sub>2</sub> production rate in mmol g<sup>-1</sup> h<sup>-1</sup> mW<sup>-1</sup> (see experimental section) and data is shown in fig. 42.

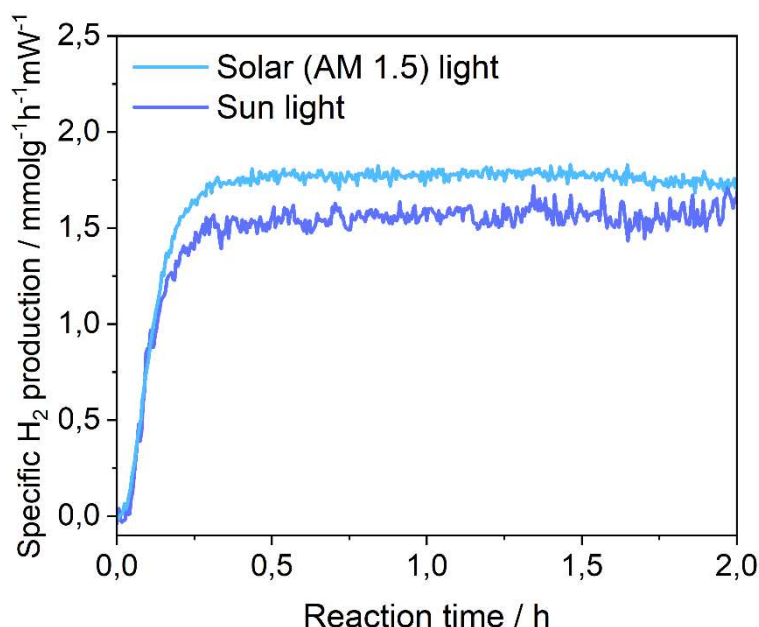


Figure 42. Comparison of photocatalytic H<sub>2</sub> production on rTiO<sub>2</sub>-needles\_120 catalyst under simulated AM 1.5 solar and direct sun illumination.

As expected, the rTiO<sub>2</sub>-needles\_120 catalyst performed stable over 2h under sun light. When compared with AM 1.5 illumination, the achieved H<sub>2</sub> production was about 15 % smaller, presumably due to the lower inherent efficiency of pyrex reactor. In the cylindrical pyrex reactor curved side walls can reflect and scatter light more than a flat quartz window, which causes a decrease in intensity of light that illuminates the catalyst slurry. Although the margin in transparency of pyrex and quartz glass is expected to be low for solar light, the contribution, however, cannot be excluded. Nonetheless, two conclusions can be drawn from the H<sub>2</sub>

production test under sun light: first, the rTiO<sub>2</sub>-needles\_120 produce H<sub>2</sub> at constant rate once the Pt co-catalyst is deposited on the surface of the catalyst and, second, comparable H<sub>2</sub> production rates are achieved under AM 1.5 and sun illumination, indicating that AM 1.5 light plausibly simulates sun light in the laboratory.

To further corroborate catalytic results obtained with the rTiO<sub>2</sub>-needles\_120 catalyst, a morphology analysis of the catalyst after the sun test was performed by TEM (fig. 43). The analysis reveals that the used rTiO<sub>2</sub>-needle-120 catalyst retains its needle-like morphology with secondary particles 200 nm in length and upwards 30 nm in width (fig 43, left). Furthermore, the high magnification micrograph shows the primary particles in the catalyst of about 5 nm in width (fig. 43, right), which is like in the fresh catalyst. The morphology of rTiO<sub>2</sub>\_needles\_120 catalyst is, therefore, comparable before and after photocatalytic tests under simulated solar and sun light (more than 9 h of under illumination), confirming that the decrease of H<sub>2</sub> production rate in fresh catalyst is not likely to be due to structural changes.

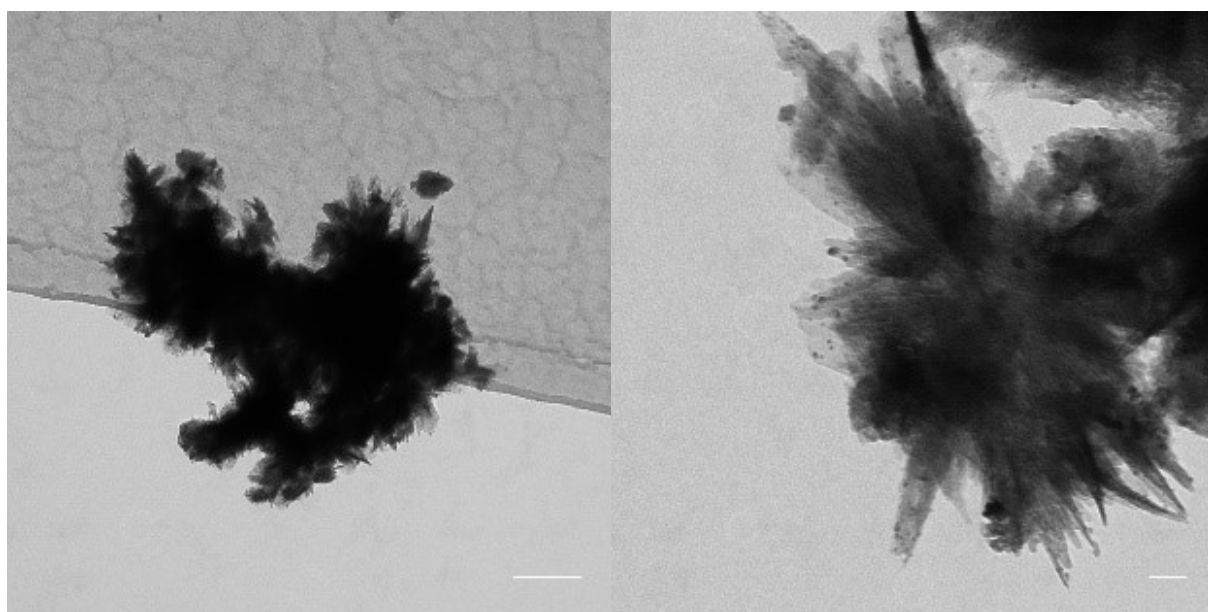


Figure 43. TEM micrographs of spare rTiO<sub>2</sub>\_needles\_120 catalyst. Scale bar is 200 nm (left) and 20 nm (right).

#### *4.5.3 Influence of test conditions on photocatalytic performance of rutile catalysts*

Since photocatalytic tests under AM 1.5 and sun illumination confirmed that the rTiO<sub>2</sub>\_needles\_120 catalyst shows stable performance in photocatalytic H<sub>2</sub> production (fig. 42), and TEM analysis of spare rTiO<sub>2</sub>\_needles\_120 catalyst confirmed that the structure of the catalyst is stable under operation conditions (fig. 43), it is time to address in more detail the decrease in performance observed in fresh rutile needle catalysts at the beginning of the

photocatalytic tests. As already mentioned, only rutile  $\text{TiO}_2$  showed a stable catalytic performance in the first test cycle under the applied conditions (fig. 41). Hence, the influence of the reaction conditions on the initial catalytic performance was investigated in the rutile  $\text{TiO}_2$  catalyst. Here, the standard reaction conditions were kept the same, with the difference being a purging time. The standard purging time of 3 h was reduced to 1 h, which is denoted in figure 44 as long and short purge, respectively. It should be noted that 1 h of purge is sufficient to completely remove oxygen from the reactor.

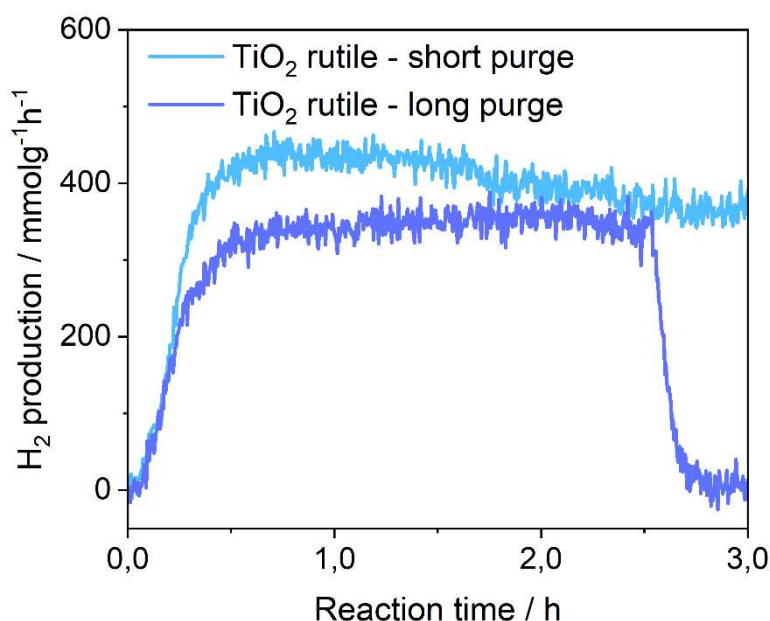


Figure 44. Comparison solar  $\text{H}_2$  production over rutile  $\text{TiO}_2$  catalyst after different purging times applied before photocatalytic reaction

The curve obtained after short purging time was different from the curve obtained after the long one. The difference is observed at the beginning of the test. A short purging time leads to higher activity in the early stage of the reaction. Afterward,  $\text{H}_2$  production activity steadily decreases where the rutile  $\text{TiO}_2$  reaches stable operation after about 2.5 h of illumination. This result suggests that longer purging time may have an effect on Pt deposition or Pt- $\text{TiO}_2$  interface in the rutile  $\text{TiO}_2$  catalysts. Also, the result confirms that the steady-state performance of the catalyst is not affected by the purging time, as far as the reaction is run under oxygen free conditions. Thus, although applying the standardized reaction conditions in catalytic tests is generally recommended, the optimal reaction conditions may vary from sample to sample. This can in turn hinder the data interpretation as showcased on the examples of studied rutile catalysts. Obviously, more experiments are needed to optimize the reaction conditions for rutile needle catalysts for photocatalytic  $\text{H}_2$  production.

## 4.6 Structure-activity relationship in rutile needle catalysts

Finally, in this section the influence of the structure of rutile photocatalysts on the H<sub>2</sub> production under solar light will be discussed. The rutile samples were characterized in detail in terms of morphology, crystal structure, surface states and optical properties. Little to no difference in optical absorption and band gaps among the different rutile samples was observed (fig. 37 and 38, respectively). Optical absorption is dominated by band-to-band transition and the band edge onset was around 3 eV, characteristic for rutile TiO<sub>2</sub>. The surface of the three rutile samples is free of nitrogen, suggesting that doping with nitrogen did not occur in these rutile needles catalysts. Also, the surface states in the rutile samples remain grossly unchanged regardless the applied processing temperature (fig. 39). However, the change in the processing temperature from 120 to 200 °C induced changes in the morphology and crystal structure of the rutile needles samples. On one side, primary particles cannot be anymore observed in rTiO<sub>2</sub>-needles\_200 catalyst, while the morphology of secondary particles is shifting from needle-like to plate-like (fig. 35). On the other hand, the change in the crystal structure is illustrated at first place by thermally induced crystal growth (fig. 36, Table 4). Both crystal growth directions, in the ab plane and along the c-axis, were affected. However, the crystals grow preferentially in c-direction. Therefore, to study the effect of anisotropic crystal growth the photocatalytic activity of the three rutile samples is plotted against the crystallite size of the 110 and 002 Bragg peaks (fig. 45). As can be seen from the graphs, the dependence of the activity on the crystallite size of both peaks is not linear. The photocatalytic activity data is then fitted with a nonlinear function, where a reasonably good fit is obtained for the 110 Bragg peak employing an exponential decay function (fig.45, top). When nonlinear fitting of the photocatalytic data in function of the crystallite size of the 002 Bragg peak is attempted, no correlation is obtained (fig. 45, bottom). Hence, it can be concluded that the crystallite size of the 110 Bragg peak may be the key to explain in systematic way H<sub>2</sub> production on rutile samples under solar light.

To understand the dependence of the photocatalytic activity in function of the 110 Bragg peak, we will now discuss charge carrier dynamics as well as facet-dependent charge carrier separation in rutile TiO<sub>2</sub>. The charge carrier dynamics have been studied in nanoparticulate and single crystal rutile TiO<sub>2</sub>.<sup>91, 92</sup> In general, photogenerated charge carrier decay is dominated by recombination of trapped electrons with holes which in rutile follows exponential decay kinetics regardless of the samples morphology. It has been also shown that bulk rather than surface recombination is the primary determinant of charge carrier lifetime which can be prolonged by reduction of particle size.<sup>91</sup> Hence, charge carrier dynamics experiments pointing out that decreasing the bulk charge carrier diffusion path by reduction of particle size via nanostructuring plays an important role in improving transport of the photogenerated charge carriers and may explain why differences in photocatalytic activity were observed for small structural changes in undoped rutile TiO<sub>2</sub>. The nanostructuring effect in rutile TiO<sub>2</sub>, however, should not be confused with the effect that aspect ratio has, particularly on big rutile crystals.<sup>172</sup> In sub-micrometer to micrometer crystals increase of

aspect ratio likely means that crystals expose more (110) facets which accounts for better performance rather than the influence of aspect ratio on charge carrier dynamics.

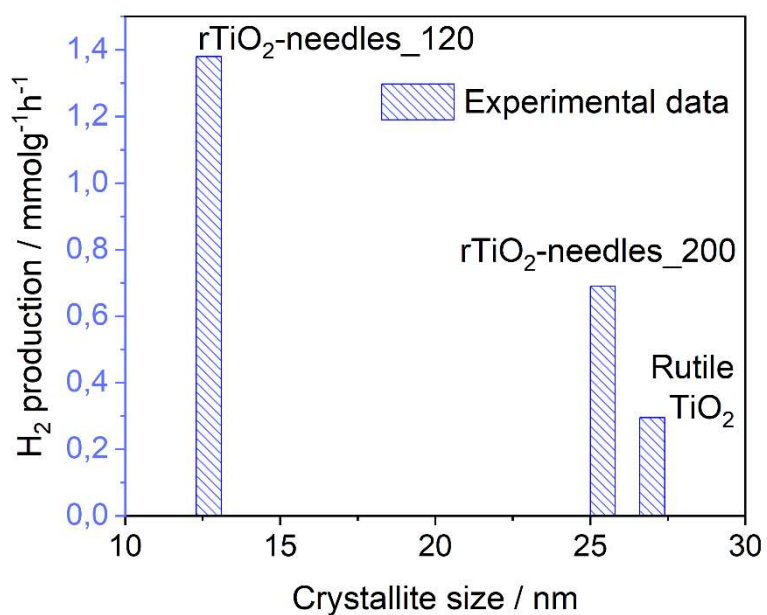
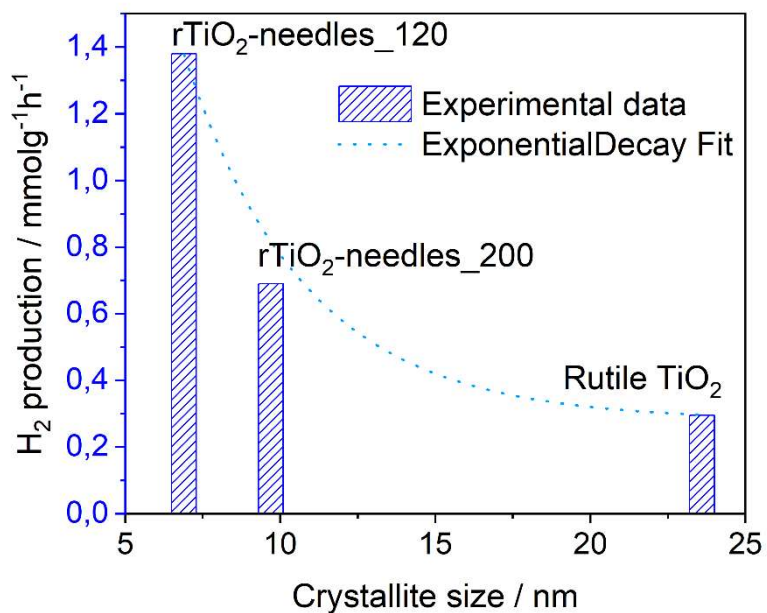


Figure 45. Structure-activity correlation for (110) (left) and (002) (right) Bragg peaks in rutile catalysts

Under illumination of rutile, photogenerated electrons are separated in facet-dependent manner. It has been demonstrated on rutile particles with exposed (110) and (011) facets that hexachloroplatinat(IV) is preferentially photodeposited on (110) surfaces as metallic Pt regardless the facet composition of rutile particles, meaning that photogenerated electrons accumulate at (110) rutile surfaces.<sup>192</sup> In fact, (011) facets lay in the crystal caps, while (110) facets form the body of the rutile crystal, implying that structural anisotropy may have an influence on electrical conductivity in rutile TiO<sub>2</sub>. As a counter-argument to facet selective deposition of Pt often is offered that preferential adsorption of co-catalyst precursor at semiconductor surface can drive the Pt deposition.<sup>193</sup> This assumption is based on the similar Pt coverage patterns obtained after deposition of Pt employing photodeposition and impregnation methods. However, when Pt photodeposition and impregnation are compared on rutile TiO<sub>2</sub>, it shows selective, facet-dependent Pt deposition while impregnation results in the non-selective coverage of the surface with Pt nanoparticles.<sup>172</sup> Under dark conditions it has been observed that for crystallographic azimuths parallel to (110) plane the highest electrical conductivity is along c-axis.<sup>194</sup> However, in the case of photogenerated electrons the charge transport is swapped, meaning that highest electron migration is observed in the direction perpendicular to c-axis i.e., in ab plane.<sup>195</sup> Thus, this experiment confirms the hypothesis that reduction of charge carrier diffusion path leads to enhanced catalytic activity and additionally demonstrates that electron transport, controlled by crystal growth in ab plane, is the key for efficient solar H<sub>2</sub> production on rutile TiO<sub>2</sub> catalysts.

## 4.7 Conclusions

In summary, rutile needles with sub-10 nm crystallites were successfully synthesized as white powders from TTIP by wet method under acidic conditions at room temperature. Structural characterization results confirm that these needle samples are pure phase rutile polycrystalline TiO<sub>2</sub>. Moreover, the data reveal that at 200 °C anisotropic thermally induced crystal growth occurs, preferentially along crystal c-axis and triggers the change of morphology from needle to plate. No surface doping with nitrogen is observed in the rutile needles under the applied conditions, while the onset of the absorption edge is around 3 eV, typical for the rutile polymorph. The platinized (0.5 wt.% Pt) rutile needle sample rTiO<sub>2</sub>-needles\_120 achieves high hydrogen production rate of 1.38 mmolg<sup>-1</sup>h<sup>-1</sup> from water/methanol solution under solar simulated light (AM 1.5), a 3- and 4.5-times higher production rate than that of nanoparticulate TiO<sub>2</sub> P25 and rutile TiO<sub>2</sub> benchmarks, respectively. Moreover, it is found that solar H<sub>2</sub> production on rutile TiO<sub>2</sub> catalysts follows a decreasing exponential function of crystallite size in ab crystal plane. This effect correlates with improved charge carrier dynamics due to the shortening of the electron diffusion path. The results of this experiment provide valuable insights into the structure-activity relationships in rutile TiO<sub>2</sub> and considering the advantage and versatility offered by this

synthesis method, the findings here can have an important impact on making efficient TiO<sub>2</sub> photocatalysts for solar applications a reality.



## 5. Final conclusions and prospects

Within this thesis the design principles that focus on intrinsic improvement of TiO<sub>2</sub> photocatalysts for solar H<sub>2</sub> production were investigated. On the one hand, the self-doping of TiO<sub>2</sub> was performed to enhance light harvesting and broaden working solar spectrum of TiO<sub>2</sub>, which can stimulate charge carrier production in TiO<sub>2</sub> photocatalysts. On the other hand, it was investigated how TiO<sub>2</sub> nanostructuring influences the length of bulk charge carrier diffusion path and its effect on charge carrier dynamics in TiO<sub>2</sub>. Finally, the structure of TiO<sub>2</sub> photocatalysts was correlated with photocatalytic activity, charge carrier production compared with charge carrier dynamics, and a guideline for design of next generation TiO<sub>2</sub> catalysts for solar application was provided.

In the first part of the thesis the impact of Ti<sup>3+</sup> ions in self-doped TiO<sub>2</sub> on light harvesting and solar H<sub>2</sub> production was investigated. The blue self-doped TiO<sub>2</sub> was synthesized in the reaction of TiO<sub>2</sub> with Na/K alloy at room temperature, and it shows outstanding color stability under storing at ambient conditions. The structural characterization reveals that self-doped TiO<sub>2</sub> has a hybrid TiO<sub>2</sub>@Ti<sup>3+</sup>/TiO<sub>2</sub>@TiO<sub>2</sub> structure, where the disordered layer is embedded between the TiO<sub>2</sub> crystalline core that was left unreacted, and the TiO<sub>2</sub> overlayer. Further, the Ti<sup>3+</sup> ions are preferentially formed in the disordered layer and their amount is a function of the amount of added Na/K alloy i.e., an extent of Na intercalation into TiO<sub>2</sub> framework. The intercalated Na seems to be crucial for long-term stabilization of Ti<sup>3+</sup> ions. However, due to the thermal instability of Na-TiO<sub>2</sub> intercalation product, after 1h at 400°C in Ar atmosphere the intercalated Na deintercalates from TiO<sub>2</sub> host. The Ti<sup>3+</sup> ions unlock visible and near infrared light absorption in self-doped TiO<sub>2</sub> by introduction of in-band electronic states 1.3 eV below the conduction band. In the photocatalytic test, platinumized self-doped TiO<sub>2</sub> (0.5 wt% Pt) achieves a H<sub>2</sub> production rate of 44 μmolg<sup>-1</sup>h<sup>-1</sup> from methanol/water mixture under solar simulated light (AM 1.5), which is 9 times less than that of TiO<sub>2</sub> P25 in spite of the fact that solar light absorption has been substantially increased in self-doped TiO<sub>2</sub>. After the Ti<sup>3+</sup> ions are removed from the B-TiO<sub>2</sub> structure, the activity of G-TiO<sub>2</sub>/AC catalyst is enhanced by a factor more than 4. When present, Ti<sup>3+</sup> deactivates self-doped TiO<sub>2</sub> catalysts and deactivation is an increasing function of the Ti<sup>3+</sup> amount. Therefore, the nature and spatial distribution of Ti<sup>3+</sup> ions within the TiO<sub>2</sub> framework strongly influence H<sub>2</sub> production in self-doped TiO<sub>2</sub>. The Ti<sup>3+</sup> ions formed in the disordered layer increases the bulk defect density in TiO<sub>2</sub>, which hampers charge carrier dynamics and lead to the sluggish H<sub>2</sub> production.

In the next section, the size effect of rutile structures on solar H<sub>2</sub> production was studied. The rutile needles with sub-10 nm crystallites were successfully synthesized as white powders from TTIP by wet method under acidic conditions at room temperature. Structural characterization confirms that these needle samples are pure phase rutile crystalline TiO<sub>2</sub>. Furthermore, the data reveals that at 200 °C anisotropic thermally induced crystal growth occurs, preferentially along crystal c-axis and triggers the change of morphology from needle to plate. The surface analysis indicates that no surface doping with nitrogen occurs in the rutile needles under the applied conditions. The onset of the absorption edge in rutile needles is

around 3 eV, the value which is typical for the rutile TiO<sub>2</sub> polymorph. The platinumized (0.5 wt.% Pt) rutile needle sample rTiO<sub>2</sub>-needles\_120 achieves high hydrogen production rate of 1.38 mmolg<sup>-1</sup>h<sup>-1</sup> from water/methanol solution under solar simulated light (AM 1.5), a 3- and 4.5-times higher production rate than that of nanoparticulate TiO<sub>2</sub> P25 and rutile TiO<sub>2</sub> benchmarks, respectively. Beside the photocatalytic test under solar simulated light, the real potential of rTiO<sub>2</sub>-needles\_120 in solar H<sub>2</sub> production is confirmed in H<sub>2</sub> production test under direct sun illumination. Lastly, it is found that solar H<sub>2</sub> production on rutile TiO<sub>2</sub> catalysts follows a decreasing exponential function of crystallite size in ab crystal plane. The effect correlates with improved charge carrier dynamics due to the shortening of the electron diffusion path which allows efficient solar H<sub>2</sub> production on rutile needle structure.

The results of doping and nanostructuring experiments provide insights into the structure-activity relationships in self-doped TiO<sub>2</sub> and rutile needles and suggest that charge carrier dynamics influences to a larger extent the photocatalytic activity of TiO<sub>2</sub> photocatalysts compared to charge carrier production. Thus, well-structured defect-free TiO<sub>2</sub> catalysts that separate photogenerated electrons and holes efficiently are good candidates for H<sub>2</sub> production under solar light. However, doped-TiO<sub>2</sub> structures with enhanced solar light harvesting could also be considered for solar H<sub>2</sub> production only if post-growth transformation and degradation of subsurface TiO<sub>2</sub> layer that typically occur during diffusion-based doping is circumvented.

Finally, having hands on the efficient photocatalytic system such as rutile needles, in general, can open-up plethora of new possibilities for the solar photocatalysis research. First and foremost, further research following the established design guideline could help discovering more efficient catalysts for solar application in perspective. Second, once rutile needles are intrinsically optimized, they can serve as a good candidate for construction of e.g., heterojunction catalysts, where charge flow can be on purpose engineered within the scheme and further improve charge carrier dynamics in the system and its solar photocatalytic activity. Third, the solar H<sub>2</sub> production tests on rutile needles with industrially relevant electron donors can be meaningful direction of research. Although short chain alcohol such as methanol is the electron donor of choice due to the higher initial performance and complete oxidation that requires smaller number of reaction intermediates, for practical application use of renewable feedstocks would be advantageous. In that way, the biomass can be valorized by producing carbon neutral, green hydrogen and added value raw materials. Lastly, running the long-term photocatalytic tests with rutile needle catalysts would allow the study of deactivation mechanism of catalyst, which can be a missing piece that could be expected to inspire development of more advanced catalytic systems in the future, making rutile TiO<sub>2</sub> polymorph more attractive for practical solar application.

# References

1. <https://www.iea.org/reports/global-energy-review-co2-emissions-in-2021-2>).
2. P. Falkowski, R. Scholes, E. Boyle, J. Canadell, D. Canfield, J. Elser, N. Gruber, K. Hibbard, P. Högberg and S. Linder, *science*, 2000, **290**, 291-296.
3. C. Le Quéré, R. J. Andres, T. Boden, T. Conway, R. A. Houghton, J. I. House, G. Marland, G. P. Peters, G. Van der Werf and A. Ahlström, *Earth System Science Data Discussions*, 2012, **5**, 1107-1157.
4. Earth System Research Laboratory Global Monitoring Division, Trends in Atmospheric Carbon Dioxide and Recent Monthly Average Manua Loa carbon dioxide, (<http://www.esrl.noaa.gov/gmd/ccqg/trends/>),, 2022.
5. D. Bogdanov, J. Farfan, K. Sadovskaia, A. Aghahosseini, M. Child, A. Gulagi, A. S. Oyewo, L. de Souza Noel Simas Barbosa and C. Breyer, *Nature communications*, 2019, **10**, 1-16.
6. N. S. Lewis and D. G. Nocera, *Proceedings of the National Academy of Sciences*, 2006, **103**, 15729-15735.
7. J. Nowotny, *Oxide semiconductors for solar energy conversion: titanium dioxide*, CRC press, 2011.
8. R. Schlögl, *Chemical energy storage*, de Gruyter Berlin, 2013.
9. H. Luo, J. Barrio, N. Sunny, A. Li, L. Steier, N. Shah, I. E. Stephens and M. M. Titirici, *Advanced Energy Materials*, 2021, **11**, 2101180.
10. A. Sartbaeva, V. Kuznetsov, S. Wells and P. Edwards, *Energy & Environmental Science*, 2008, **1**, 79-85.
11. B. A. Pinaud, J. D. Benck, L. C. Seitz, A. J. Forman, Z. Chen, T. G. Deutsch, B. D. James, K. N. Baum, G. N. Baum and S. Ardo, *Energy & Environmental Science*, 2013, **6**, 1983-2002.
12. D. M. Fabian, S. Hu, N. Singh, F. A. Houle, T. Hisatomi, K. Domen, F. E. Osterloh and S. Ardo, *Energy & Environmental Science*, 2015, **8**, 2825-2850.
13. A. Kudo and Y. Miseki, *Chemical Society Reviews*, 2009, **38**, 253-278.
14. G. Korotcenkov, *Titanium Dioxide (TiO<sub>2</sub>) and Its Applications*, Elsevier, 2020.
15. S. Chen, T. Takata and K. Domen, *Nature Reviews Materials*, 2017, **2**, 1-17.
16. S. Zhu and D. Wang, *Advanced Energy Materials*, 2017, **7**, 1700841.
17. B. Ohtani, *Journal of Photochemistry and Photobiology C: Photochemistry Reviews*, 2010, **11**, 157-178.
18. C. A. Gueymard, D. Myers and K. Emery, *Solar energy*, 2002, **73**, 443-467.
19. N. Genitori and G. Di Marco, in *Titanium Dioxide (TiO<sub>2</sub>) and Its Applications*, Elsevier, 2021, pp. 169-209.
20. J. Strunk, in *Metal Oxides in Energy Technologies*, Elsevier, 2018, pp. 275-301.
21. R. Beranek, *Advances in Physical Chemistry*, 2011, **2011**.
22. J. Li and N. Wu, *Catalysis Science & Technology*, 2015, **5**, 1360-1384.
23. J. Schneider, M. Matsuoka, M. Takeuchi, J. Zhang, Y. Horiuchi, M. Anpo and D. W. Bahnemann, *Chemical reviews*, 2014, **114**, 9919-9986.
24. S. N. Habisreutinger, L. Schmidt-Mende and J. K. Stolarczyk, *Angewandte Chemie International Edition*, 2013, **52**, 7372-7408.
25. S. Buller and J. Strunk, *Journal of Energy Chemistry*, 2016, **25**, 171-190.
26. T. Takata, J. Jiang, Y. Sakata, M. Nakabayashi, N. Shibata, V. Nandal, K. Seki, T. Hisatomi and K. Domen, *Nature*, 2020, **581**, 411-414.
27. P. Naliwajko and J. Strunk, *Heterogeneous Photocatalysis: From Fundamentals to Applications in Energy Conversion and Depollution*, 2021, 101-126.
28. U. Diebold, *Surface science reports*, 2003, **48**, 53-229.
29. A. Fujishima and K. Honda, *nature*, 1972, **238**, 37-38.
30. T. Inoue, A. Fujishima, S. Konishi and K. Honda, *Nature*, 1979, **277**, 637-638.

31. K. Maeda, *Chemical Communications*, 2013, **49**, 8404-8406.
32. J. B. Priebe, J. r. Radnik, A. J. Lennox, M.-M. Pohl, M. Karnahl, D. Hollmann, K. Grabow, U. Bentrup, H. Junge and M. Beller, *Acs Catalysis*, 2015, **5**, 2137-2148.
33. H. Zhang and J. F. Banfield, *Chemical reviews*, 2014, **114**, 9613-9644.
34. D. A. Hanaor and C. C. Sorrell, *Journal of Materials science*, 2011, **46**, 855-874.
35. M. Ranade, A. Navrotsky, H. Zhang, J. Banfield, S. Elder, A. Zaban, P. Borse, S. Kulkarni, G. Doran and H. Whitfield, *Proceedings of the National Academy of Sciences*, 2002, **99**, 6476-6481.
36. H. Zhang and J. F. Banfield, *The Journal of Physical Chemistry B*, 2000, **104**, 3481-3487.
37. X. Chen and S. S. Mao, *Chemical reviews*, 2007, **107**, 2891-2959.
38. Y. Li, C. Yang, F. Zheng, Q. Pan, Y. Liu, G. Wang, T. Liu, J. Hu and M. Liu, *Nano Energy*, 2019, **59**, 582-590.
39. L. Zhou, W. Utetiwabo, R. Chen and W. Yang, 2019.
40. K. Bourikas, C. Kordulis and A. Lycourghiotis, *Chemical reviews*, 2014, **114**, 9754-9823.
41. P. Smith and S. Bernasek, *Surface science*, 1987, **188**, 241-254.
42. O. Bikondoa, C. L. Pang, R. Ithnin, C. A. Muryn, H. Onishi and G. Thornton, *Nature materials*, 2006, **5**, 189-192.
43. I. Brookes, C. Muryn and G. Thornton, *Physical review letters*, 2001, **87**, 266103.
44. R. Schaub, P. Thstrup, N. Lopez, E. Lægsgaard, I. Stensgaard, J. K. Nørskov and F. Besenbacher, *Physical Review Letters*, 2001, **87**, 266104.
45. A. Kornherr, D. Vogtenhuber, M. Ruckebauer, R. Podloucky and G. Zifferer, *The Journal of chemical physics*, 2004, **121**, 3722-3726.
46. M. A. Henderson, *Langmuir*, 1996, **12**, 5093-5098.
47. G. Liu, H. G. Yang, J. Pan, Y. Q. Yang, G. Q. Lu and H.-M. Cheng, *Chemical reviews*, 2014, **114**, 9559-9612.
48. M. Ramamoorthy, D. Vanderbilt and R. King-Smith, *Physical Review B*, 1994, **49**, 16721.
49. H. Perron, C. Domain, J. Roques, R. Drot, E. Simoni and H. Catalette, *Theoretical Chemistry Accounts*, 2007, **117**, 565-574.
50. F. Labat, P. Baranek and C. Adamo, *Journal of Chemical Theory and Computation*, 2008, **4**, 341-352.
51. D. Su, S. Dou and G. Wang, *Chemistry of Materials*, 2015, **27**, 6022-6029.
52. X. Yang, C. Wang, Y. Yang, Y. Zhang, X. Jia, J. Chen and X. Ji, *Journal of Materials Chemistry A*, 2015, **3**, 8800-8807.
53. G. Longoni, R. L. Pena Cabrera, S. Polizzi, M. D'Arienzo, C. M. Mari, Y. Cui and R. Ruffo, *Nano Letters*, 2017, **17**, 992-1000.
54. M. Lazzeri, A. Vittadini and A. Selloni, *Physical Review B*, 2001, **63**, 155409.
55. C. Arrouvel, M. Digne, M. Breyse, H. Toulhoat and P. Raybaud, *Journal of Catalysis*, 2004, **222**, 152-166.
56. A. Beltran, J. Sambrano, M. Calatayud, F. Sensato and J. Andres, *Surface science*, 2001, **490**, 116-124.
57. D. Friedmann, A. Hakki, H. Kim, W. Choi and D. Bahnemann, *Green Chemistry*, 2016, **18**, 5391-5411.
58. A. Pougin, M. Dilla and J. Strunk, *Physical Chemistry Chemical Physics*, 2016, **18**, 10809-10817.
59. B. Ohtani, O. Prieto-Mahaney, D. Li and R. Abe, *Journal of Photochemistry and Photobiology A: Chemistry*, 2010, **216**, 179-182.
60. R. I. Bickley, T. Gonzalez-Carreno, J. S. Lees, L. Palmisano and R. J. Tilley, *Journal of solid state chemistry*, 1991, **92**, 178-190.
61. Y. Ide, N. Inami, H. Hattori, K. Saito, M. Sohmiya, N. Tsunoji, K. Komaguchi, T. Sano, Y. Bando and D. Golberg, *Angewandte Chemie International Edition*, 2016, **55**, 3600-3605.
62. T. Ohno, K. Sarukawa, K. Tokieda and M. Matsumura, *Journal of Catalysis*, 2001, **203**, 82-86.
63. X. Jiang, M. Manawan, T. Feng, R. Qian, T. Zhao, G. Zhou, F. Kong, Q. Wang, S. Dai and J. H. Pan, *Catalysis Today*, 2018, **300**, 12-17.

64. L. Kavan, M. Grätzel, S. Gilbert, C. Klemenz and H. Scheel, *Journal of the American Chemical Society*, 1996, **118**, 6716-6723.
65. D. C. Hurum, A. G. Agrios, K. A. Gray, T. Rajh and M. C. Thurnauer, *The Journal of Physical Chemistry B*, 2003, **107**, 4545-4549.
66. D. O. Scanlon, C. W. Dunnill, J. Buckeridge, S. A. Shevlin, A. J. Logsdail, S. M. Woodley, C. R. A. Catlow, M. Powell, R. G. Palgrave and I. P. Parkin, *Nature materials*, 2013, **12**, 798-801.
67. R. Asahi, T. Morikawa, T. Ohwaki, K. Aoki and Y. Taga, *science*, 2001, **293**, 269-271.
68. S. U. Khan, M. Al-Shahry and W. B. Ingler Jr, *science*, 2002, **297**, 2243-2245.
69. M. R. Hoffmann, S. T. Martin, W. Choi and D. W. Bahnemann, *Chemical reviews*, 1995, **95**, 69-96.
70. C. Di Valentin, G. Pacchioni and A. Selloni, *Physical review B*, 2004, **70**, 085116.
71. C. Di Valentin and G. Pacchioni, *Catalysis today*, 2013, **206**, 12-18.
72. Y. Li, G. Ma, S. Peng, G. Lu and S. Li, *Applied Surface Science*, 2008, **254**, 6831-6836.
73. R. Sasikala, A. Shirole, V. Sudarsan, C. Sudakar, R. Naik, R. Rao and S. Bharadwaj, *Applied Catalysis A: General*, 2010, **377**, 47-54.
74. X. Sun, H. Liu, J. Dong, J. Wei and Y. Zhang, *Catalysis letters*, 2010, **135**, 219-225.
75. E. Borgarello, J. Kiwi, M. Graetzel, E. Pelizzetti and M. Visca, *Journal of the American chemical society*, 1982, **104**, 2996-3002.
76. R. Niishiro, H. Kato and A. Kudo, *Physical Chemistry Chemical Physics*, 2005, **7**, 2241-2245.
77. Y. Ma, X. Wang, Y. Jia, X. Chen, H. Han and C. Li, *Chemical reviews*, 2014, **114**, 9987-10043.
78. S. Sakthivel and H. Kisch, *Angewandte Chemie International Edition*, 2003, **42**, 4908-4911.
79. F. Zuo, L. Wang, T. Wu, Z. Zhang, D. Borchardt and P. Feng, *Journal of the American Chemical Society*, 2010, **132**, 11856-11857.
80. J. Strunk, W. C. Vining and A. T. Bell, *The Journal of Physical Chemistry C*, 2010, **114**, 16937-16945.
81. H. Tan, Z. Zhao, M. Niu, C. Mao, D. Cao, D. Cheng, P. Feng and Z. Sun, *Nanoscale*, 2014, **6**, 10216-10223.
82. A. Naldoni, M. Altomare, G. Zoppellaro, N. Liu, S. Kment, R. Zboril and P. Schmuki, *ACS catalysis*, 2018, **9**, 345-364.
83. T. L. Thompson and J. T. Yates, *Chemical reviews*, 2006, **106**, 4428-4453.
84. Y. Zhang, Z. Xing, X. Liu, Z. Li, X. Wu, J. Jiang, M. Li, Q. Zhu and W. Zhou, *ACS applied materials & interfaces*, 2016, **8**, 26851-26859.
85. K. Zhang, L. Wang, J. K. Kim, M. Ma, G. Veerappan, C.-L. Lee, K.-j. Kong, H. Lee and J. H. Park, *Energy & Environmental Science*, 2016, **9**, 499-503.
86. G. Yin, X. Huang, T. Chen, W. Zhao, Q. Bi, J. Xu, Y. Han and F. Huang, *ACS Catalysis*, 2018, **8**, 1009-1017.
87. M. Zhang, Q. Pei, W. Chen, L. Liu, T. He and P. Chen, *RSC Advances*, 2017, **7**, 4306-4311.
88. J. Xu, Z. Tian, G. Yin, T. Lin and F. Huang, *Dalton Transactions*, 2017, **46**, 1047-1051.
89. Z. Wang, C. Yang, T. Lin, H. Yin, P. Chen, D. Wan, F. Xu, F. Huang, J. Lin and X. Xie, *Energy & Environmental Science*, 2013, **6**, 3007-3014.
90. G. Zhu, Y. Shan, T. Lin, W. Zhao, J. Xu, Z. Tian, H. Zhang, C. Zheng and F. Huang, *Nanoscale*, 2016, **8**, 4705-4712.
91. M. Sachs, E. Pastor, A. Kafizas and J. R. Durrant, *The journal of physical chemistry letters*, 2016, **7**, 3742-3746.
92. Y. Yamada and Y. Kanemitsu, *Applied Physics Letters*, 2012, **101**, 133907.
93. A. Yamakata, J. J. M. Vequizo and H. Matsunaga, *The Journal of Physical Chemistry C*, 2015, **119**, 24538-24545.
94. M. Setvin, C. Franchini, X. Hao, M. Schmid, A. Janotti, M. Kaltak, C. G. Van de Walle, G. Kresse and U. Diebold, *Physical review letters*, 2014, **113**, 086402.
95. T. M. Clarke and J. R. Durrant, *Chemical reviews*, 2010, **110**, 6736-6767.
96. X. Wang, Z. Feng, J. Shi, G. Jia, S. Shen, J. Zhou and C. Li, *Physical Chemistry Chemical Physics*, 2010, **12**, 7083-7090.

97. P. Maity, O. F. Mohammed, K. Katsiev and H. Idriss, *The Journal of Physical Chemistry C*, 2018, **122**, 8925-8932.
98. A. Fujishima, T. N. Rao and D. A. Tryk, *Journal of photochemistry and photobiology C: Photochemistry reviews*, 2000, **1**, 1-21.
99. K. Y. Jung, S. B. Park and M. Anpo, *Journal of photochemistry and photobiology A: Chemistry*, 2005, **170**, 247-252.
100. L. Li, P. A. Salvador and G. S. Rohrer, *Nanoscale*, 2014, **6**, 24-42.
101. Z. Zhang and J. T. Yates Jr, *Chemical reviews*, 2012, **112**, 5520-5551.
102. N. A. Deskins, R. Rousseau and M. Dupuis, *The Journal of Physical Chemistry C*, 2010, **114**, 5891-5897.
103. A. Tilocca and A. Selloni, *The Journal of Physical Chemistry B*, 2004, **108**, 4743-4751.
104. A. Stevanovic and J. T. Yates Jr, *The Journal of Physical Chemistry C*, 2013, **117**, 24189-24195.
105. R. F. Howe and M. Gratzel, *The Journal of Physical Chemistry*, 1985, **89**, 4495-4499.
106. D. Zywitzki, H. Jing, H. Tüysüz and C. K. Chan, *Journal of Materials Chemistry A*, 2017, **5**, 10957-10967.
107. A. Furube, T. Asahi, H. Masuhara, H. Yamashita and M. Anpo, *Chemical physics letters*, 2001, **336**, 424-430.
108. K. Iwata, T. Takaya, H.-o. Hamaguchi, A. Yamakata, T.-a. Ishibashi, H. Onishi and H. Kuroda, *The Journal of Physical Chemistry B*, 2004, **108**, 20233-20239.
109. M. Anpo and M. Takeuchi, *Journal of catalysis*, 2003, **216**, 505-516.
110. K. Domen, S. Naito, M. Soma, T. Onishi and K. Tamaru, *Journal of the Chemical Society, Chemical Communications*, 1980, 543-544.
111. T. Kawai and T. Sakata, *Journal of the Chemical Society, Chemical Communications*, 1980, 694-695.
112. E. Doustkhah, M. H. N. Assadi, K. Komaguchi, N. Tsunoji, M. Esmat, N. Fukata, O. Tomita, R. Abe, B. Ohtani and Y. Ide, *Applied Catalysis B: Environmental*, 2021, **297**, 120380.
113. B. Moss, Q. Wang, K. T. Butler, R. Grau-Crespo, S. Selim, A. Regoutz, T. Hisatomi, R. Godin, D. J. Payne and A. Kafizas, *Nature Materials*, 2021, **20**, 511-517.
114. Y. Xu, Y. Huang and B. Zhang, *Inorganic Chemistry Frontiers*, 2016, **3**, 591-615.
115. P. Wang, Z. Shen, Y. Xia, H. Wang, L. Zheng, W. Xi and S. Zhan, *Advanced Functional Materials*, 2019, **29**, 1807013.
116. T. Lange, S. Reichenberger, M. Rohe, M. Bartsch, L. Kampermann, J. Klein, J. Strunk, G. Bacher, R. Schlögl and S. Barcikowski, *Advanced Functional Materials*, 2021, **31**, 2009323.
117. M. Matsumura, M. Hiramoto, T. Iehara and H. Tsubomura, *The Journal of Physical Chemistry*, 1984, **88**, 248-250.
118. S. Chen and L.-W. Wang, *Chemistry of Materials*, 2012, **24**, 3659-3666.
119. J. Yang, D. Wang, H. Han and C. Li, *Accounts of chemical research*, 2013, **46**, 1900-1909.
120. K. Rajeshwar, *Journal of Applied Electrochemistry*, 2007, **37**, 765-787.
121. S. Sato and J. White, *Journal of Catalysis*, 1981, **69**, 128-139.
122. R. Li, Y. Weng, X. Zhou, X. Wang, Y. Mi, R. Chong, H. Han and C. Li, *Energy & Environmental Science*, 2015, **8**, 2377-2382.
123. R. Abe, K. Sayama, K. Domen and H. Arakawa, *Chemical physics letters*, 2001, **344**, 339-344.
124. C. C. McCrory, S. Jung, I. M. Ferrer, S. M. Chatman, J. C. Peters and T. F. Jaramillo, *Journal of the American Chemical Society*, 2015, **137**, 4347-4357.
125. S. Kampouri and K. C. Stylianou, *ACS Catalysis*, 2019, **9**, 4247-4270.
126. P. V. Kamat and S. Jin, *ACS Energy Letters*, 2018, **3**, 622-623.
127. A. Patsoura, D. I. Kondarides and X. E. Verykios, *Catalysis Today*, 2007, **124**, 94-102.
128. F. López-Tenllado, J. Hidalgo-Carrillo, V. Montes, A. Marinas, F. Urbano, J. Marinas, L. Ilieva, T. Tabakova and F. Reid, *Catalysis Today*, 2017, **280**, 58-64.
129. A. V. Puga, *Coordination Chemistry Reviews*, 2016, **315**, 1-66.
130. A. Y. Ahmed, T. A. Kandiel, I. Ivanova and D. Bahnemann, *Applied surface science*, 2014, **319**, 44-49.

131. N. Hykaway, W. Sears, H. Morisaki and S. R. Morrison, *The Journal of Physical Chemistry*, 1986, **90**, 6663-6667.
132. G. Nogami and J. H. Kennedy, *Journal of the Electrochemical Society*, 1989, **136**, 2583.
133. L. Li, J. Yan, T. Wang, Z.-J. Zhao, J. Zhang, J. Gong and N. Guan, *Nature communications*, 2015, **6**, 1-10.
134. V. M. Daskalaki and D. I. Kondarides, *Catalysis Today*, 2009, **144**, 75-80.
135. W.-C. Lin, W.-D. Yang, I.-L. Huang, T.-S. Wu and Z.-J. Chung, *Energy & Fuels*, 2009, **23**, 2192-2196.
136. B. Genorio, W. Lu, A. M. Dimiev, Y. Zhu, A.-R. O. Raji, B. Novosel, L. B. Alemany and J. M. Tour, *ACS nano*, 2012, **6**, 4231-4240.
137. M. Gopal, W. J. Moberly Chan and L. C. De Jonghe, *Journal of Materials Science*, 1997, **32**, 6001-6008.
138. M. G. Norton and C. Suryanarayana, *X-Ray diffraction: a practical approach*, Plenum Press, 1998.
139. J. I. Langford and A. Wilson, *Journal of applied crystallography*, 1978, **11**, 102-113.
140. B. W. David and C. B. Carter, *Transmission electron microscopy: A textbook for materials science*, Springer Science+ Business Media, LLC, 1996.
141. R. López and R. Gómez, *Journal of sol-gel science and technology*, 2012, **61**, 1-7.
142. F. A. Stevie and C. L. Donley, *Journal of Vacuum Science & Technology A: Vacuum, Surfaces, and Films*, 2020, **38**, 063204.
143. J. Chastain and R. C. King Jr, *Perkin-Elmer Corporation*, 1992, **40**, 221.
144. A. T. Van Loon, *Analytical atomic absorption spectroscopy: selected methods*, Elsevier, 2012.
145. L. Schanne and M. W. Haenel, *Tetrahedron Letters*, 1979, **20**, 4245-4248.
146. T. Song and U. Paik, *Journal of Materials Chemistry A*, 2016, **4**, 14-31.
147. W. Wang, Y. Liu, X. Wu, J. Wang, L. Fu, Y. Zhu, Y. Wu and X. Liu, *Advanced Materials Technologies*, 2018, **3**, 1800004.
148. S. Clarke, A. Fowkes, A. Harrison, R. Ibberson and M. Rosseinsky, *Chemistry of materials*, 1998, **10**, 372-384.
149. B. Laskova, O. Frank, M. Zikalova, M. Bousa, M. Dracinsky and L. Kavan, *Chemistry of Materials*, 2013, **25**, 3710-3717.
150. J. Pan and G. Liu, in *Semiconductors and Semimetals*, Elsevier, 2017, vol. 97, pp. 349-391.
151. V. N. Kuznetsov and N. Serpone, *The Journal of Physical Chemistry C*, 2009, **113**, 15110-15123.
152. Q. Yi, Y. Zhou, M. Xing and J. Zhang, *Research on Chemical Intermediates*, 2016, **42**, 4181-4189.
153. P. Makuła, M. Pacia and W. Macyk, *The Journal of Physical Chemistry Letters*, 2018, **9**, 6814-6817.
154. D. Cronemeyer, *Physical review*, 1959, **113**, 1222.
155. J. Mayer, U. Diebold, T. Madey and E. Garfunkel, *Journal of Electron Spectroscopy and Related Phenomena*, 1995, **73**, 1-11.
156. P. A. Schultz and R. P. Messmer, *Surface science*, 1989, **209**, 229-242.
157. J.-C. Dupin, D. Gonbeau, P. Vinatier and A. Levasseur, *Physical Chemistry Chemical Physics*, 2000, **2**, 1319-1324.
158. R. Iyengar and M. Codell, *Advances in Colloid and Interface Science*, 1972, **3**, 365-388.
159. S. Livraghi, M. Chiesa, M. C. Paganini and E. Giamello, *The Journal of Physical Chemistry C*, 2011, **115**, 25413-25421.
160. P. Cornaz, J. Van Hooff, F. Pluijm and G. Schuit, *Discussions of the Faraday Society*, 1966, **41**, 290-304.
161. E. Serwicka, M. Schlierkamp and R. Schindler, *Zeitschrift für Naturforschung A*, 1981, **36**, 226-232.
162. L. R. Grabstanowicz, S. Gao, T. Li, R. M. Rickard, T. Rajh, D.-J. Liu and T. Xu, *Inorganic chemistry*, 2013, **52**, 3884-3890.

163. M. Anpo, M. Che, B. Fubini, E. Garrone, E. Giamello and M. C. Paganini, *Topics in catalysis*, 1999, **8**, 189.
164. C. V. Pham, M. Krueger, M. Eck, S. Weber and E. Erdem, *Applied Physics Letters*, 2014, **104**, 132102.
165. S. Rao, A. Stesmans, D. Kosynkin, A. Higginbotham and J. Tour, *New Journal of Physics*, 2011, **13**, 113004.
166. B. Pilawa, A. B. Więckowski and B. Trzebicka, *Radiation Physics and Chemistry*, 1995, **45**, 899-908.
167. M. Chiesa, M. C. Paganini, S. Livraghi and E. Giamello, *Physical Chemistry Chemical Physics*, 2013, **15**, 9435-9447.
168. G. Radtke, S. Lazar and G. Botton, *Physical Review B*, 2006, **74**, 155117.
169. A. Gloter, C. Ewels, P. Umek, D. Arcon and C. Colliex, *Physical Review B*, 2009, **80**, 035413.
170. E. Stoyanov, F. Langenhorst and G. Steinle-Neumann, *American Mineralogist*, 2007, **92**, 577-586.
171. S. Yang, Y. Liu, Y. Guo, J. Zhao, H. Xu and Z. Wang, *Materials chemistry and physics*, 2003, **77**, 501-506.
172. Q. Zhang, R. Li, Z. Li, A. Li, S. Wang, Z. Liang, S. Liao and C. Li, *Journal of Catalysis*, 2016, **337**, 36-44.
173. J. Livage, M. Henry and C. Sanchez, *Progress in solid state chemistry*, 1988, **18**, 259-341.
174. B. Nabivanets, *Russ. J. Inorg. Chem*, 1962, **7**, 212.
175. B. Nabivanets and L. Kudritskaya, *Russ. J. Inorg. Chem*, 1967, **12**, 616.
176. B. Nabivanets and L. Kudritskaya, *Russ. J. Inorg. Chem*, 1967, **12**, 789-792.
177. A. Pottier, C. Chanéac, E. Tronc, L. Mazerolles and J.-P. Jolivet, *Journal of Materials Chemistry*, 2001, **11**, 1116-1121.
178. Q. Zhang and L. Gao, *Langmuir*, 2003, **19**, 967-971.
179. L. Pauling, *Journal of the american chemical society*, 1929, **51**, 1010-1026.
180. J. H. Watson, W. Heller and W. Wojtowicz, *Science*, 1949, **109**, 274-278.
181. A. Bleier and R. Cannon, *Materials Research Society, Pittsburgh, PA*, 1986.
182. T. Zoltai and J. Stout, *Co., Minneapolis, Minnesota*, 1984, **126**.
183. Y. Wang and G. S. Hwang, *Surface science*, 2003, **542**, 72-80.
184. Y. Wang, T. Sun, X. Liu, H. Zhang, P. Liu, H. Yang, X. Yao and H. Zhao, *Physical Review B*, 2014, **90**, 045304.
185. G. Li, L. Li, J. Boerio-Goates and B. F. Woodfield, *Journal of materials research*, 2003, **18**, 2664-2669.
186. A. A. Levchenko, G. Li, J. Boerio-Goates, B. F. Woodfield and A. Navrotsky, *Chemistry of Materials*, 2006, **18**, 6324-6332.
187. B. E. Yoldas, *Journal of materials science*, 1979, **14**, 1843-1849.
188. A. Heller, *Accounts of chemical research*, 1981, **14**, 154-162.
189. T. Sham and M. Lazarus, *Chemical Physics Letters*, 1979, **68**, 426-432.
190. E. McCafferty and J. Wightman, *Surface and Interface Analysis: An International Journal devoted to the development and application of techniques for the analysis of surfaces, interfaces and thin films*, 1998, **26**, 549-564.
191. J. Carrasco, J. Klimeš and A. Michaelides, *The Journal of chemical physics*, 2013, **138**, 024708.
192. T. Ohno, K. Sarukawa and M. Matsumura, *New journal of chemistry*, 2002, **26**, 1167-1170.
193. K. Wenderich, A. Klaassen, I. Siretanu, F. Mugele and G. Mul, *Angewandte Chemie International Edition*, 2014, **53**, 12476-12479.
194. O. Byl and J. T. Yates, *The Journal of Physical Chemistry B*, 2006, **110**, 22966-22967.
195. E. Hendry, F. Wang, J. Shan, T. F. Heinz and M. Bonn, *Physical Review B*, 2004, **69**, 081101.



# Curriculum vitae

Igor Medic, M. Sc.

Born on the June 8<sup>th</sup>, 1992, in Novi Sad, Serbia

## Academic Education

August 2019 – June 2023	Ph.D. in Chemistry: Leibniz Institute for Catalysis e.V. at University of Rostock, Germany
October 2015 – September 2016	M.Sc. in Chemistry: Faculty of Sciences, University of Novi Sad, Serbia
October 2011 – September 2015	B.Sc. with Honours in Chemistry: Faculty of Sciences, University of Novi Sad, Serbia

## Scientific contribution

### Publications:

#### Paper

Ding, S.; Medic, I.; Steinfeldt, N.; Dong, T.; Voelzer, T.; Haida, S.; Rabeah, J.; Hu, J.; Strunk, J. Ultrathin Defective Nanosheet Subunit ZnIn<sub>2</sub>S<sub>4</sub> Hollow Nanoflowers for Efficient Photocatalytic Hydrogen Evolution. *Small Structures* 2023, 2300091. DOI: [10.1002/sstr.202300091](https://doi.org/10.1002/sstr.202300091)

#### Paper

Sebek, M.; Peppel, T.; Lund, H.; Medic, I.; Springer, A.; Mazierski, P.; Zaleska-Medynska, A.; Strunk, J.; Steinfeldt, N. Thermal annealing of ordered TiO<sub>2</sub> nanotube arrays with water vapor-assisted crystallization under a continuous gas flow for superior photocatalytic performance. *Chemical Engineering Journal* 2021, 425, 130619. DOI: [10.1016/j.cej.2021.130619](https://doi.org/10.1016/j.cej.2021.130619)

#### Paper

Djordjevic, A.; Merkulov, D. Š.; Lazarević, M.; Borišev, I.; Medić, I.; Pavlović, V.; Miljević, B.; Abramović, B. Enhancement of nano titanium dioxide coatings by fullerene and polyhydroxy fullerene in the photocatalytic degradation of the herbicide mesotrione. *Chemosphere* 2018, 196, 145-152. DOI: [10.1016/j.chemosphere.2017.12.160](https://doi.org/10.1016/j.chemosphere.2017.12.160)

### **Oral presentations:**

Medić, I.; Borišev, I.; Jović, D.; Srdić, V.; Đorđević, A. The impact of changes of experimental conditions and organic solvent on nC<sub>60</sub> particle size. In Fifteenth Young Researchers Conference – Materials Science and Engineering, Belgrade, Serbia; December 7-9, 2016.

Novaković, M.; Medić, I.; Borišev, I.; Jović, D.; Srdić, V.; Đorđević, A. Synthesis and characterization of fullerene C<sub>60</sub> carboxylic derivatives. In Fourteenth Young Researchers Conference – Materials Science and Engineering, Belgrade, Serbia; December 9-11, 2015.

Igor Medić, Aleksandar Djordjević, Ivana Borišev, Danica Jović. "Fullerene C<sub>60</sub> Dimer Oxides." In *Thirteenth Young Researchers Conference – Materials Science and Engineering*. Belgrade, Serbia, December 10-12, 2014.

### **Poster presentations:**

Medic, I.; Springer, A.; Lund, H.; Zapf, A.; Strunk, J. Solar-driven H<sub>2</sub> production on rutile TiO<sub>2</sub> nanoneedles with sub-10 nm crystallites. In 23<sup>rd</sup> International Conference on Photochemical Conversion and Storage of Solar Energy (IPS-23), Lausanne, Switzerland; August 2-5, 2022.

Bíborka, B.; Steinfeldt, N.; Medic, I.; Moustakas, N.; Lund, H.; Vasile-Mircea, C.; Pap, Z.; Strunk, J. The development of novel SrTiO<sub>3</sub>-based catalysts for photocatalytic applications. In 11th European Conference on Solar Chemistry and Photocatalysis: Environmental Applications (SPEA), Turin, Italy, June 6-10, 2022.

Medic, I.; Springer, A.; Lund, H.; Zapf, A.; Strunk, J. Solar-driven H<sub>2</sub> production on rutile TiO<sub>2</sub> nanoneedles with sub-10 nm crystallites. In 3<sup>rd</sup> ComBioCat Symposium 2022 - PATHWAYS TO SUSTAINABLE CHEMICAL SYNTHESIS, Rostock, Germany; June 8-9, 2022.

Kojić, V.; Jakimov, D.; Vucinic, N.; Djan, I.; Borišev, I.; Jović, D.; Medić, I.; Djordjevic, A. Radioadaptive irradiation combined with radiosensitising effects of gold nanoparticles on the healthy and cancer human lung cell lines. In *Advanced Ceramics and Applications VI: New Frontiers in Multifunctional Material Science and Processing*, Belgrade, Serbia; September 18-20, 2017.

Medić, I.; Panić, S.; Đurđić, E.; Jović, D.; Bošković, G.; Cvejić, Ž.; Rakić, S.; Đorđević, A. Oxidative longitudinal unzipping of short MWCNTs toward graphene nanoribbons. In *NINETEENTH ANNUAL CONFERENCE YUCOMAT 2017*, Herceg Novi, Montenegro; September 4-8, 2017.